TECHNISCHE UNIVERSITÄT MÜNCHEN

LEHRSTUHL FÜR AERODYNAMIK UND STRÖMUNGSMECHANIK

Numerical investigation of the flow field around a delta wing

Christian Zwerger

Vollständiger Abdruck der von der Fakultät für Maschinenwesen der Technischen Universität München zur Erlangung des akademischen Grades eines

Doktor-Ingenieurs

genehmigten Dissertation.

Vorsitzender:		Prof. Dr.-Ing. Hans-Jakob Kaltenbach
Prüfer der Dissertation:	1.	Prof. Dr.-Ing. Nikolaus A. Adams
	2.	Prof. Dr.-Ing. Stefan Hickel,
		Technische Universiteit Delft

Die Dissertation wurde am 07.12.2015 bei der Technischen Universität München eingereicht und durch die Fakultät für Maschinenwesen am 07.12.2016 angenommen.

Abstract

The flow field around delta wings is characterized by a variety of interesting phenomena, which are not fully understood yet, most notably the primary vortex and its possible breakdown. Along with the multitude of applications in industry, delta wings have thus been a focus of intensive research for several decades.

This work numerically investigates the generic vortex flow experiment-2 (VFE-2) delta wing configuration in a subsonic regime using wall modeled implicit large eddy simulation. First, leading edge bluntness effects on the primary vortex separation behavior are considered by simulating sharp and round leading edge geometries for different angles of attack. The numerical results are compared with experimental measurements conducted at the Institute of Aerodynamics and Fluid Mechanics of Technische Universität München. Overall, the agreement is very good for the sharp leading edge geometry, for which the primary vortex separation is geometrically fixed at the leading edge, and good for the round leading edge, which is more challenging due to the fact that the primary vortex separation occurs from a smooth curved surface. The investigations show that the employed grid resolution in combination with a wall model based on the simplified turbulent boundary layer equations (TBLE) is not sufficient to accurately predict the separation behavior and the pressure coefficient distribution on the wing surface, but simulations with a better resolved wall region clearly improve the predictions. A well resolved wall region could not be achieved, however, due to the limited computational resources. Nonetheless, the numerical results are qualitatively consistent in all respects with the experimental measurements and show quantitatively reasonable to good agreement, notably regarding quantities away from the wall.

Second, two mechanisms to control vortex breakdown are examined. One, oscillating control surfaces at the leading edges, which have also been investigated experimentally. The numerical simulations show that this approach has only a minor effect on the vortex breakdown position in the pre-stall regime considered, which confirms the experimental observations. Two, a novel approach based on a geometric modification leading to the injection of fluid from the pressure side is presented. The numerical simulations show that such an approach can have a significant effect on the vortex breakdown location and thus appears to be a promising direction for further investigations.

Contents

List of Figures

List of Tables

Abbreviations

ALDM	**A**daptive **L**ocal **D**econvolution **M**ethod
AMR	**A**daptive **M**esh **R**efinement
AV	**A**pex **V**ortex
AVAL	**A**pex **V**ortex **A**ttachment **L**ine
AVSL	**A**pex **V**ortex **S**eparation **L**ine
CAD	**C**omputer **A**ided **D**esign
CFL	**C**ourant-**F**riedrichs-**L**ewy
CFD	**C**omputational **F**luid **D**ynamics
CIIM	**C**onservative **I**mmersed **I**nterface **M**ethod
DES	**D**etached **E**ddy **S**imulation
DNS	**D**irect **N**umerical **S**imulation
EDQNM	**E**ddy **D**amped **Q**uasi-**N**ormal **M**arkovian
EOS	**E**quation **O**f **S**tate
EXP	**EXP**eriment
FC	**F**low **C**ontrol
IB	**I**mmersed **B**oundary
LE	**L**eading **E**dge
LES	**L**arge **E**ddy **S**imulation
LRLE	**L**arge **R**adius **L**eading **E**dge
LRZ	**L**eibniz-**R**echen**Z**entrum
MDE	**M**odified **D**ifferential **E**quation
MRLE	**M**edium **R**adius **L**eading **E**dge
MPI	**M**essage **P**assing **I**nterface
NN	**N**eural **N**etwork
OpenMP	**O**pen Multi-**P**rocessing

PV	**P**rimary **V**ortex
PVAL	**P**rimary **V**ortex **A**ttachment **L**ine
PVSL	**P**rimary **V**ortex **S**eparation **L**ine
RANS	**R**eynolds-**A**veraged **N**avier-**S**tokes
RMS	**R**oot **M**ean **S**quare
SALD	**S**implified **A**daptive **L**ocal **D**econvolution method
SIM	**SIM**ulation
SGS	**S**ub**G**rid **S**cale
SLE	**S**harp **L**eading **E**dge
SRLE	**S**mall **R**adius **L**eading **E**dge
STL	**ST**ereo**L**ithography
SV	**S**econdary **V**ortex
SVAL	**S**econdary **V**ortex **A**ttachment **L**ine
SVSL	**S**econdary **V**ortex **S**eparation **L**ine
TBLE	**T**urbulent **B**oundary **L**ayer **E**quations
TCF	**T**urbulent **C**hannel **F**low
TEV	**T**railing **E**dge **V**ortex
VB	**V**ortex **B**reakdown
VFE-1	**V**ortex **F**low **E**xperiment-**1**
VFE-2	**V**ortex **F**low **E**xperiment-**2**
WM	**W**all **M**odel

Chapter 1

Introduction

This introductory chapter contains three sections. Section one gives the motivation for the investigation of delta wings, section two discusses possible methods of investigation, and section three specifies the objectives of this work.

1.1 Motivation for the investigation of delta wings

Delta wing configurations have many applications in industry, e.g. high-agility aircraft, vortex generators, or more exotic devices such as snow fences [1, 2]. In each of these cases, the development of large leading edge vortices, see Fig. 1.1, is utilized. Applied in high-agility aircraft, the additional lift originating from the primary vortices leads to advantageous properties regarding the maneuverability of the aircraft. However, at high angles of attack, a sudden breakdown of the leading edge vortex may occur, see Fig. 1.1. Vortex breakdown entails a significant change in the aerodynamic quantities bringing forth disadvantageous effects, such as worsened maneuverability and higher structural loads due to increased turbulence levels. Hence, a thorough understanding of the flow field is of considerable importance and inevitable for the development and investigation of flow control mechanisms, which are aimed at controlling the complex flow structures.

In view of the many interesting and unsolved problems regarding the flow around delta wings, it has been studied for decades [3–8], and more recently, significant collaborative efforts have been undertaken in the framework of the international vortex flow
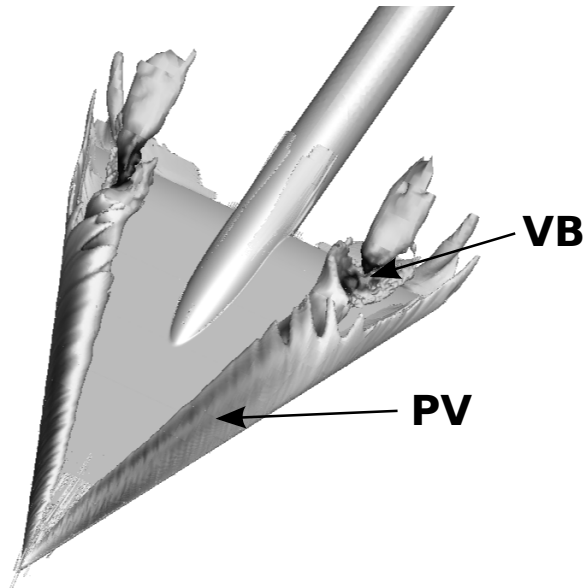
FIGURE 1.1: Characteristic vortex structure of the flow field around a delta wing. PV - primary vortex; VB - vortex breakdown. Figure shows isosurfaces of streamwise vorticity colored by streamwise velocity, extracted from a numerical simulation of the flow field around the VFE-2 delta wing with round leading edge.

experiments VFE-1 and VFE-2 [9–16], providing a large data base of experimental and computational investigations.

1.2   Possible methods of investigation

Commonly, there are three investigation approaches, namely analytical, experimental, and numerical investigation.

1.2.1   Analytical investigation

Regarding the flow around delta wings, the scope of analytical results is very limited. It is presumed that the motion of Newtonian fluids is accurately described by the Navier-Stokes equations. However, for a general three-dimensional problem, some mathematical properties of these equations are not fully understood yet, notably existence and, for the incompressible form only, smoothness of solutions [17–19]. Hence, there is only a small number of problems, usually problems for which a number of simplifying assumptions can be made, for which analytical solutions have been found, and one is far from analytically solving the Navier-Stokes equations for complex problems such as the turbulent flow around delta wings.

Nonetheless, some important aspects regarding the flow around delta wings, e.g. the nonlinear increase of lift and the shape of the pressure distribution on the wing, can be derived analytically using potential flow theory and further assumptions, such as conical flow, see [3, 20, 21]. Further analytical approaches can be found in [22–24], and analytical results obtained within VFE-2 are reported by Nangia in [25, 26]. Moreover, some of the phenomena appearing in the flow field around a delta wing have been studied analytically as isolated phenomena, e.g. vortex breakdown in [27].

1.2.2 Experimental investigation

Experimental investigations of the flow field around a delta wing have been a primary contributor to advancing the understanding of the diverse flow features and have been carried out at various institutions for decades. In the framework of VFE-2, measurements were conducted, amongst others [28–37], at the Institute of Aerodynamics and Fluid Mechanics of Technische Universität München [38–41]. Overall, experimental investigations can still be considered as the most reliable and most accurate way to investigate complex, industrially relevant flows, such as the flow around a delta wing, which is why they are prevalently used to validate analytical and numerical investigations. However, experiments have several drawbacks, notably the necessity of complex apparatus and equipment and the limited number of measurement points, see table 1.1.

1.2.3 Numerical investigation

Some of the shortcomings of experimental investigations can be easily dealt with in numerical investigations, see table 1.1 for a comparison, which motivated extensive research efforts in the last decades. Even though an analytical solution of the Navier-Stokes equations for the turbulent flow around obstacles is not within reach, it is possible to numerically approximate the governing or modified equations and thereby compute approximate solutions using the increasing capabilities of compute systems. The most common approaches for turbulent flows are direct numerical simulation (DNS), simulations based on the Reynolds-averaged Navier-Stokes equations (RANS), and large eddy simulation (LES). These approaches differ in and can be evaluated according to level of description, completeness, cost and ease of use, range of applicability, and accuracy [42].

TABLE 1.1: Comparison of experimental and numerical investigations. The mentioned aspects should be considered as general but can of course differ depending on the particular problem at hand.

Experimental investigations	Numerical investigations
expensive	cheap
slow	fast
little data due to few measurement points in space and time	lots of data due to high resolution in space and time
accessible problems limited by equipment and apparatus	virtually any problem accessible
actual physics	modeled physics

Hereafter, a short description of DNS, RANS, and LES is given, and their possible application to the study of the flow field around a delta wing is discussed.

1.2.3.1 DNS

From a conceptual point of view, DNS is the most straightforward numerical approach: the Navier-Stokes equations are discretized in such a way that all scales of fluid motion are resolved. DNS therefore provides the highest level of description possible and is complete in the sense that no flow dependent specifications are present in the model's equations [42]. However, DNS becomes prohibitive in consideration of cost and ease of use when applied to practical problems, such as the turbulent flow around a delta wing, given the large range of time and length scales. Chapman [43] estimated that the number of grid points required to perform a DNS scales as $N_{DNS} \sim Re_L^{9/4}$, where $Re_L = \frac{U \cdot L}{\nu}$ denotes the Reynolds number, determined by free stream velocity U, characteristic length L, and kinematic viscosity ν. However, this estimate has recently been revised by Choi and Moin [44] to an even larger number, $N_{DNS} \sim Re_L^{37/14}$. Furthermore, Piomelli and Balaras [45] state that the number of time steps required for a simulation is proportional to $N^{1/3}$, where N denotes the number of grid points. Therefore, assuming that one needs 1000 floating point operations per grid point and time step [42], the time required to

perform a DNS of a wall-bounded flow at a Reynolds number of $Re_L = 2.0 \cdot 10^6$, which will be considered in this work, on a supercomputer providing a computing rate of 13 petaflops is

$$T_{DNS} \sim \frac{10^3 \cdot (Re_L^{37/14})^{4/3}}{13 \cdot 10^{15} \cdot 60 \cdot 60 \cdot 24} \, days \approx 14229 \, days \approx 39 \, years \,. \qquad (1.1)$$

This estimate is still optimistic since it is derived for canonical geometries. The computational cost for complex geometries cannot be derived a priori [45] but can be orders of magnitude higher [46]. DNS has thus a very limited range of applicability and has mainly been used to study geometrically simple, academic test cases, e.g. turbulent channel flow [47] or the flow over a backward facing step [48]. DNS can therefore be considered as primarily a research tool [49].

1.2.3.2   RANS

The idea of RANS is to decompose the velocity field $\boldsymbol{u}$ into a mean part $\langle \boldsymbol{u} \rangle$ and a fluctuating part $\boldsymbol{u_f}$ via an averaging operation [42], i.e.

$$\boldsymbol{u} = \langle \boldsymbol{u} \rangle + \boldsymbol{u_f} \,. \qquad (1.2)$$

Applying this averaging operation to the Navier-Stokes equations yields the Reynolds equations for the mean part of the velocity field, which are unclosed due to the appearance of the so-called *Reynolds stress* term arising from the fluctuating part. For closure, the Reynolds equations must therefore be solved along with turbulence model equations for the Reynolds stress term. Evidently, this approach gives a significantly lower level of description than DNS [42]. However, regarding cost, ease of use, and range of applicability, RANS approaches can be viewed as the most convenient and thus are the most commonly used in industry [50]. A detailed description of various RANS approaches is given in [42, 51, 52].

RANS simulations of the flow field around a delta wing have been conducted with varying success in numerous studies, i.a. for the VFE-2 delta wing by Fritz [53–55], Le Roy et al. [56], Le Roy and Riou [57], Boelens [58], Gurdamar et al. [59, 60], Crippa [61], Crippa

and Rizzi [62, 63], and Crivellini et al. [64]. However, given that the fluctuating part is not represented, RANS approaches seem by their very nature unsuitable for flows in which large-scale three-dimensional unsteady motions are crucial, such as the flow around delta wings or bluff bodies [42]. It is thus not surprising that various authors, e.g. [65–69], report problems in accurately predicting massively separated flows using RANS approaches. Moreover, in many cases, an assumption regarding transition is needed, which can have a substantial effect on the results [64, 69]. Therefore, RANS approaches usually necessitate additional corrections and parameter-twiddling to accurately predict the flow around a delta wing.

1.2.3.3   LES

Conceptionally, the idea of LES is to decompose the velocity field $\boldsymbol{u}$ into a represented part $\overline{\boldsymbol{u}}$ and an unrepresented part $\boldsymbol{u}'$ via a filtering operation [42], i.e.

$$\boldsymbol{u} = \overline{\boldsymbol{u}} + \boldsymbol{u}'. \tag{1.3}$$

The represented part is also called resolved or filtered part, and the unrepresented part is also called unresolved, residual, or subgrid scale (SGS) part. Applying this filtering operation to the Navier-Stokes equations yields equations for the represented part of the velocity field, which are unclosed due to the appearance of the so-called *subgrid scale (SGS) stress* term. For closure, the equations for the represented part therefore require a model for the subgrid stress term. Even though the decompositions used in LES and RANS seem similar, there are two important differences [42]. First, the represented part in LES, $\overline{\boldsymbol{u}}$, is a random field, whereas the mean part in RANS, $\langle \boldsymbol{u} \rangle$, is an averaged field. Second, the filtered unrepresented part in LES is generally not zero, i.e. $\overline{\boldsymbol{u}'} \neq 0$, whereas the averaged fluctuating part in RANS is zero, i.e. $\langle \boldsymbol{u_f} \rangle = 0$. Detailed information regarding the underlying ideas of LES including derivations and descriptions of various SGS models can be found in [42, 70, 71].

Given that in LES, the large energy-containing unsteady scales are represented, it provides a higher level of description than RANS approaches and seems more suitable for vortical flows. Regarding cost and ease of use, LES lies between RANS and DNS. The former, however, is the main drawback of LES in wall-bounded flows. In the near wall

region, the size of the relevant turbulent eddies scales approximately linearly with the wall distance [72]. Resolving these eddies yields a Reynolds number dependent grid point requirement that is almost as severe as that of DNS [72]. Using such a grid resolution yields a *well resolved* LES [73]. In many cases, however, only the wall normal direction is resolved with a grid spacing approaching that of DNS, and the horizontal grid spacing is coarser. Such a LES is called *wall resolved* [73]. Chapman [43] originally estimated that the number of grid points required for a wall resolved LES scales with the Reynolds number Re_L as $N_{LES,wr} \sim Re_L^{9/5}$. This estimate has recently been revised by Choi and Moin and the new estimate is $N_{LES,wr} \sim Re_L^{13/7}$ [44]. Assuming one wants to perform a wall resolved LES of a wall-bounded flow at $Re_L = 2 \cdot 10^6$, the number of grid points required becomes

$$N_{LES,wr} \sim Re_L^{13/7} \approx 5 \cdot 10^{11} \, , \tag{1.4}$$

which is still prohibitively expensive. Wall resolved LES of industrially relevant high-Reynolds number flows is therefore not feasible at this point. This problem can be circumvented by wall modeled LES, in which the near wall region is not resolved but approximated by a wall model, which yields a grid point requirement of $N_{LES,wm} \sim Re_L$ [44]. Again, this estimate is optimistic since it is derived for canonical geometries. Nonetheless, one can expect that wall modeled LES can be used to investigate flows of practical interest, such as the flow around a delta wing.

Wall modeled LES has been used with moderate success by Mary [74] to investigate the flow around a delta wing with sharp leading edge, but apart from this investigation, to the author's knowledge, there are no other results reported in the literature, in particular regarding a delta wing with round leading edge.

It should be noted that there are other approaches trying to circumvent the prohibitive grid resolution requirements of wall resolved LES, notably various forms of hybrid RANS / LES or DES, see e.g. [68, 75, 76], which have been used to investigate the flow field around a delta wing, e.g. for the VFE-2 delta wing by Le Roy and Riou [57], Crippa and Rizzi [62], Crippa [61], Cummings and Schütte [77–79], Tangermann et al. [80], and Jirasek [81]. So far, no single method has proven superior to the others, including wall

modeled LES [82], and such approaches are not investigated within the scope of this work.

1.3   Objectives of this work

The Institute of Aerodynamics and Fluid Mechanics of Technische Universität München participated in VFE-2 and contributed comprehensive data from wind tunnel measurements. The present work numerically investigates the very same configurations and thus constitutes a complement to the past and current experimental efforts. Among the feasible ways to numerically investigate the flow around a delta wing, wall modeled LES is expected to provide the highest level of description. Therefore, the capability of wall modeled LES for the flow around the VFE-2 delta wing is assessed in this work. Two aspects of the flow field are of particular interest: (A) the leading edge bluntness effects on the primary vortex separation [35], and (B), vortex breakdown above the wing and its control [83]. Addressing these two aspects are thus the two main objectives of this work.

Regarding objective (A), simulations are first conducted for the VFE-2 delta wing with medium radius round leading edge (MRLE) at three different angles of attack α, namely 13°, 18°, and 23°, resulting in different overall flow characteristics: partly attached flow for $\alpha = 13°$, fully developed leading edge vortex for $\alpha = 18°$, and fully developed leading edge vortex with vortex breakdown for $\alpha = 23°$. The same angles of attack are then investigated for the sharp leading edge (SLE).

Regarding objective (B), simulations with active flow control via oscillating control surfaces at the leading edges are carried out for the SLE and $\alpha = 28°$. Furthermore, a novel approach based on a geometric modification, leading to the injection of fluid from the pressure side, is presented.

This work consists of seven chapters. Following this introductory chapter, chapter 2 describes the flow physics of the flow around delta wings and briefly introduces some aspects concerning flow control, which will be relevant in the subsequent chapters. Chapter 3 provides details regarding the numerical methods used throughout the investigations, and chapter 4 delineates some aspects as to the realization of the simulations. In chapter 5, the numerical results with respect to objective (A), leading edge bluntness effects on

primary vortex separation, are discussed in detail. Chapter 6 presents the results of the investigations regarding objective (B), control of vortex breakdown via flow control mechanisms. Finally, chapter 7 summarizes the results obtained, discusses their significance and implications in a wider context, and provides a brief outlook to possible further investigations.

Chapter 2

Delta wing flow physics

This chapter illustrates characteristic features of the flow field around a delta wing. It contains five sections. Section one describes the primary vortex, section two the secondary vortex, and section three the trailing edge vortex. Section four provides information regarding the phenomenon of vortex breakdown, and section five discusses flow control mechanisms targeting vortex breakdown.

2.1   Primary vortex

The most prominent feature of the flow over delta wings is the development of two large vortices above the wing, originating from the flow separation at the leading edges. These vortices are called primary vortices. Their existence depends notably on sweep angle (φ), leading edge radius (r), angle of attack (α), and free stream velocity (U_∞). Stanbrook and Squire [84] derived a criterion indicating their existence, based on quantities normal to the leading edge, see Fig. 2.1, with angle of attack α_N and Mach number $Ma_{\infty,N}$ given by the equations below. The Mach number Ma_∞ is defined by the ratio of free stream velocity and speed of sound.

$$\alpha_N = arctan\left(\frac{tan\ \alpha}{cos\ \varphi}\right) \tag{2.1}$$

$$Ma_{\infty,N} = Ma_\infty \cdot cos\ \varphi \cdot \sqrt{1 + sin^2\ \alpha \cdot tan^2\ \varphi} \tag{2.2}$$
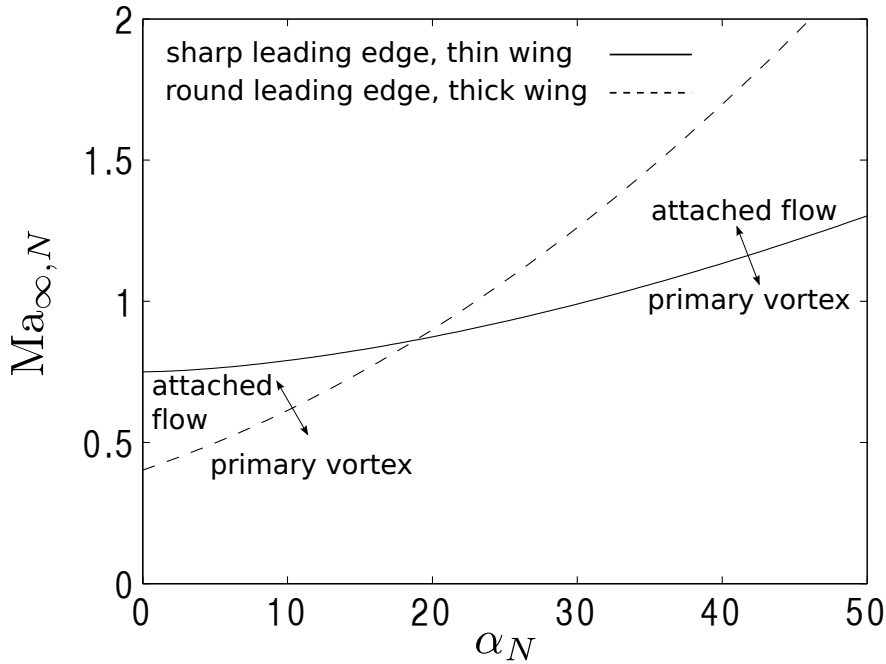
FIGURE 2.1: Stanbrook-Squire criterion indicating the existence of primary vortices:
Solid line for thin wings with sharp leading edge,
$$Ma_{\infty,N} = 0.75 + 0.000940\alpha_N^{1.63};$$
Dashed line for thick wings with round leading edge,
$$Ma_{\infty,N} = 0.20 + 0.000375(|\alpha_N| + 23.2)^2.$$
Illustration following Stanbrook and Squire [84].

In case of separation, the flow rolls up into two stable conical vortex sheets and some fluid is drawn over the vortex sheets and accelerated downward, resulting in an attaching flow, indicated by an attachment line inboard of the primary vortex [5], see Fig. 2.2.

The fluid then moves towards the leading edge which leads to high velocities in spanwise direction resulting in suction peaks below the axes of the primary vortices on the upper part of the wing. These suction peaks give rise to an additional, vortex induced lift and yield a nonlinear increase of lift, see Fig. 2.3.

The precise location of the flow separation and the vortex structure depend on several aspects, i.a. sweep angle, angle of attack, Reynolds number Re, Mach number Ma, and notably leading edge geometry [35]. The dependance on leading edge geometry is succinctly summarized in the sketch by Luckring [86], see Fig. 2.4. As opposed to a sharp leading edge, where separation is geometrically fixed at the apex, separation for a round leading edge initially occurs at a location close to the trailing edge and then moves up the leading edge with increasing angle of attack [35]. This results from

Spiral-shaped
vortex sheets

Primary vortex
attachment lines
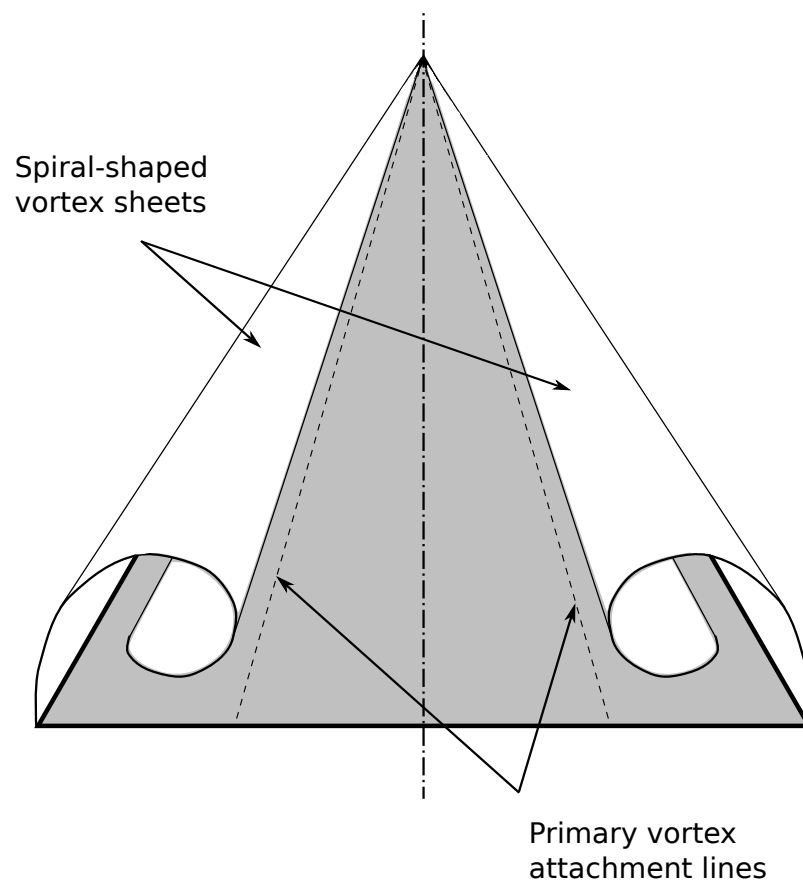
FIGURE 2.2: Illustration of primary vortex, following Polhamus [5].

vortex induced
nonlinear lift

vortex
breakdown

C_L

α
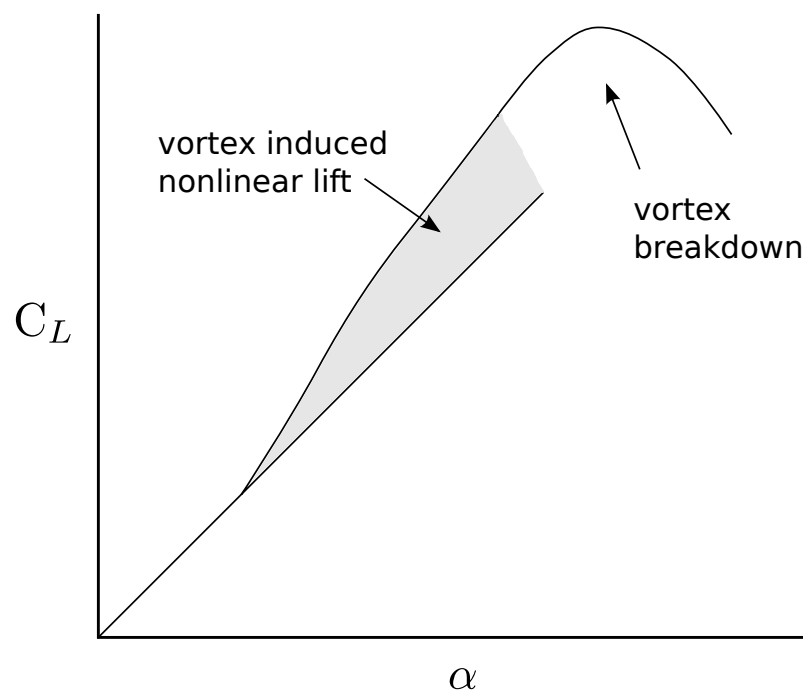
FIGURE 2.3: Lift coefficient C_L of delta wings depending on angle of attack α. Sketch
following Polhamus [5] and Breitsamter [85].

Sharp leading edge   Round leading edge

Vortex origin fixed   Vortex origin displaced
at apex   from apex

Separation fixed   Separation near
at leading edge   leading edge
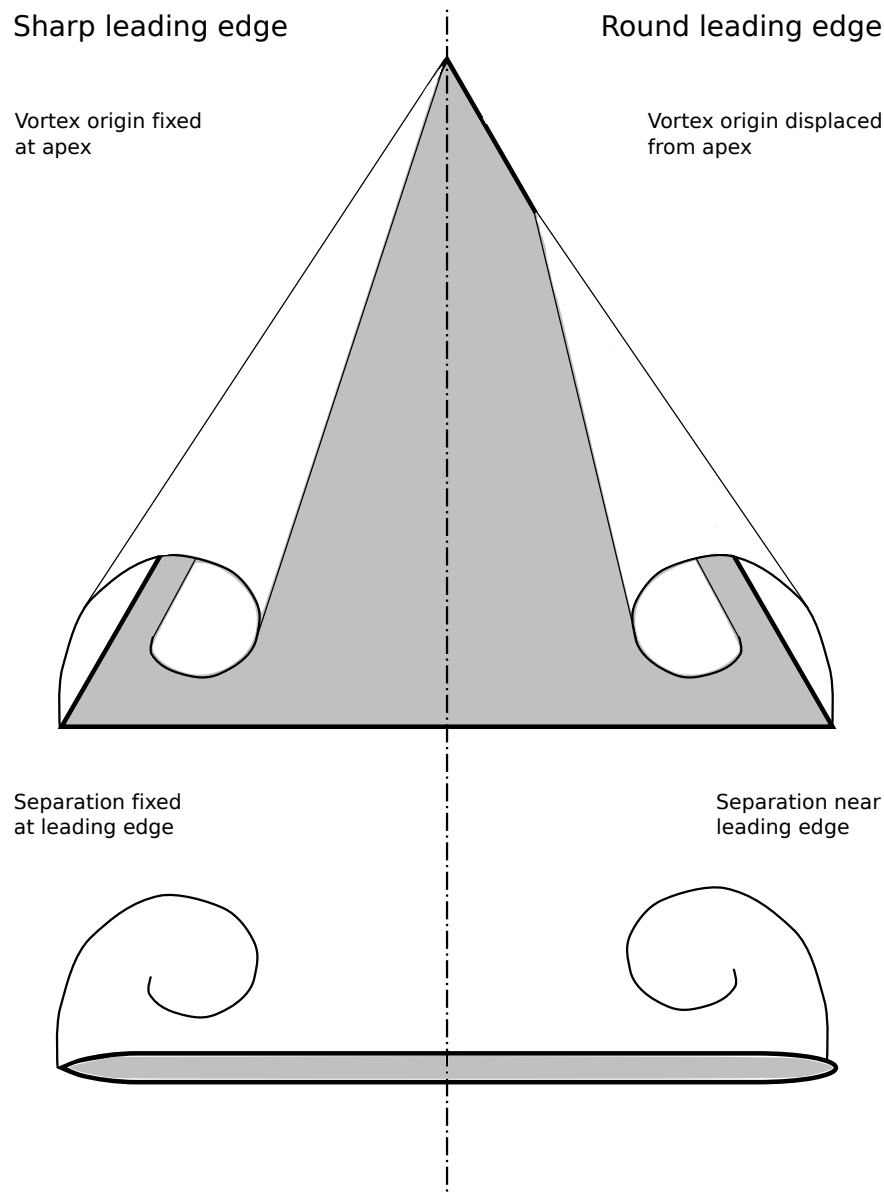
FIGURE 2.4: Influence of leading edge geometry on primary vortex onset, following
Luckring [86].

two facts [35]: (1) the local angle of attack is higher near the trailing edge, and (2),
the crossflow bluntness r_{le}/b_{loc}, where r_{le} denotes leading edge radius and b_{loc} denotes
local span width, increases from blunter to sharper as the trailing edge is approached.
Another important difference is that separation for a round leading edge occurs slightly
inboard of the leading edge and is not fixed precisely at the leading edge, as for a sharp
leading edge, see Fig. 2.4.

A detailed sketch of the primary vortex structure is shown in Fig. 2.5. Three aspects
are particularly noteworthy:
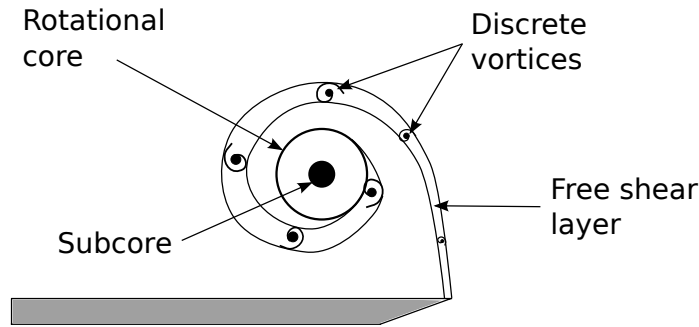
FIGURE 2.5: Primary vortex structure, following Breitsamter [85].

(1) **Free shear layer**

The free shear layer originating from the leading edges thickens while rolling up and contains discrete vortices (Kelvin-Helmholtz instabilities) [87].

(2) **Rotational core**

The rotational core is formed by the rolled-up shear layer and has a diameter of up to 30% of the local half span width [87].

(3) **Subcore**

The subcore, dominated by viscous effects, is embedded in the rotational core and marked by high streamwise velocities and low static pressures [87].

2.2 Secondary vortex

As mentioned in the previous section, the primary vortex induces a reattached flow in spanwise direction on the upper side of the wing. This flow may separate due to the adverse pressure gradient and form a vortex which is counter-rotating to the primary vortex, called secondary vortex. It lies outboard of the primary vortex [35], see Fig. 2.6, and leads to a second suction peak in the pressure distribution. The presence and size of the secondary vortex depends strongly on whether the reattached spanwise flow is laminar or turbulent [88], see Fig. 2.7.

2.3 Trailing edge vortex

The most prominent phenomenon in the wake region is the so-called trailing edge vortex, first investigated and explained by Hummel and Redeker [89], who also introduced the
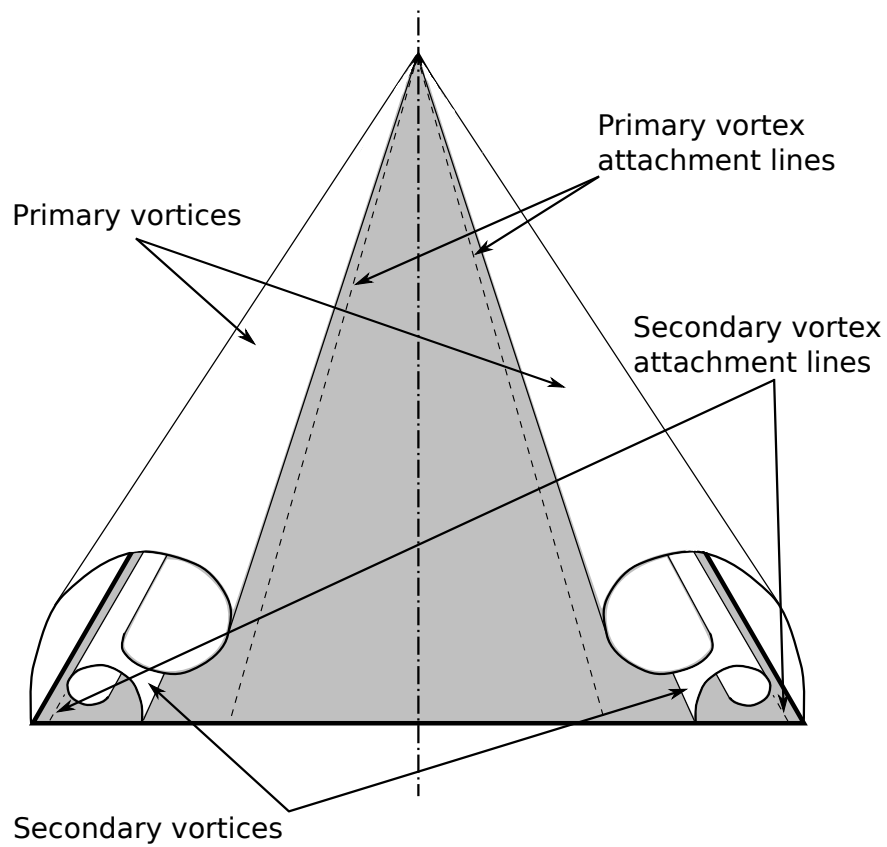
FIGURE 2.6: Illustration of secondary vortex, following Hummel [88].
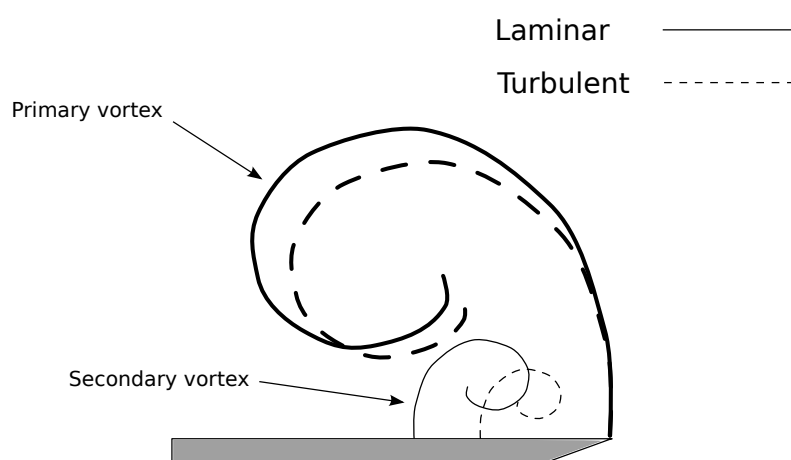
FIGURE 2.7: Shape of primary and secondary vortex depending on whether the flow is laminar or turbulent, following Hummel [88].
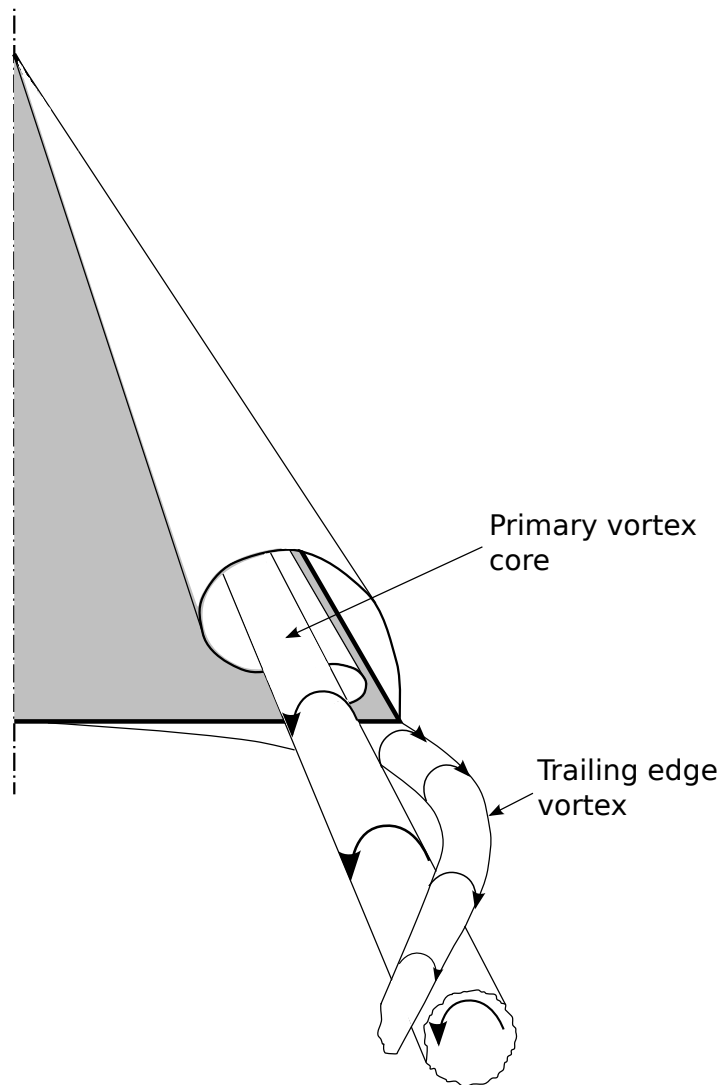
FIGURE 2.8: Illustration of trailing edge vortex, following Breitsamter [87].

term. As a result of the velocity distribution on the upper and lower part of the wing, a vortex sheet, whose vorticity has opposite sign of the primary vortex's, originates from the trailing edge, rolls up, and moves toward the trailing edge tip, where it forms the trailing edge vortex. This counter-rotating vortex then rolls up around the primary vortex and finally dissipates. Even though secondary and trailing edge vortex rotate in the same direction, the two are distinct phenomena [89]. A sketch of the phenomenon is shown in Fig. 2.8.
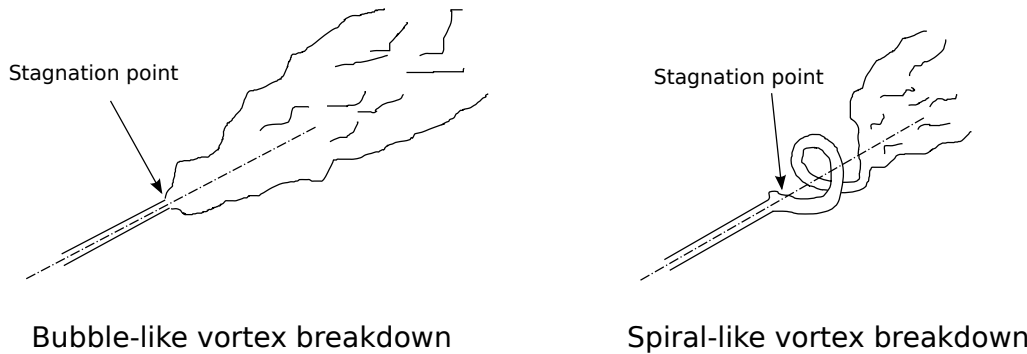
FIGURE 2.9: Vortex breakdown types, illustration following Breitsamter [87].

2.4 Vortex breakdown

Certain circumstances, which are not fully understood yet [7, 83], can lead to a significant structural change of the primary vortices known as vortex breakdown. Vortex breakdown is characterized by a significant expansion of the vortex, zero or negative streamwise velocities in the vortex core, and a strong increase in turbulence intensity. One distinguishes two forms of vortex breakdown: bubble-like and spiral-like [90]. The designations stem from the characteristic shapes of the respective forms, see Fig. 2.9.

Four common approaches to explaining vortex breakdown theoretically are [7]: (1) a quasi-cylindrical approach with an analogy to boundary layer separation, (2) a solution of the axisymmetric Navier-Stokes equations, (3) a concept of a critical state, and (4) an approach via hydrodynamic instabilities. Given that the approaches are of minor relevance for this work, they are not elaborated on here. A detailed description of the respective concepts and reviews of vortex breakdown can be found in [7] and [91].

2.5 Flow control

Vortex breakdown can be advantageous, e.g. as a means to destroy hazardous vortices or to improve mixing in combustion chambers, or disadvantageous, e.g. for aircraft, when it negatively impacts the aerodynamics and stability, and thus maneuverability, and leads to increased structural loads [83]. Research into vortex breakdown control is thus of high importance. Gursul et al. [92] and Mitchell and Délery [83] reviewed common approaches. They emphasize notably two aspects: First, the two main parameters that can be targeted to control vortex breakdown: (a) the swirl level, which is a measure
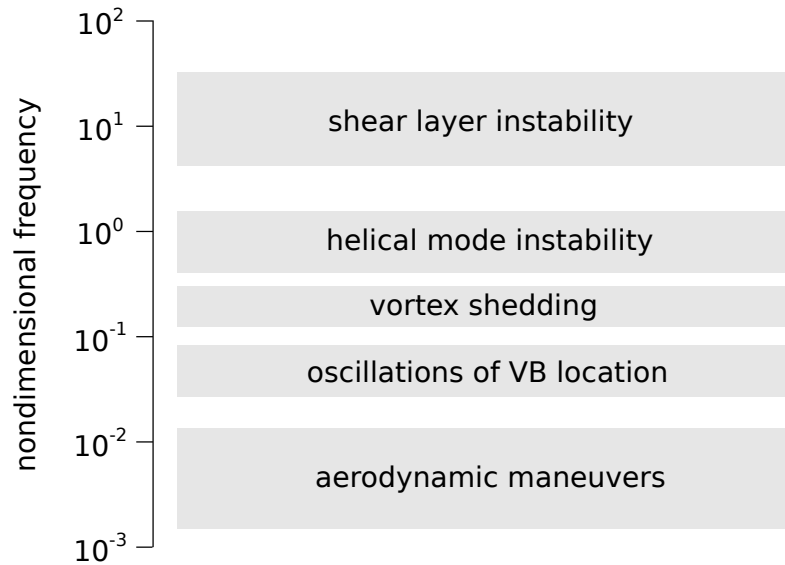
FIGURE 2.10: Characteristic frequencies in the flow field around a delta wing, following Gursul et al. [92]. Vortex shedding refers to the shedding of vortices in the post stall regime, which is not considered in this work. VB - vortex breakdown.

determined by the ratio of azimuthal to axial velocity, and (b) the pressure gradient. And second, the distinction between steady approaches and unsteady approaches, which typically employ frequencies in the range of one of the characteristic frequencies appearing in the flow field around a delta wing, see Fig. 2.10. A detailed description of the various approaches can be found in the reviews by Gursul et al. [92] and Mitchell and Délery [83].

Here, only the four mechanisms relevant for the investigations in this work are mentioned and briefly illustrated hereafter:

(1) **Placing an obstacle downstream of the wing's trailing edge**

An obstacle located downstream of the trailing edge increases the adverse pressure gradient and moves the vortex breakdown location upstream, as first demonstrated by Werlé [93]. A sketch of this approach is shown in Fig. 2.11.

(2) **Blowing along the vortex core**

Blowing along the core decreases the adverse pressure gradient and thus moves the vortex breakdown location downstream. As the previous mechanism, this was first shown by Werlé [93]. A sketch of this approach is shown in Fig. 2.12.

(3) **Trailing edge jet**

Wang et al. [94] showed that thrust-vectoring jets at the trailing edges can move
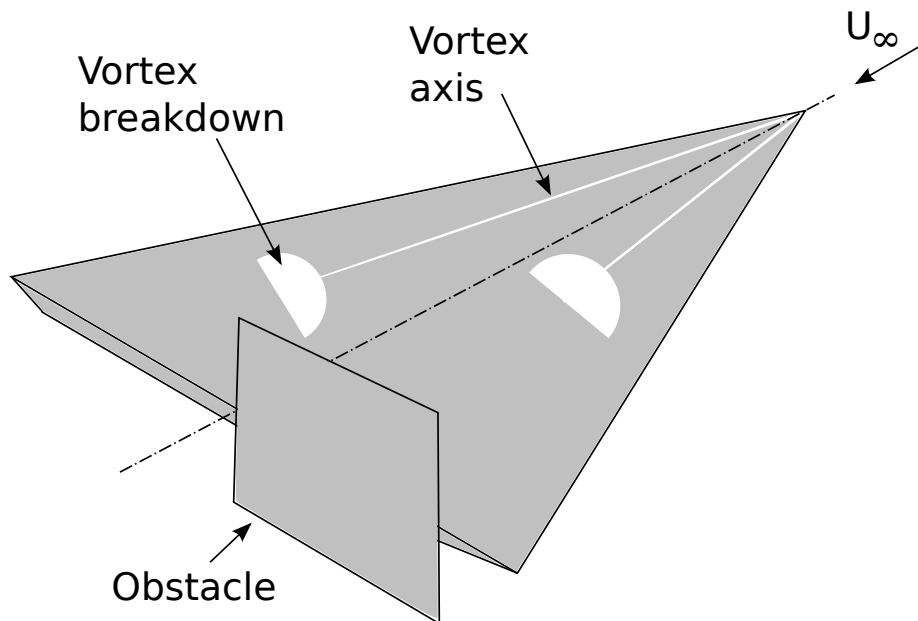
FIGURE 2.11: Flow control via obstacle downstream of trailing edge. Vortex breakdown
position moves upstream.

the vortex breakdown position upstream or downstream, depending on whether
the jet is oriented upward or downward of the wing surface, see Figs. 2.13 and
2.14.

(4) **Leading edge devices**

Leading edge devices such as flaps or other control surfaces can affect structure
and strength of the vortices [95], and, when employed in unsteady mode, e.g.
oscillating, introduce unsteady momentum into the flow and thereby control the
flow separation [96]. A sketch of this approach is shown in Fig. 2.15.
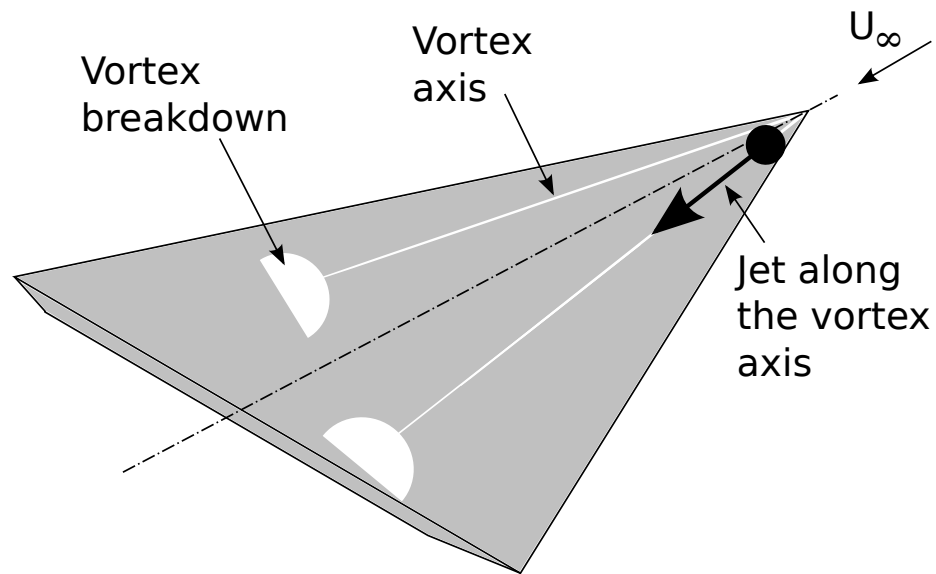
FIGURE 2.12: Flow control via blowing along the core. Vortex breakdown position moves downstream.
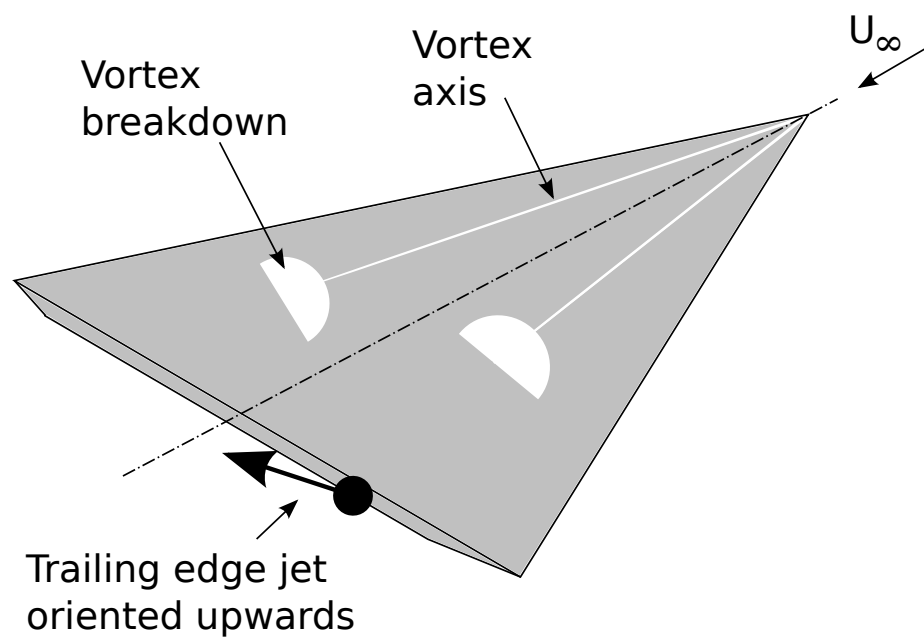
FIGURE 2.13: Flow control via blowing at the trailing edge, jet oriented upward. Vortex breakdown position moves upstream. Sketch following Wang et al. [94].
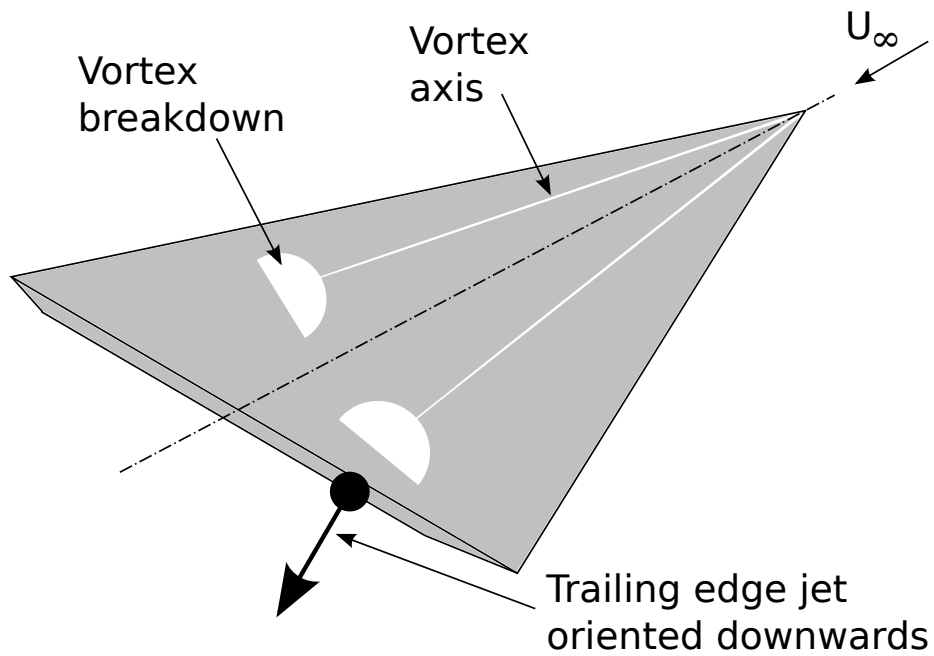
FIGURE 2.14: Flow control via blowing at the trailing edge, jet oriented downward. Vortex breakdown position moves downstream. Sketch following Wang et al. [94].
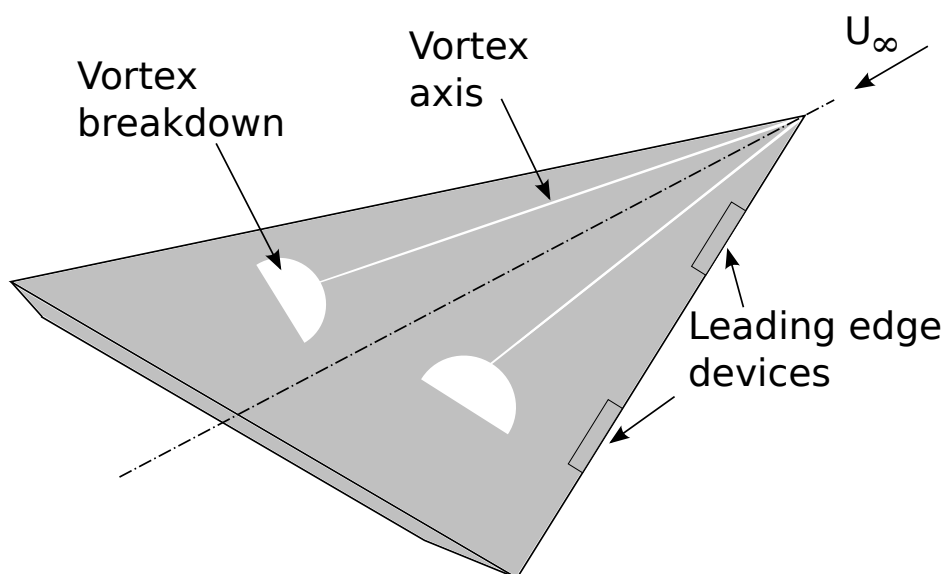
FIGURE 2.15: Flow control via leading edge devices. Vortex breakdown position can move upstream or downstream, depending on factors such as geometry, size, and movement of devices.

Chapter 3

Theory of numerical methods

This chapter outlines the numerical methods used in the investigations. It contains four sections. Section one explains the concept of implicit LES based on the adaptive local deconvolution method (ALDM). Section two provides an overview of the conservative immersed interface method (CIIM). Section three sketches adaptive mesh refinement (AMR) techniques, and section four describes the employed wall modeling (WM) approach.

3.1   Implicit LES

As described in section 1.2.3.3, only the large-scale part of the turbulent flow structures is resolved in LES. The unresolved small-scale part must be modeled in order to account for the nonlinear interactions of the unresolved small scales with the resolved large scales. Models accomplishing this are called subgrid scale (SGS) models. One distinguishes explicit and implicit SGS models. Whereas the use of explicit models necessitates the modification of the equations describing the underlying conservation law, the approach of implicit models is to use the numerical truncation error as SGS model and thus requires no explicit computation of any model terms. The idea for implicit SGS modeling originated from the observation that the numerical truncation error and the explicit SGS modeling terms are of similar magnitude [97, 98].

3.1.1   General approach of implicit LES

The general approach of implicit SGS modeling is briefly outlined hereafter, following
Hickel et al. [99], including the notation used therein. One considers the generic nonlinear
transport equation

$$\partial_t \phi + \partial_x F(\phi) = 0\,. \tag{3.1}$$

Applying a homogeneous filter G yields

$$\partial_t \overline{\phi} + G * \partial_x F(\phi) = 0\,, \tag{3.2}$$

and subsequently discretizing the equation results in

$$\partial_t \overline{\phi}_N + G * \partial_x F_N(\phi_N) = -G * \partial_x \mathcal{G}_{SGS}\,. \tag{3.3}$$

In the former equations, filtered quantities are indicated by an overbar,

$$\overline{\phi}(x) = \int\limits_{-\infty}^{+\infty} G(x - x')\phi(x')dx' = G * \phi\,, \tag{3.4}$$

and the subscript N denotes grid functions, which result from projecting continuous
functions onto the numerical grid $x_n = \{x_j\}$, $j \in \mathbb{Z}$,

$$\overline{\phi}_N = \left\{ \overline{\phi}(x_j) \right\}. \tag{3.5}$$

This projection removes all scales above the Nyquist wavenumber $\xi_N = \pi/h$, where h
designates a constant grid spacing. The nonlinear term in equation 3.3 requires the
computation of ϕ_N which is the represented part of the unfiltered field. This can be
achieved by an inverse filter operation $\phi_N = G^{-1} * \overline{\phi}_N$ on the represented part of the
field, called *soft deconvolution problem*. Note that $\phi_N \neq \phi$ due to the impossibility of
recovering non-represented scales. This irreversible projection of the nonlinear terms on
the numerical grid leads to the subgrid stress term

$$\mathcal{G}_{SGS} = F(\phi) - F_N(\phi_N) \, . \tag{3.6}$$

Modeling this term is called *hard deconvolution problem.* A variety of attempts has been made to approximate the subgrid stress term $\mathcal{G}_{SGS}$ by explicit models $\mathcal{M}_{SGS}$, i.e. $\mathcal{M}_{SGS} \approx \mathcal{G}_{SGS}$. However, every discretization scheme has a truncation error and thus the numerically computed $\overline{\phi}_N$ does not solve equation 3.3 but a modified differential equation (MDE). The MDE of a general LES discretization scheme can be written as

$$\partial_t \overline{\phi}_N + G * \partial_x F_N(\phi_N) = \mathcal{G}_N + \mathcal{G}_M - G * \partial_x \mathcal{G}_{SGS} \, , \tag{3.7}$$

where

$$\mathcal{G}_M = G * \partial_x \mathcal{G}_{SGS} - G * \partial_x \mathcal{M}_{SGS} \tag{3.8}$$

denotes the modeling error, and

$$\mathcal{G}_N = G * \partial_x F_N(\phi_N) - \check{G} * \check{\partial}_x \check{F}_N(\check{\phi}_N) + G * \partial_x \mathcal{M}_{SGS} - \check{G} * \check{\partial}_x \check{M}_{SGS} \tag{3.9}$$

denotes the truncation error. Here and in the following, numerical operators and approximate numerical solutions are denoted by a check.

As previously stated, it has been observed that $\|\mathcal{G}_N\| \approx \|G * \partial_x \mathcal{G}_{SGS}\|$ [97, 98]. The discretization of the convective fluxes can therefore negatively impact or even override the effect of subgrid scale models. In view of this observation and by considering equations 3.3 and 3.7, one notices that the truncation error $\mathcal{G}_N$ can act as SGS model, without having to explicitly compute any model terms $\mathcal{M}_{SGS}$, if it satisfies

$$\mathcal{G}_N \approx -G * \partial_x \mathcal{G}_{SGS} \tag{3.10}$$

for a finite grid spacing h, which is the idea of implicit LES.

3.1.2   Adaptive local deconvolution method (ALDM)

A systematic framework for a physically motivated implicit LES scheme was developed by Adams et al. [100] and Hickel et al. [99, 101]. It relies on a discretization scheme whose free parameters are optimized such that its numerical viscosity matches the predictions of eddy-damped quasi-normal Markovian (EDQNM) theory. A brief summary of ALDM is given hereafter, following Hickel et al. [99], including the notation used therein.

3.1.2.1   Governing equations

The compressible three-dimensional Navier-Stokes equations in integral form can be written as

$$\partial_t \overline{\boldsymbol{U}} = -\frac{1}{V_N} \oint_{\partial\Omega_N} \Big(\boldsymbol{C}(\boldsymbol{U}) + \boldsymbol{P}(\boldsymbol{U}) + \boldsymbol{D}(\boldsymbol{U}) \Big) \cdot d\boldsymbol{A} + \frac{1}{V_N} \oint_{\Omega_N} \boldsymbol{S}(\boldsymbol{U}) dV \,, \qquad (3.11)$$

with suitable initial and boundary conditions. $\overline{\boldsymbol{U}}$ denotes the solution vector of the volume-averaged conserved variables

$$\overline{\boldsymbol{U}} = \frac{1}{V_N} \int_{\Omega_N} \boldsymbol{U} dV \,, \qquad (3.12)$$

whereat $\boldsymbol{U} = \Big[\rho, \rho u_1, \rho u_2, \rho u_3, \rho E \Big]^T$ contains mass density ρ, momentum in the three coordinate directions ρu_i, and total energy ρE. Ω_N designates a control volume with volume V_N and boundary $\partial\Omega_N$. $\boldsymbol{C}(\boldsymbol{U})$, $\boldsymbol{P}(\boldsymbol{U})$, and $\boldsymbol{D}(\boldsymbol{U})$ denote the convective part of the fluxes across $\partial\Omega_N$, the surface stresses due to pressure, and the surface stresses due to viscosity, respectively:

$$\boldsymbol{C}_i = \Big[u_i\rho, u_i\rho u_1, u_i\rho u_2, u_i\rho u_3, u_i\rho E \Big]^T \,, \qquad (3.13)$$

$$\boldsymbol{P}_i = \Big[0, \delta_{i1}p, \delta_{i2}p, \delta_{i3}p, u_k\delta_{ik}p \Big]^T \,, \qquad (3.14)$$

$$\boldsymbol{D}_i = -\Big[0, \tau_{i1}, \tau_{i2}, \tau_{i3}, u_k\tau_{ik} + q_i\Big]^T .$$ (3.15)

u_i denotes the velocity in i-direction, τ_{ij} is the viscous stress tensor for a Newtonian fluid

$$\tau_{ij} = \mu(T)\Big(\partial_j u_i + \partial_i u_j - \frac{2}{3}\delta_{ij}\partial_k u_k\Big) ,$$ (3.16)

and q_i denotes the heat flux in the energy equation

$$q_i = \kappa(T)\partial_i T .$$ (3.17)

Considering an ideal gas with a Prandtl number of $Pr = \nu/\kappa = 0.72$, a ratio of specific heats of $\gamma = c_p/c_v = 1.4$, Reynolds number Re, and Mach number Ma as nondimensional flow parameters, a closure of the Navier-Stokes equations can be achieved via relations for the pressure p, temperature T, dynamic viscosity μ, and thermal diffusivity κ, notably the equation of state (EOS) of an ideal gas,

$$p = \mathcal{R}\rho T ,$$ (3.18)

with the gas constant $\mathcal{R} = \frac{1}{\gamma Ma^2}$, which, along with the definition of the internal energy,

$$\rho e = \rho E - \frac{1}{2}\rho u^2 = \frac{1}{\gamma - 1}p ,$$ (3.19)

allows for the determination of pressure and temperature. Speed of sound c, dynamic viscosity μ, and thermal conductivity κ are computed via

$$c = \sqrt{\gamma\frac{p}{\rho}} ,$$ (3.20)

$$\mu = \frac{1}{Re}T^{0.75} ,$$ (3.21)

and

$$\kappa = \frac{1}{(\gamma - 1)Ma^2 Pr}\mu(T)\,, \tag{3.22}$$

respectively. ALDM is designed based on a finite volume discretization, which can be expressed as a top-hat filter

$$G(\boldsymbol{x}, V_j) = \begin{cases} 1/V_j, & \text{for } \boldsymbol{x} \in \Omega_j \\ 0, & \text{else} \end{cases}, \tag{3.23}$$

where V_j denotes the cell volume of cell Ω_j, and it can be directly applied to equation 3.11. Note that employing this filter in equation 3.4 for $\phi = \boldsymbol{U}$ results in equation 3.12. Finite volume methods require (1) a numerical reconstruction of the unfiltered solution at the cell faces, (2) a numerical flux function utilizing the numerically reconstructed solution, and (3) a numerical discretization scheme computing face-averaged fluxes. In the following, reconstruction and flux function are briefly explained, again following Hickel et al. [99], including the notation therein.

3.1.2.2 Reconstruction

Quantities at the cell faces are reconstructed using

$$\check{\phi}^{\mp}(x_{j\pm 1/2}) = \sum_{k=1}^{K} \alpha_k \check{\phi}_k^{\mp}(x_{j\pm 1/2})\,, \tag{3.24}$$

where K is an integer whose value ($K = 3$) is explained below, α_k are currently unused free modeling parameters set to $1/K$, and the functions $\check{\phi}_k^{\mp}(x_{j\pm 1/2})$ are defined as

$$\check{\phi}_1^{\mp}(x_{j\pm 1/2}) = \check{g}_{1,0}^{\mp}(x_{j\pm 1/2})\,, \tag{3.25}$$

$$\check{\phi}_2^{\mp}(x_{j\pm 1/2}) = \sum_{r=0}^{1} \omega_{2,r}^{\mp}(\gamma_{2,r}, \overline{u}_N)\check{g}_{2,r}^{\mp}(x_{j\pm 1/2})\,, \tag{3.26}$$

$$\check{\phi}_3^{\mp}(x_{j\pm1/2}) = \sum_{r=0}^{2} \omega_{3,r}^{\mp}(\gamma_{3,r}, \overline{u}_N)\check{g}_{3,r}^{\mp}(x_{j\pm1/2}).\tag{3.27}$$

The deconvolution polynomials $\check{g}_{k,r}^{\mp}(x_{j\pm1/2})$ are defined as

$$\check{g}_{k,r}^{\mp}(x_{j\pm1/2}) = \sum_{l=0}^{k-1} c_{k,r,l}^{\mp}(x_N)\overline{\phi}(x_{j-r+l}),\tag{3.28}$$

and $\omega_{k,r}(\gamma_{k,r}, \overline{\phi}_N)$ are dynamic, solution-adaptive weight coefficients given by

$$\omega_{k,r}(\gamma_{k,r}, \overline{\phi}_N) = \frac{\gamma_{k,r}\beta_{k,r}(\overline{\phi}_N)}{\sum\limits_{s=0}^{k-1}\gamma_{k,s}\beta_{k,s}(\overline{\phi}_N)}.\tag{3.29}$$

$\gamma_{k,r}$ are free modeling parameters, and $\beta_{k,r}$ is a smoothness measure defined by

$$\beta_{k,r}(\overline{\phi}_N, x_i) = \left(\varepsilon_\beta + \sum_{l=-r}^{k-r-2}(\overline{\phi}(x_{i+m+1}) - \overline{\phi}(x_{i+m}))^2\right)^{-2},\tag{3.30}$$

with $\varepsilon_\beta = 10^{-99}$ to avoid division by zero. The coefficients $c_{k,r,l}^{\mp}$ are grid-dependent and chosen in a way that ensures

$$\check{g}_{k,r}^{\mp} = \phi(x_{j\pm1/2}) + \mathcal{O}(h^k).\tag{3.31}$$

The deconvolved solution is regularized by choosing $k \leq K = 3$, i.e. only polynomials of degree $1 \leq k \leq K$ contribute to it.

In order to limit the computational cost, a simplified adaptive local deconvolution method (SALD) was developed [102] and is employed for all computations in this work. The reconstruction scheme is applied to the cell-averaged density $\overline{\rho}$, velocity $\overline{u}_i$, pressure $\overline{p}$, and internal energy $\overline{\rho e}$, and the LES solution vector is constituted by the cell-averaged density, the resolved momentum, and the resolved total energy:

$$\overline{\boldsymbol{U}} = \left[\overline{\rho}, \overline{\rho}\,\overline{u}_1, \overline{\rho}\,\overline{u}_2, \overline{\rho}\,\overline{u}_3, \overline{\rho e} + \frac{1}{2}\overline{\rho}\,\overline{u}_k\overline{u}_k\right]^T.\tag{3.32}$$

The average pressure,

$$\overline{p} := \overline{p}(\overline{\rho}, \overline{\rho e}) \,, \tag{3.33}$$

is obtained from equation 3.18.

3.1.2.3   Numerical flux function

The numerical flux function used in ALDM has the following form:

$$\check{F}_{j\pm1/2} = F\left(\frac{\check{\phi}^+ + \check{\phi}^-}{2}\right) - R \cdot \left(\check{\phi}^+ - \check{\phi}^-\right) \,. \tag{3.34}$$

Only the hyperbolic flux $\boldsymbol{C} + \boldsymbol{P}$ is considered for the implicit SGS modeling. Gradients appearing in the viscous flux $\boldsymbol{D}$ are approximated by linear second-order schemes. The first term in equation 3.34 represents the physical flux arising from the Navier-Stokes equations and is computed using both reconstructed values at the specified cell face. The second term signifies a regularization term where the dissipation matrix R is specifically defined for the differential equation considered, see below.

Using this approach, the numerical mass density flux at any cell face is determined via

$$\check{C}_i^{\rho} = \check{u}^* \frac{\check{\rho}^+ + \check{\rho}^-}{2} - R_i^{\rho}(\check{\rho}^+ - \check{\rho}^-) \,, \tag{3.35}$$

where transport velocity $\check{u}^*$ and dissipation coefficient R_i^{ρ} are defined further below, and the numerical momentum flux at any cell face is

$$\check{C}_i^{\rho u_k} = \check{C}_i^{\rho} \frac{\check{u}_k^+ + \check{u}_k^-}{2} - R_i^{\rho u} \frac{\check{\rho}^+ + \check{\rho}^-}{2} \left(\check{u}_k^+ - \check{u}_k^-\right) \,. \tag{3.36}$$

The regularization terms in equations 3.35 and 3.36 dissipate turbulent kinetic energy from the represented scales and thereby model unresolved surface stresses. The total energy flux at any cell face is

$$\check{C}_i^{\rho e} = \check{u}^* \frac{\check{\rho}e^+ + \check{\rho}e^-}{2} + \frac{\check{u}_k^+ + \check{u}_k^-}{2} \left(\check{C}_i^{\rho u_k} - \frac{\check{u}_k^+ + \check{u}_k^-}{4} \check{C}_i^{\rho u_k} \right) - R_i^{\rho e} \left(\check{\rho}e^+ - \check{\rho}e^- \right) . \quad (3.37)$$

The pressure flux is

$$\boldsymbol{\check{P}}_i = \left[0, \delta_{i1}\check{p}^*, \delta_{i2}\check{p}^*, \delta_{i3}\check{p}^*, \check{u}_i^*\check{p}^* \right]^T , \quad (3.38)$$

with the interface pressure

$$\check{p}^* = \frac{\check{p}^+ + \check{p}^-}{2} . \quad (3.39)$$

The transport velocity introduced in equation 3.35 is defined as

$$\check{u}_i^* = \frac{\check{u}_i^+ + \check{u}_i^-}{2} - \frac{1}{\check{c}} \frac{\check{p}_3^+ - \check{p}_3^-}{\check{\rho}^+ + \check{\rho}^-} , \quad (3.40)$$

where $\check{c}$ denotes the maximum speed of sound in adjacent cells, and $\check{p}_3^\pm$ are the third-order pressure reconstruction polynomials.

The dissipation matrix is given by

$$\boldsymbol{R}_i = \left[\sigma^\rho |\check{u}_i^+ - \check{u}_i^-|, \sigma^{\rho u} |\check{u}_1^+ - \check{u}_1^-|, \sigma^{\rho u} |\check{u}_2^+ - \check{u}_2^-|, \sigma^{\rho u} |\check{u}_3^+ - \check{u}_3^-|, \sigma^{\rho e} |\check{u}_i^+ - \check{u}_i^-| \right]^T , \quad (3.41)$$

with the case-independent model parameters $\sigma^\rho, \sigma^{\rho u}$, and $\sigma^{\rho e}$.

Taken together, reconstruction scheme and numerical flux function provide a set of free parameters $\{\alpha, \gamma, \sigma\}$, which is chosen in such a way that the truncation error constitutes a physically motivated SGS model. The set of parameters is determined via an optimization problem described in [101] and [99], and its values are given in table 3.1.

ALDM can also deal with shock waves, which is accomplished by detecting discontinuities via the sensor functional

TABLE 3.1: Model parameters of ALDM for compressible flows, taken from [99].

Parameter	Value
α_1	$(1 - f_s)/3$
α_2	$(1 - f_s)/3$
α_3	$1 - \alpha_1 - \alpha_2$
$\gamma_{2,0}^{+}$	1
$\gamma_{2,1}^{+}$	1
$\gamma_{3,0}^{+}$	$0.01902 + f_s(0.3 - 0.01902)$
$\gamma_{3,1}^{+}$	$0.08550 + f_s(0.6 - 0.08550)$
$\gamma_{3,2}^{+}$	$1 - \gamma_{3,0}^{+} - \gamma_{3,1}^{+}$
$\gamma_{2,1}^{-}$	$\gamma_{3,0}^{+}$
$\gamma_{2,0}^{-}$	$\gamma_{3,1}^{+}$
$\gamma_{3,2}^{-}$	$\gamma_{3,0}^{+}$
$\gamma_{3,1}^{-}$	$\gamma_{3,1}^{+}$
$\gamma_{3,0}^{-}$	$\gamma_{3,2}^{+}$
σ^{ρ}	0.615
$\sigma^{\rho u}$	0.125
$\sigma^{\rho e}$	0.615

$$f_s = \begin{cases} 1, & \frac{|\nabla \cdot \overline{u}|}{|\nabla \cdot \overline{u}| + \|\nabla \times \overline{u}\| + \varepsilon} \geq 0.95 \\ 0, & \text{else} \end{cases}, \tag{3.42}$$

and adding the term

$$f_s \frac{|\breve{u}_i^*| + |\breve{u}_i^+ - \breve{u}_i^-|}{2}[1, 1, 1, 1, 1]^T \tag{3.43}$$

to the dissipation matrix $\boldsymbol{R}_i$ given in equation 3.41. The treatment of shock waves is of no relevance for this work, however, since shock waves do not appear for the considered free stream conditions ($Re = 2 \cdot 10^6$, $Ma = 0.14$).

3.2   Immersed boundary technique

The previously described implicit LES approach is based on Cartesian grids. Therefore, an immersed boundary (IB) technique is required to represent complex geometries, such as a delta wing. Generally, IB techniques have two main advantages [103]: First,

the process of generating proper body-fitted grids is avoided, which can be very time-consuming and thus is particularly undesirable when grid regeneration is needed, e.g. in case of moving or deforming boundaries. Second, the accuracy of the discretization scheme is not affected by limited grid regularity, i.e. smoothness and orthogonality, which is particularly important when employing implicit LES, where the spatial truncation error models the subgrid scales. IB techniques can be considered as well developed, reviews are given in [104] and [103]. In this study, the conservative immersed interface method (CIIM) for compressible flows developed by Grilli et al. [105] is used. It is briefly described hereafter, following Grilli et al. [105], including the notation used therein.

3.2.1 Conservative immersed interface method (CIIM)

3.2.1.1 Mathematical basis

One considers an interface $\Gamma(t)$, representing the geometry of interest, which is described by a level set field Φ. $\Gamma(t)$ divides the computational domain Ω into two domains: Ω_1, denoting the domain occupied by the fluid, and Ω_2, denoting the domain occupied by the solid. The computational domain is discretized using a Carstesian grid with grid spacings Δx, Δy, and Δz leading to computational cells (i,j,k) whose fluid volume $V_{i,j,k} \cap \Omega_1(t)$ can be computed by $\alpha_{i,j,k}(t)\Delta x \Delta y \Delta z$. $\alpha_{i,j,k}$ denotes the fluid volume fraction. Approximating time integration by a forward Euler scheme, one can express equation 3.11 for a cut cell as

$$
\begin{aligned}
\Delta x \Delta y \Delta z \left(\alpha_{i,j,k}^{n+1}\overline{\boldsymbol{U}}_{i,j,k}^{n+1} - \alpha_{i,j,k}^{n}\overline{\boldsymbol{U}}_{i,j,k}^{n} \right) = {} & \Delta t \Delta y \Delta z \left[A_{i,j,k}^{12}\boldsymbol{F}_{i,j,k}^{12} - A_{i,j,k}^{11}\boldsymbol{F}_{i,j,k}^{11} \right] \\
& + \Delta t \Delta x \Delta z \left[A_{i,j,k}^{22}\boldsymbol{F}_{i,j,k}^{22} - A_{i,j,k}^{21}\boldsymbol{F}_{i,j,k}^{21} \right] \\
& + \Delta t \Delta x \Delta z \left[A_{i,j,k}^{32}\boldsymbol{F}_{i,j,k}^{32} - A_{i,j,k}^{31}\boldsymbol{F}_{i,j,k}^{31} \right] \\
& + \Delta t \boldsymbol{X}_{i,j,k}(\Delta\Gamma_{i,j,k}(t)),
\end{aligned}
\tag{3.44}
$$

where $A_{i,j,k}^{lm}$ represent the cell face apertures, see Fig. 3.1, $\Delta\Gamma_{i,j,k}(t) = \Gamma(t) \cap V_{i,j,k}$ denotes the interface segment, $\boldsymbol{F}_{i,j,k}^{lm}$ represent the average fluxes across a cell face, and $\boldsymbol{X}_{i,j,k}$ denotes the integral momentum and energy exchange across the interface. For cells
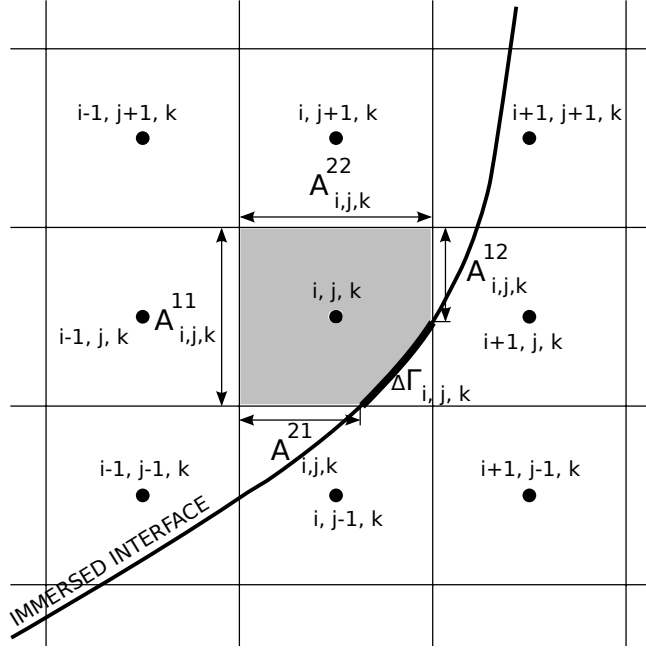
FIGURE 3.1: Two dimensional illustration of the conservative discretization of a cut cell, following Grilli et al. [105]. The volume fraction $\alpha_{i,j,k}$ is determined by dividing the shaded area by the total area of cell i, j, k.

that are not cut by the interface one has $\alpha_{i,j,k} = A^{lm}_{i,j,k} = 1$, and $\Delta\Gamma_{i,j,k}(t) = \Gamma(t) \cap V_{i,j,k} = 0$, and thus obtains

$$
\begin{aligned}
\Delta x \Delta y \Delta z \left(\overline{\boldsymbol{U}}^{n+1}_{i,j,k} - \overline{\boldsymbol{U}}^{n}_{i,j,k} \right) = {} & \Delta t \Delta y \Delta z \left[\boldsymbol{F}^{12}_{i,j,k} - \boldsymbol{F}^{11}_{i,j,k} \right] \\
& + \Delta t \Delta x \Delta z \left[\boldsymbol{F}^{22}_{i,j,k} - \boldsymbol{F}^{21}_{i,j,k} \right] \\
& + \Delta t \Delta x \Delta z \left[\boldsymbol{F}^{32}_{i,j,k} - \boldsymbol{F}^{31}_{i,j,k} \right] .
\end{aligned}
\tag{3.45}
$$

3.2.1.2   Interface exchange term

The interface interaction term $\boldsymbol{X}_{i,j,k}$ can be decomposed into three contributions

$$
\boldsymbol{X}_{i,j,k}(\Delta\Gamma_{i,j,k}) = \boldsymbol{X}^p + \boldsymbol{X}^v + \boldsymbol{X}^{ht},
\tag{3.46}
$$

i.e. a contribution from pressure $\boldsymbol{X}^p$, a contribution from viscous effects $\boldsymbol{X}^v$, and a contribution from heat transfer $\boldsymbol{X}^{ht}$.

Pressure term $\boldsymbol{X}^p$

The term $\boldsymbol{X}^p$ can be expressed as

$$\boldsymbol{X}^p = \left[0,\, p_\Gamma \Delta\Gamma(t) n_1^\Gamma,\, p_\Gamma \Delta\Gamma(t) n_2^\Gamma,\, p_\Gamma \Delta\Gamma(t) n_3^\Gamma,\, p_\Gamma \Delta\Gamma(t)(\boldsymbol{n}^\Gamma \cdot \boldsymbol{v}^\Gamma)\right]^T, \qquad (3.47)$$

where p_Γ is the interface pressure obtained by solving a Riemann problem

$$\mathcal{R}(\overline{\boldsymbol{U}}, \boldsymbol{v}_n^\Gamma) = 0 \qquad (3.48)$$

for the pressure on the interface segment, as described in [106]. Here, $\boldsymbol{v}_n^\Gamma = \boldsymbol{v}^\Gamma \boldsymbol{n}^\Gamma$ denotes the component of the interface velocity in the direction of the local interface normal vector $\boldsymbol{n}^\Gamma = \left[n_1^\Gamma, n_2^\Gamma, n_3^\Gamma\right]$.

Viscous term $\boldsymbol{X}^v$

The viscous term arises from the friction force $\boldsymbol{D}$ which can be computed via

$$\boldsymbol{D} = \int_{\Delta\Gamma(t)} \overline{\boldsymbol{\tau}} \cdot \boldsymbol{n}^\Gamma dS. \qquad (3.49)$$

The components of the viscous stress tensor $\overline{\boldsymbol{\tau}}$ are given by equation 3.16. Using simplifying assumptions, see Grilli et al. [105], the viscous force can be approximated by

$$\boldsymbol{D} = \int_{\Delta\Gamma(t)} \overline{\boldsymbol{\tau}} \cdot \boldsymbol{n}^\Gamma dS \approx \left[\frac{4}{3}\mu \frac{\partial u_n}{\partial n}, \frac{\partial u_t}{\partial n}, \frac{\partial u_p}{\partial n}\right]^T \Delta\Gamma(t), \qquad (3.50)$$

where (n, t, p) signifies a local reference system depicted in Fig. 3.2, or

$$\boldsymbol{D} = \int_{\Delta\Gamma(t)} \overline{\boldsymbol{\tau}} \cdot \boldsymbol{n}^\Gamma dS \approx \mu \left(\frac{4}{3}\frac{\partial \boldsymbol{u}^\parallel}{\partial n} + \frac{\partial \boldsymbol{u}^\perp}{\partial n}\right) \Delta\Gamma(t), \qquad (3.51)$$

when using normal $(\boldsymbol{u}^\perp)$ and tangential part $(\boldsymbol{u}^\parallel)$ of the local volume averaged velocity $\overline{\boldsymbol{u}}$:
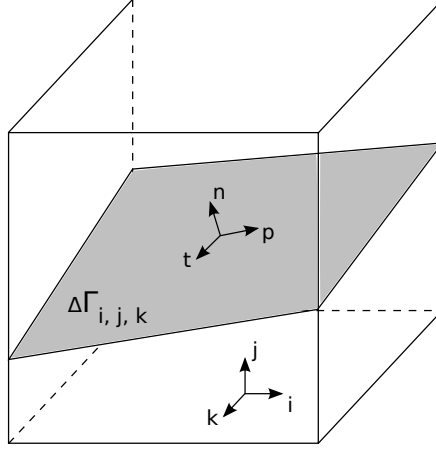
FIGURE 3.2: Illustration of local reference system of a cut cell, following Grilli et al. [105].

$$\overline{\boldsymbol{u}} = \boldsymbol{u}^{\parallel} + \boldsymbol{u}^{\perp} \,, \tag{3.52}$$

$$\boldsymbol{u}^{\perp} = \left(\overline{\boldsymbol{u}} \cdot \boldsymbol{n}^{\Gamma}\right) \cdot \boldsymbol{n}^{\Gamma} \,, \tag{3.53}$$

$$\boldsymbol{u}^{\parallel} = \overline{\boldsymbol{u}} = \boldsymbol{u}^{\perp} \,. \tag{3.54}$$

The velocity gradient in equation 3.51 can be approximated by a wall model, see section 3.4, or by a simple linear approximation. For the linear approximation, one computes the velocity and viscosity at point P'' via an interpolation scheme and obtains

$$\boldsymbol{D} = \mu \left(\frac{4}{3} \frac{\boldsymbol{u}_{P''}^{\parallel} - \boldsymbol{v}^{\Gamma}}{\Delta h} + \frac{\boldsymbol{u}_{P''}^{\perp} - \boldsymbol{v}^{\Gamma}}{\Delta h} \right) \Delta \Gamma(t) \,. \tag{3.55}$$

P'' is specified by the foot point P', the normal vector $\boldsymbol{n}^{\Gamma}$, and the length scale

$$\Delta h = \sqrt{(\Delta x n_1^{\Gamma})^2 + (\Delta y n_2^{\Gamma})^2 + (\Delta z n_3^{\Gamma})^2} \,, \tag{3.56}$$

see Fig. 3.3.

Introducing the term C
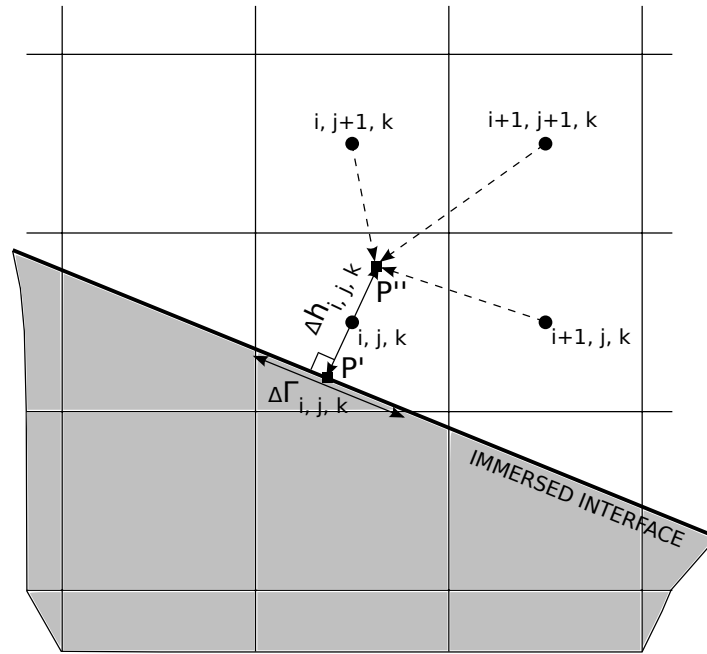
FIGURE 3.3: Two dimensional illustration of interpolation procedure for immersed boundary, following Grilli et al. [105]. Shaded area indicates solid, white area indicates fluid.

$$C = \int\limits_{\Delta\Gamma(t)} \left(\overline{\boldsymbol{\tau}} \cdot \boldsymbol{v}^{\Gamma} \right) \cdot d\boldsymbol{S} \approx \boldsymbol{D} \cdot \boldsymbol{v}^{\Gamma} \,, \tag{3.57}$$

effective only in case of moving boundaries, the viscous term $\boldsymbol{X}^v$ can be expressed as

$$\boldsymbol{X}^v = \left[0, D_1, D_2, D_3, C \right]^T . \tag{3.58}$$

Heat transfer term $\boldsymbol{X}^{ht}$

The heat transfer term $\boldsymbol{X}^{ht}$ can be expressed by

$$\boldsymbol{X}^{ht} = \left[0, 0, 0, 0, q \right]^T , \tag{3.59}$$

where q denotes the heat transfer across the interface segment and is computed by

$$q = \int\limits_{\Delta\Gamma(t)} k\nabla T \cdot d\boldsymbol{S} \,. \tag{3.60}$$

Using simplifying assumptions (see [105]) it can be written as

$$q = \int\limits_{\Delta\Gamma(t)} k\nabla T \cdot d\boldsymbol{S} \approx k\frac{\partial T}{\partial n}\Delta\Gamma(t) \approx k\frac{T^{P''} - T^{\Gamma}}{\Delta h}\Delta\Gamma(t)\,, \tag{3.61}$$

where k is the thermal conductivity evaluated in point P'', $T^{P''}$ is the temperature in point P'', and T^{Γ} denotes the fixed wall temperature. Note that $\boldsymbol{X}^{ht}$ is nonzero only in case of an isothermal wall boundary condition. For an adiabatic wall, which is assumed in the investigations in this work, one has $\nabla T \cdot \boldsymbol{n} = 0$ and thus $q = 0$ and $\boldsymbol{X}^{ht} = \left[0,0,0,0,0\right]^{T}$.

3.2.1.3   Mixing procedure

An arbitrary geometry can lead to cut cells containing only a very small fluid fraction. Such cells may cause the following problem: a time step determined based on a general non-cut cell may be too large to ensure a correct computation of the quantities in the considered cell, and a time step determined based on the actual cell dimensions of such cells may be extremely small, thereby making simulations prohibitively expensive in view of the available computational resources. In order to remedy this problem, conserved quantities of such small cells are mixed with the respective quantities in larger neighboring cells. This procedure is called conservative mixing. The implementation described hereafter, following Grilli et al. [105], is based on work by Hu et al. [106].

Only cells with a volume fraction smaller than a certain threshold, in this work $\alpha_{th} = 0.6$, are mixed with neighboring cells. A smaller threshold leads to a higher accuracy in the interface region but lowers the numerical stability. The quantities of a cut cell (i,j,k) with $\alpha_{i,j,k} < \alpha_{th}$ are computed using seven neighboring cells, which are called target cells (hereafter denoted by trg) and determined based on the local interface normal vector, via

$$\overline{\boldsymbol{U}}_{i,j,k} = \left(\overline{\boldsymbol{U}}_{i,j,k}\right)^{*} + \frac{\boldsymbol{M}^{trg}_{i,j,k}}{\alpha^{n}_{i,j,k}V_{i,j,k}}\,. \tag{3.62}$$

In the above equation, $\left(\overline{\boldsymbol{U}}_{i,j,k}\right)^{*}$ denotes quantities of the cut cell (i,j,k) before applying the mixing procedure, and $\boldsymbol{M}^{trg}_{i,j,k}$ denotes the mixing flux determined by

$$\boldsymbol{M}_{i,j,k}^{trg} = \frac{\beta_{i,j,k}^{trg}\big[(V_{trg}\alpha_{trg}\overline{\boldsymbol{U}}_{trg})V_{i,j,k}\alpha_{i,j,k} - (V_{i,j,k}\alpha_{i,j,k}\overline{\boldsymbol{U}}_{i,j,k})V_{trg}\alpha_{trg}\big]}{\alpha_{i,j,k}V_{i,j,k}\beta_{i,j,k}^{trg} + \alpha_{trg}V_{trg}}\,. \tag{3.63}$$

The weights $\beta_{i,j,k}^{trg}$ for each target cell are determined via

$$
\begin{aligned}
\beta_{i,j,k}^{x} &= |n_1^{\Gamma}|^2 \alpha_{mix_i,j,k}\,, \\
\beta_{i,j,k}^{y} &= |n_2^{\Gamma}|^2 \alpha_{i,mix_j,k}\,, \\
\beta_{i,j,k}^{z} &= |n_3^{\Gamma}|^2 \alpha_{i,j,mix_k}\,, \\
\beta_{i,j,k}^{xy} &= |n_1^{\Gamma} n_2^{\Gamma}| \alpha_{mix_i,mix_j,k}\,, \\
\beta_{i,j,k}^{xz} &= |n_1^{\Gamma} n_3^{\Gamma}| \alpha_{mix_i,j,mix_k}\,, \\
\beta_{i,j,k}^{yz} &= |n_2^{\Gamma} n_3^{\Gamma}| \alpha_{i,mix_j,mix_k}\,, \\
\beta_{i,j,k}^{xyz} &= |n_1^{\Gamma} n_2^{\Gamma} n_3^{\Gamma}|^{2/3} \alpha_{mix_i,mix_j,mix_k}\,,
\end{aligned}
\tag{3.64}
$$

and subsequent normalization

$$\beta_{i,j,k}^{x} + \beta_{i,j,k}^{y} + \beta_{i,j,k}^{z} + \beta_{i,j,k}^{xy} + \beta_{i,j,k}^{xz} + \beta_{i,j,k}^{yz} + \beta_{i,j,k}^{xyz} = 1\,. \tag{3.65}$$

Quantities of target cells are computed via

$$\overline{\boldsymbol{U}}_{trg} = \big(\overline{\boldsymbol{U}}_{trg}\big)^* - \frac{\boldsymbol{M}_{i,j,k}^{trg}}{\alpha_{trg}^{n}V_{trg}}\,, \tag{3.66}$$

so that conservativity is ensured. As before, $\big(\overline{\boldsymbol{U}}_{trg}\big)^*$ denotes quantities of the target cells before mixing. The described procedure is employed before each time step and Runge-Kutta substep.

3.2.1.4 Extending procedure

Conserved quantities are extrapolated across the interface into a ghost-cell by determining a steady-state solution to

$$\frac{\partial \boldsymbol{U}}{\partial t_f} - \boldsymbol{n} \cdot \nabla \boldsymbol{U} = 0 \tag{3.67}$$
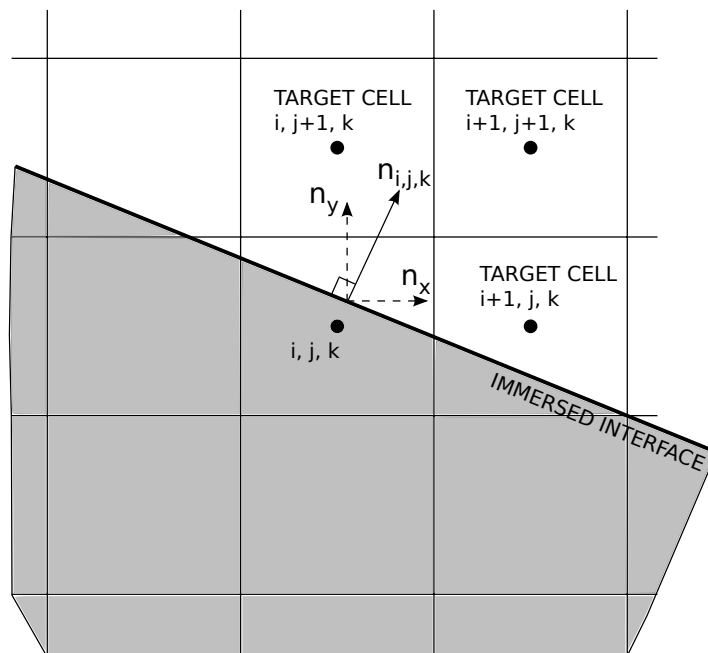
FIGURE 3.4: Two dimensional illustration of mixing procedure for immersed boundary, following Grilli et al. [105]. Shaded area indicates solid, white area indicates fluid.

to ensure that unmodified stencils can be used for the reconstruction scheme near the interface and to ensure physically reasonable conditions for newly formed cells. t_f in equation 3.67 denotes a pseudo-time. In case of an adiabatic wall boundary condition, as given in the investigations of this work, all thermodynamic quantities are extended across the interface using the decribed procedure. Further details, notably regarding isothermal wall boundary conditions, can be found in the work of Grilli et al. [105].

3.2.2 Implementation

Below, the general approach for one time step (or Runge-Kutta substep) is outlined, as given by Grilli et al. [105]:

Step 0 The level-set field is computed given the geometrical input data.

Step 1 Cut cells and their face apertures and volume fractions are determined.

Step 2 The mixing procedure is employed for all cut cells having a volume fraction below the threshold value.

Step 3 The extending procedure is applied in the interface region.

Step 4 The convective and diffusive fluxes are computed for all cells disregarding the interface.

Step 5 The fluxes of cut cells are modified by accounting for the cell face apertures and the interface interaction term.

Step 6 The flux divergence is computed.

Step 7 Level-set field and solution are advanced in time.

Note that step 0 has to be performed only once, at the beginning of the simulation, and in case of stationary boundaries, step 1 also has to be performed only once, at the beginning of the simulation.

3.3 Adaptive mesh refinement (AMR)

In many simulations of wall-bounded flows the required grid resolution in the near wall region is very high, particularly when considering Reynolds numbers typical for engineering flows. By contrast, a coarse grid may suffice to accurately predict the relevant flow features in other regions of the computational domain, e.g. the far field. In view of the limited computational resources available, a common approach is to generate grids that are sufficiently fine in the near wall region and other regions of particular interest, but coarse and thus computationally beneficial in areas such as the far field. To this end, an adaptive mesh refinement technique is adopted in this work.

For the code used in this investigation, the computational domain is initially composed of one or more cuboid blocks, each defined by the locations of its vertices, the number of cells in each coordinate direction, N_x, N_y, and N_z, and possibly a non uniform distribution of the cells. However, only uniform grid spacings in each coordinate direction have been employed throughout the investigations in this work. Blocks are then refined, coarsened, or split, which is determined by a chosen refinement criterion. The code provides a variety of possible refinement criteria, i.a. a criterion based on the size of cut cells and a criterion based on the size of cells within a specified distance from the wall, which are the criteria primarily employed in this study. Other parameters of the refinement procedure are refinement ratio, which was set to 2 for all simulations carried

out in this work, maximum refinement level, and minimum cell size. The refinement algorithm ensures that the refinement level of neighboring blocks differs by one or less, thereby limiting the inhomogeneity of the generated grids. Flow quantities of neighboring blocks are exchanged by means of buffer cells. In case of differing refinement levels, this process necessitates conservative interpolation or restriction procedures.

Details regarding the grid generation process for the simulations carried out in this work are given in section 4.3.

3.4   Wall modeling

The idea behind wall modeling is to circumvent the prohibitive grid resolution requirement of wall resolved LES by modeling the wall layer with simplified equations. Generally, some information from the exterior LES is used by the wall model, e.g. as a boundary condition, and the wall model then feeds back some information to the exterior flow. Imposing the wall shear stress as a boundary condition on the exterior flow has proven effective [45]. Reviews of wall models are given by Piomelli and Balaras [45] and Piomelli [82]. Following Chen [107], a general wall stress model can be expressed as

$$\boldsymbol{\tau}_w = f(\boldsymbol{u}_0, p_0, \nu, \boldsymbol{x}_0).$$
(3.68)

In the above equation, f designates any kind of mapping relating the wall stresses in wall-tangential directions $\boldsymbol{\tau}_w$ to the velocity $\boldsymbol{u}_0$ and the pressure p_0 at the coupling position $\boldsymbol{x}_0 = (x_{1,0}, x_{2,0}, x_{3,0})$.

3.4.1   Simplified turbulent boundary layer equations (TBLE)

In this work, wall modeling based on the simplified turbulent boundary layer equations (TBLE) as suggested by Chen [107] is used, and thus f represents a set of differential equations. Hereafter, the TBLE based wall model is briefly described, following Chen [107]. The TBLE are given by

$$\frac{\partial u_i}{\partial t} + \frac{\partial u_i u_j}{\partial x_j} = -\frac{1}{\rho}\frac{\partial p}{\partial x_i} + \nu\frac{\partial^2 u_i}{\partial x_2^2},$$
(3.69)

with $i = 1, 3$ denoting the wall-tangential directions and $i = 2$ the wall-normal direction, respectively. In this work, in addition to neglecting the convective terms as done by Chen [107], the pressure gradient term is omitted, too. The latter simplification is adopted in view of the findings of Hickel et al. [108], who showed that the convective terms and the pressure gradient term must be kept or omitted with each other, and not independently, for consistency reasons. Employing a damped mixing-length eddy-viscosity model to account for near wall turbulence, the resulting simplified TBLE are

$$\frac{\partial u_i}{\partial t} = \frac{\partial}{\partial x_2}(\nu + \nu_t)\frac{\partial u_i}{\partial x_2}\,, \tag{3.70}$$

with $i = 1, 3$ and

$$\nu_t = \kappa x_2 u_\tau (1 - e^{(-x_2^+/A)})^2\,, \tag{3.71}$$

with $\kappa = 0.4$, $A = 19.0$, and $x_2^+ = x_2 u_\tau/\nu$. As described in [107], equation 3.71 is solved numerically on an embedded grid between the wall and the interpolation point $\boldsymbol{x}_0$. At the wall, a no-slip boundary condition is imposed. At the interpolation point, boundary conditions for the velocity are imposed using the interpolated values from the exterior LES. A second-order centered discretization scheme leads to a tridiagonal system of linear equations which is solved by a tridiagonal matrix algorithm at every Runge-Kutta substep.

3.4.2 Wall modeling in conjunction with CIIM

Considering complex geometries represented by CIIM, the boundaries are in general not aligned with the background Cartesian grid, and thus further manipulations are needed in order to be able to compute the wall shear stresses by a wall model in conjunction with CIIM. Notably, a coupling position $\boldsymbol{x}_0$ and flow quantities at this coupling position have to be determined, and two wall tangential directions, denoted by $\boldsymbol{t}_1$ and $\boldsymbol{t}_3$, must be defined. The coupling point's coordinate can be expressed by

$$\boldsymbol{x}_0 = \boldsymbol{x}_w + \boldsymbol{n}d\,, \tag{3.72}$$
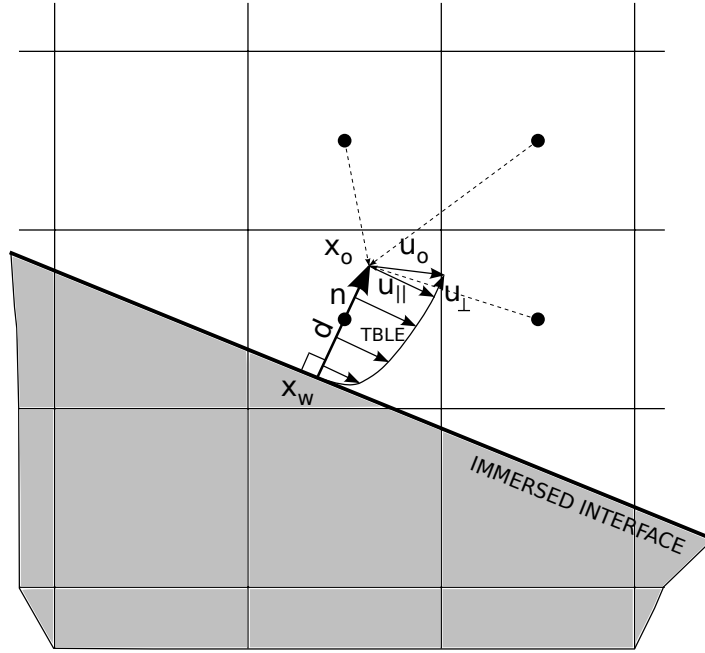
FIGURE 3.5: Illustration of wall modeling in conjunction with immersed boundary.

where $\boldsymbol{x}_w$ signifies the projection of the cut cell center on the interface, $\boldsymbol{n}$ denotes the interface normal vector, and d is a distance defined by

$$d = 1.5 \cdot min\Big(\Delta x, \Delta y, \Delta z\Big) . \tag{3.73}$$

$\boldsymbol{t}_1$ is defined by the intersection of one axis of the Cartesian coordinate system and the wall-tangential plane defined by the interface normal vector. $\boldsymbol{t}_3$ can then be determined via

$$\boldsymbol{t}_3 = \boldsymbol{t}_1 \times \boldsymbol{n} . \tag{3.74}$$

Flow quantities at $\boldsymbol{x}_0$ are computed based on surrounding grid points via an interpolation scheme, see [107]. The velocity gradients can then be determined by the wall model and used directly as an improved approximation of the velocity gradient in equation 3.50. A sketch of the wall modeling approach in conjunction with CIIM is shown in Fig. 3.5.

Chapter 4

Realization of simulations

This chapter gives details regarding the realization of the simulations. It contains five sections. Section one provides information concerning the implementation of the numerical methods described in the previous chapter. Section two describes the wing geometry, and section three provides a general description of the process of grid generation and the grids used. Section four specifies the chosen boundary and initial conditions, and section five describes the compute system used to carry out the simulations.

4.1   Code

The methods described in chapter 3 are implemented in the flow solver INCA, which is a continuously developed and extended research code written in Fortran. INCA is parallelized (MPI and OpenMP) allowing simulations with several thousand processors [109]. The code has been successfully validated and applied to a variety of problems, i.a. turbulent channel flow with and without periodic constrictions [110], flow around a cylinder [111], flows involving shock waves [112–114], cavitating flows [115], stratified flows [116], and aerodynamic configurations [117–119]. INCA provides a large number of solvers for linear problems, time integration schemes, and discretization methods. All simulations presented in this work have been conducted using a three-step Runge-Kutta scheme for time integration and the simplified adaptive local deconvolution method (SALD) for the discretization of the advective terms. An ideal gas with a ratio of specific heats of $\gamma = 1.4$ and a Prandtl number of $Pr = 0.72$ is assumed, and all simulations

have been carried out for a Reynolds number based on the mean aerodynamic chord $(2/3 \, c_r)$ of $Re = 2.0 \cdot 10^6$ and a Mach number of $Ma = 0.14$.

4.2   Wing geometry

The VFE-2 delta wing has a leading edge sweep of $65°$, a flat plate main part, and four types of interchangeable leading edges, see Figs. 4.1 and 4.2. The whole wing geometry is described by analytical formulas. Further details regarding the geometry are given in [120]. In this work, only sharp leading edge (SLE) and medium radius round leading edge (MRLE) have been considered. The delta wing's geometry is mapped onto the Cartesian grid by the immersed boundary technique described in 3.2 and, for this reason, has to be represented by an STL (Stereolithography) file. The STL files, see Fig. 4.3, have been generated using the 3D CAD design software CATIA. Rear part and length of the sting are slightly different for the two geometries, the discrepancies have no relevant effect on the results, however.

4.3   Computational grids

The computational domain is cubic and has a side length of ten root chords (c_r). The center of the cube is located at $(x_g/c_r, y_g/c_r, z_g/c_r) = (1, 0, 0)$, the wing tip is located at $(x_g/c_r, y_g/c_r, z_g/c_r) = (x/c_r, y/c_r, z/c_r) = (0, 0, 0)$. Subscript g denotes the global coordinate system, no subscript denotes the wing-fixed coordinate system, which is obtained by rotating the global coordinate system around the y_g-axis by the angle of attack α. A sketch of the setup is shown in Fig. 4.5. Simulations with coarse grids and experiences with other simulations showed that the chosen domain size is sufficiently large to exclude boundary effects.

For each configuration, i.e. angle of attack and leading edge geometry, a separate grid was generated using the AMR techniques outlined in 3.3. At first, one block covering the entire simulation domain with eight cells in each coordinate direction is used. It is refined using a cut-cell criterion, a refinement ratio of two, and a maximum refinement level of six, leading to a grid hereafter denoted by Grid 1. Then, the grid is further refined in the region close to the wall using a wall distance criterion, i.e. the cell size within a
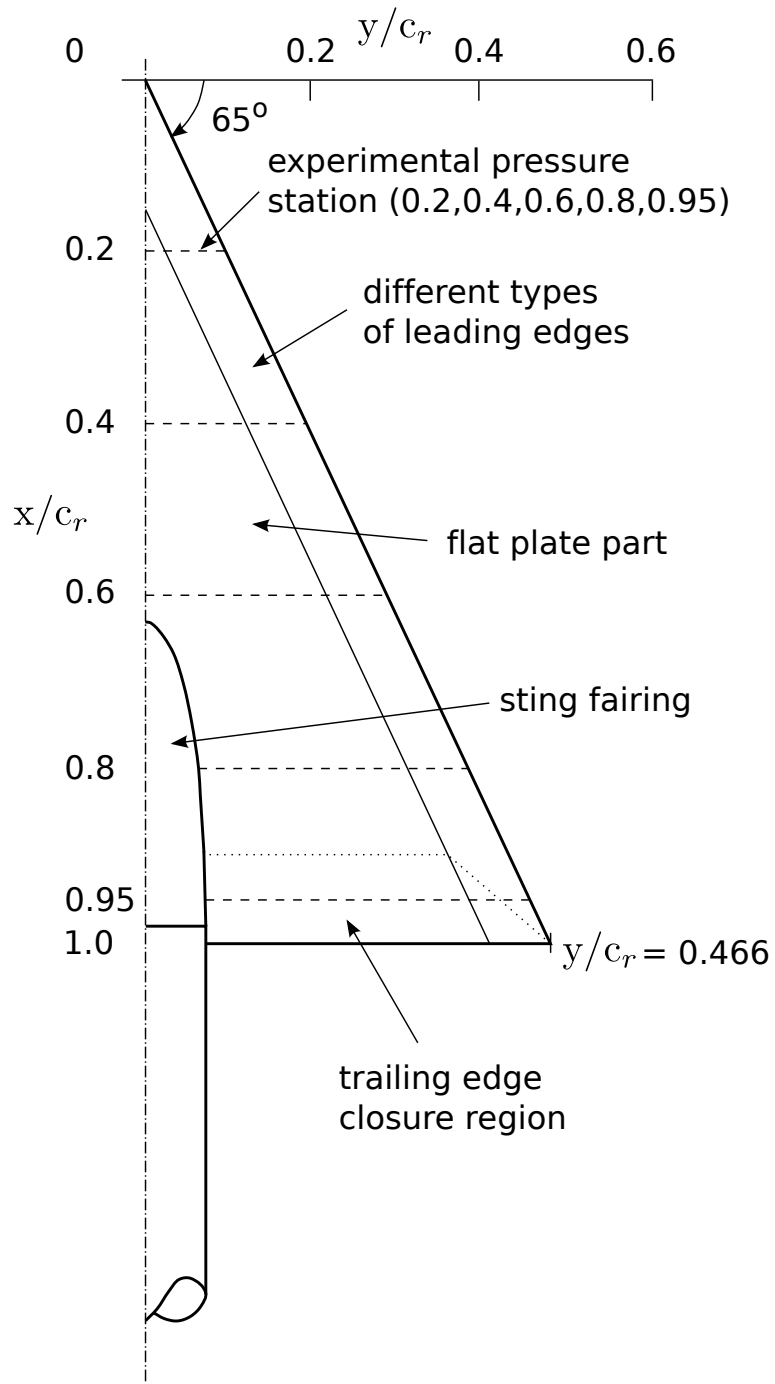
FIGURE 4.1: Basic geometry of VFE-2 delta wing model, illustration following [120].
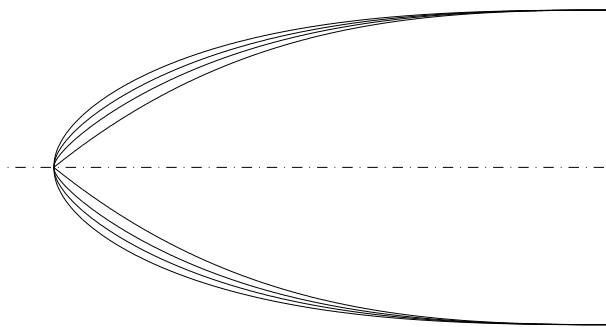
FIGURE 4.2: Basic geometry of VFE-2 delta wing leading edge types [120]. The four types are, with increasing leading edge radius: sharp leading edge (SLE), small radius leading edge (SRLE), medium radius leading edge (MRLE), and large radius leading edge (LRLE).
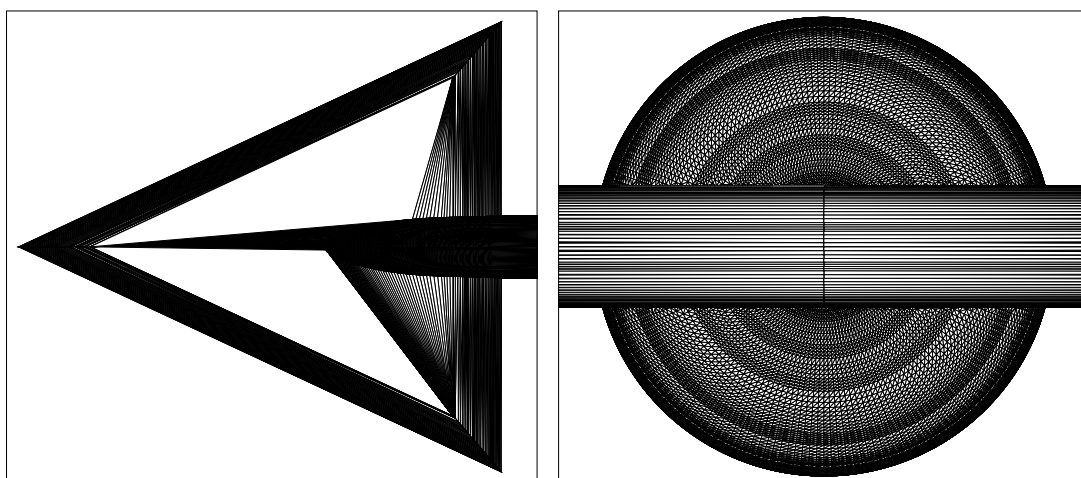
FIGURE 4.3: STL file of wing geometry with SLE. Left picture shows top view, right picture shows zoomed front view.

certain distance of the wall is limited, and a progressively increasing maximum number of refinement levels, leading to Grid 2, Grid 3, and Grid 4. Lastly, the grid is further refined in the region close to the apex and possibly in the region of the primary vortices, performed by means of custom criteria, such as magnitude of streamwise vorticity. Wall-adjacent cells of Grid 4, which will be primarily considered in the results chapters, have an estimated y^+ value of 120, and thus yield a wall model coupling position within the log layer. Grids used for simulations with the half-span model have been obtained by
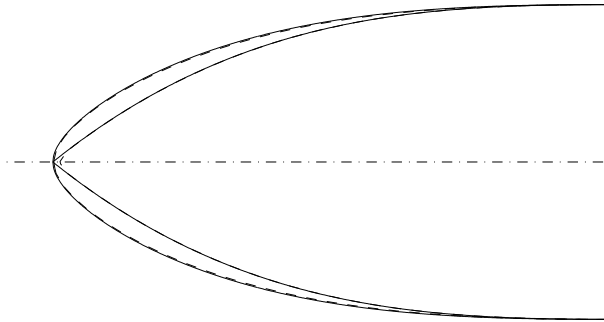
FIGURE 4.4: IB representation of leading edge (dashed line) compared with analytical description (solid line) for both SLE and MRLE, using Grid 4.
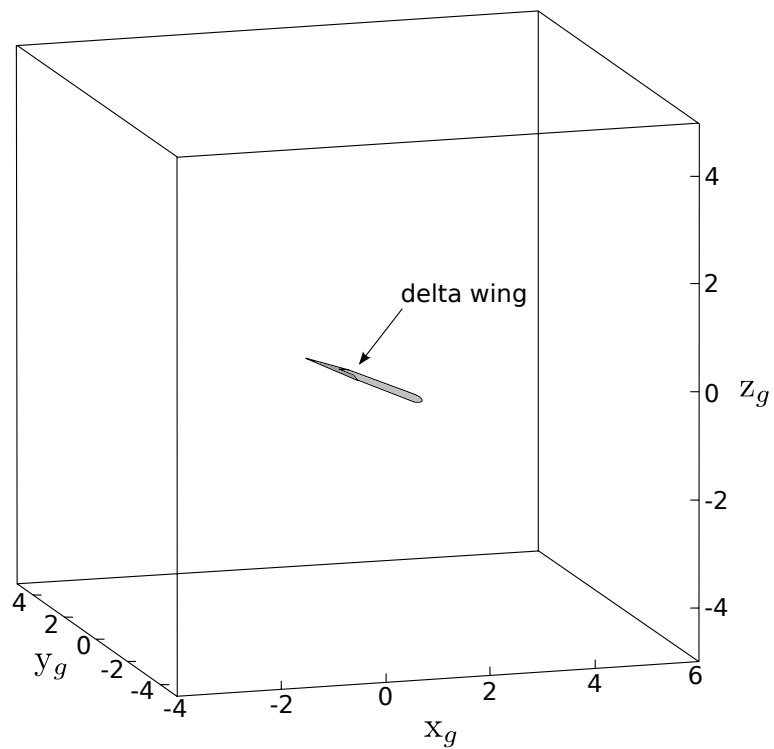
FIGURE 4.5: Sketch of computational domain and delta wing position therein ($c_r = 1$).

TABLE 4.1: Summary of applied computational grids for MRLE.

	MRLE	13°	18°	23°	28°
Grid 1	no. of cells	$1.2 \cdot 10^6$	$1.2 \cdot 10^6$	$1.2 \cdot 10^6$	
	no. of blocks	$9.0 \cdot 10^2$	$9.4 \cdot 10^2$	$9.6 \cdot 10^2$	
	min. cell size $[c_r]$	$9.8 \cdot 10^{-3}$	$9.8 \cdot 10^{-3}$	$9.8 \cdot 10^{-3}$	
Grid 2	no. of cells	$2.5 \cdot 10^6$	$2.4 \cdot 10^6$	$2.7 \cdot 10^6$	
	no. of blocks	$1.7 \cdot 10^3$	$1.7 \cdot 10^3$	$1.8 \cdot 10^3$	
	min. cell size $[c_r]$	$4.9 \cdot 10^{-3}$	$4.9 \cdot 10^{-3}$	$4.9 \cdot 10^{-3}$	
Grid 3	no. of cells	$6.9 \cdot 10^6$	$7.0 \cdot 10^6$	$7.4 \cdot 10^6$	$7.6 \cdot 10^6$
	no. of blocks	$4.0 \cdot 10^3$	$4.0 \cdot 10^3$	$4.3 \cdot 10^3$	$4.5 \cdot 10^3$
	min. cell size $[c_r]$	$2.4 \cdot 10^{-3}$	$2.4 \cdot 10^{-3}$	$2.4 \cdot 10^{-3}$	$2.4 \cdot 10^{-3}$
Grid 4	no. of cells	$2.5 \cdot 10^7$	$2.7 \cdot 10^7$	$2.8 \cdot 10^7$	
	no. of blocks	$1.2 \cdot 10^4$	$1.3 \cdot 10^4$	$1.3 \cdot 10^4$	
	min. cell size $[c_r]$	$1.2 \cdot 10^{-3}$	$1.2 \cdot 10^{-3}$	$1.2 \cdot 10^{-3}$	
Grid 4567	no. of cells			$7.4 \cdot 10^7$	
	no. of blocks			$3.3 \cdot 10^4$	
	min. cell size $[c_r]$			$1.5 \cdot 10^{-4}$	

taking the grid for the full-span model and splitting it into two parts. Tables 4.1 and 4.2 summarize the computational grids employed.

4.4   Boundary and initial conditions

At the inflow, a uniform velocity is prescribed. At the outflow, a static pressure of $p_{stat} = \frac{1}{\gamma \cdot Ma^2}$ is imposed. All other domain boundaries have a slip condition, see Fig. 4.7. Contrary to the wind tunnel experiments, where a non-zero turbulence level of $Tu \leq 0.08\%$ in the approaching flow was observed, the simulations are conducted with a turbulence level of $Tu = 0\%$, i.e. there are no random fluctuations at the inflow. However, one can assume that this deviation from the experimental conditions has overall only a minor effect. The wing walls are assumed to be adiabatic in the simulations.

The initial solution for all simulations is a uniform velocity distribution in streamwise direction. To satisfy the no-slip boundary condition at the geometry, the velocity profile close to the wall is chosen as

$$u(y_w) = (y_w - \frac{sin(2\pi y_w)}{2\pi}) \cdot U_\infty \, , \tag{4.1}$$

TABLE 4.2: Summary of applied computational grids for SLE.

	SLE	13°	18°	23°	28°
Grid 1	no. of cells	$1.2 \cdot 10^6$	$1.2 \cdot 10^6$	$1.2 \cdot 10^6$	
	no. of blocks	$9.0 \cdot 10^2$	$9.4 \cdot 10^2$	$9.6 \cdot 10^2$	
	min. cell size $[c_r]$	$9.8 \cdot 10^{-3}$	$9.8 \cdot 10^{-3}$	$9.8 \cdot 10^{-3}$	
Grid 2	no. of cells				
	no. of blocks				
	min. cell size $[c_r]$				
Grid 3	no. of cells	$6.7 \cdot 10^6$	$6.8 \cdot 10^6$	$7.3 \cdot 10^6$	$6.0 \cdot 10^6$
	no. of blocks	$3.9 \cdot 10^3$	$3.9 \cdot 10^3$	$4.3 \cdot 10^3$	$3.7 \cdot 10^3$
	min. cell size $[c_r]$	$2.4 \cdot 10^{-3}$	$2.4 \cdot 10^{-3}$	$2.4 \cdot 10^{-3}$	$2.4 \cdot 10^{-3}$
Grid 4	no. of cells	$2.4 \cdot 10^7$	$2.6 \cdot 10^7$	$2.2 \cdot 10^7$	
	no. of blocks	$1.2 \cdot 10^4$	$1.2 \cdot 10^4$	$1.1 \cdot 10^4$	
	min. cell size $[c_r]$	$1.2 \cdot 10^{-3}$	$1.2 \cdot 10^{-3}$	$1.2 \cdot 10^{-3}$	
Grid 45	no. of cells			$1.5 \cdot 10^7$	
	no. of blocks			$7.5 \cdot 10^3$	
	min. cell size $[c_r]$			$6.1 \cdot 10^{-4}$	
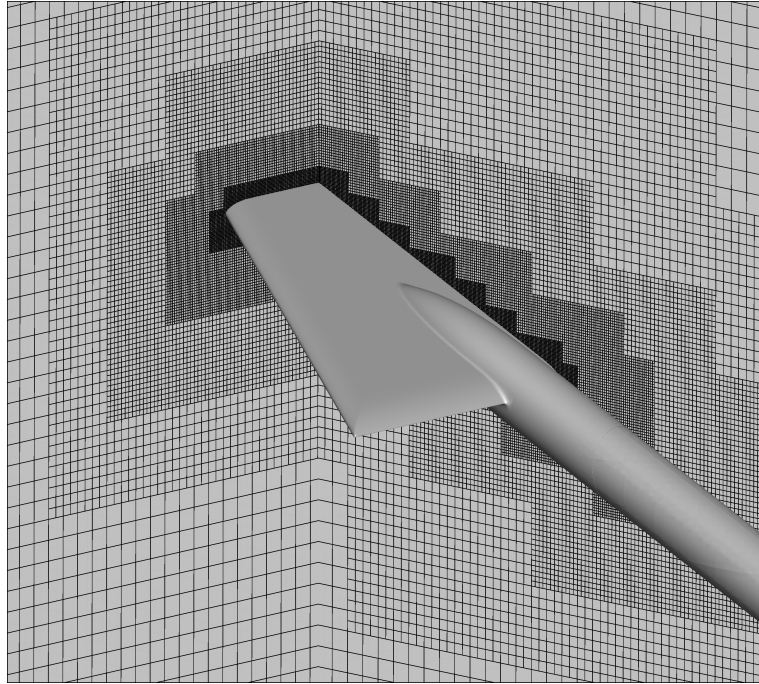
FIGURE 4.6: Exemplary picture of Grid 3, MRLE, angle of attack of 23°.
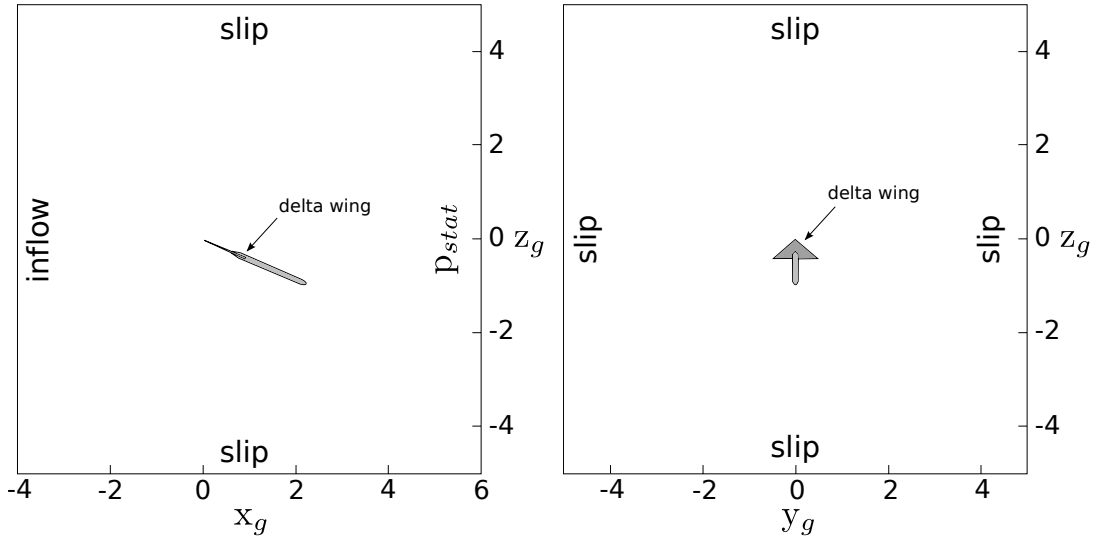
FIGURE 4.7: Boundary conditions of setup ($c_r = 1$).

where y_w is defined as $y_w = min(max(walldistance, 0), c_r)/c_r$, and U_∞ is the free stream velocity. For Grid 4 and upwards, i.e. Grid 45, ..., the initial condition is obtained by interpolating the results of a simulation with the next coarser grid onto the finer grid, e.g. the initial condition for Grid 4 was obtained by interpolating the results of Grid 3 on the finer Grid 4.

4.5   Compute system

The simulations have been carried out on the high performance compute system SuperMUC of the Leibniz-Rechenzentrum (LRZ) in Garching. SuperMUC consists of 18 thin node islands and one fat node island, which differ regarding several aspects, i.a. the number of nodes per island, the number of processors per node, and the number of cores per processor. The simulations have been primarily run on the fat node island as it provides more available memory per core when all cores per node are used. A detailed description of the compute system can be found in [121]. The simulations were carried out with up to 2080 cores, the maximum number of cores per standard job on the fat node island. However, considering the queuing time of the jobs, jobs with a lower number of cores, e.g. 1040, were overall faster.

Chapter 5

Results of investigations without flow control

This chapter presents results of the simulations without flow control, partly published in [122–124]. It focuses on the leading edge bluntness effects on primary vortex separation. To this end, medium radius round leading edge (MRLE) and sharp leading edge (SLE) at angles of attack of 13°, 18°, and 23° are considered in section one and two, respectively. The numerical results are compared with experimental measurements regarding main flow characteristics, velocity and velocity fluctuation intensity distributions, pressure and pressure fluctuation intensity distributions, and vortex breakdown position and frequency.

5.1 Medium Radius Leading Edge (MRLE) - angles of attack of $13°$, $18°$, and $23°$

As discussed in chapter 2, the MRLE configuration is computationally more challenging than the SLE configuration since the primary vortex separation is not geometrically fixed at the leading edge but slightly displaced from it. Considering the main flow characteristics, the numerical investigations show overall good agreement with the experimental results but discrepancies regarding the separation line, notably in the front part of the wing, where the leading edge crossflow bluntness is highest. Moreover, there is no secondary vortex for any of the three angles of attack. As a result, the velocity and

pressure distributions also deviate from the experimental measurements at the upstream cross sections. The agreement at the downstream cross sections is good, however. Vortex breakdown position and frequency are predicted well. A detailed discussion of the results is given in the following subsections.

5.1.1   Main flow characteristics

The main flow characteristics are predicted correctly for all angles of attack considered, apart from the secondary vortex, which is not present in any of the simulations. For $\alpha = 13°$, one observes a partly developed leading edge vortex, an apex vortex, and a counter rotating trailing edge vortex, see left column of Figure 5.1. For $\alpha = 18°$, one observes a fully developed leading edge vortex, an apex vortex, and a counter rotating trailing edge vortex, see center column of Fig. 5.1. For $\alpha = 23°$, one observes a fully developed leading edge vortex with vortex breakdown above the wing, and a counter rotating trailing edge vortex, see right column of Fig. 5.1. A secondary vortex has not been observed for any of the three angles of attack. For the configurations considered, the secondary vortex is expected to be small [88], which is corroborated by the experimental measurements, where the secondary vortex is only observable on the oil flow pictures but not in the velocity and pressure measurements. In this study, the grid resolution on the upper wing surface in conjunction with the TBLE wall model is insufficient to represent this small-scale flow feature, which confirms observations made in [125] and [110]. The vortex system leads to the characteristic pressure coefficient distribution on the upper surface of the wing with a suction peak below the axis of the primary vortex, see bottom row of Fig. 5.1. The main flow features depicted in Fig. 5.1 are predicted correctly regardless of the use of the wall model, indicating that the wall model does not have a major impact for this type of flow, an observation already made in a previous study [74].

A comparison of streamlines close to the wing surface with experimental oil flow visualizations, shown in Fig. 5.2, indicates that the primary vortex separation line is predicted further away from the leading edge in the front part of the wing for all three angles of attack.

For $\alpha = 13°$, the partly developed primary vortex leads to a primary vortex separation line originating at approximately one third chord length close to the leading edge. Given that the separation line is very close to the leading edge, it is hardly discernible in the
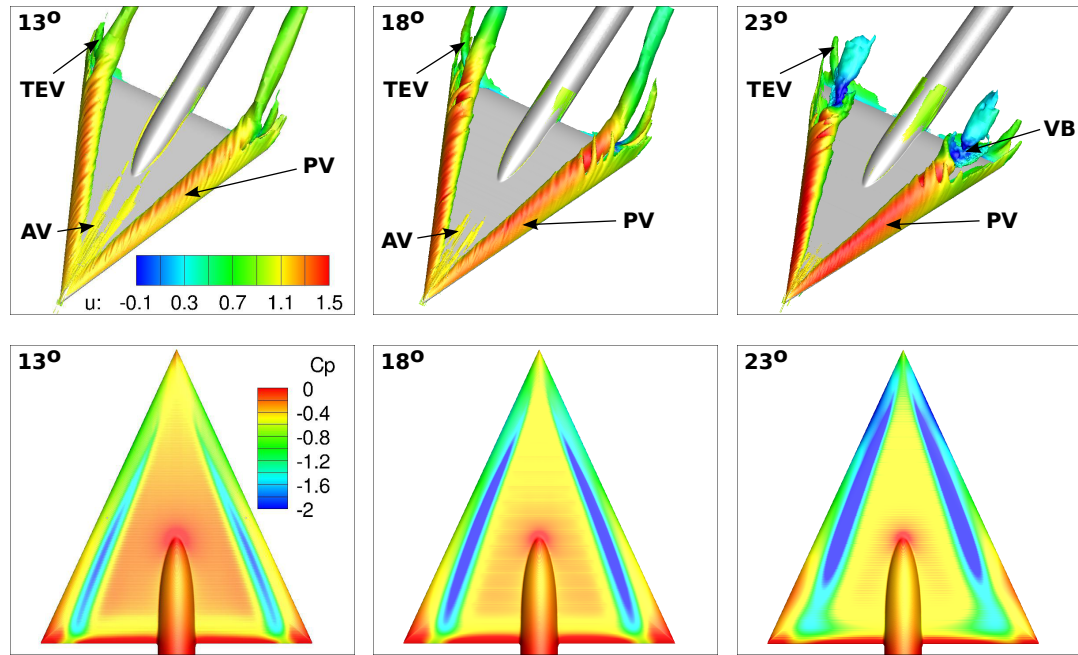
FIGURE 5.1: MRLE: Main flow characteristics at angles of attack of 13° (left), 18° (center), and 23° (right), obtained with Grid 4. AV - apex vortex, PV - primary vortex, TEV - trailing edge vortex, VB - vortex breakdown. Top row shows isosurfaces of streamwise vorticity ($\omega_x = \pm20$) colored by streamwise velocity. Bottom row shows pressure coefficient distribution on upper wing surface.

experimental oil flow visualization. In the simulation, it is clearly observable but not as close to the leading edge. The primary vortex attachment line observed in the simulation lies further inboard in the front part and approximately at the same position close to the trailing edge. The secondary vortex separation and attachment lines are not observed in the simulation.

For $\alpha = 18°$, the fully developed leading edge vortex leads to a primary vortex separation line originating close to the apex. Again, as for $\alpha = 13°$, the primary vortex separation line lies not as close to the leading edge as in the experiment. In comparison with $\alpha = 13°$, the primary vortex attachment line is located further inboard in both experiment and simulation. Comparing simulation with experiment, one again observes that the attachment line lies further inboard in the front part and approximately at the same position at the trailing edge. For $\alpha = 18°$, the secondary vortex separation and attachment lines are again only visible in the experiment.

For $\alpha = 23°$, the fully developed leading edge vortex leads to a primary vortex separation line originating close to the apex, which, as for the other two angles of attack, again lies closer to the leading edge in the experiment. The primary vortex attachment
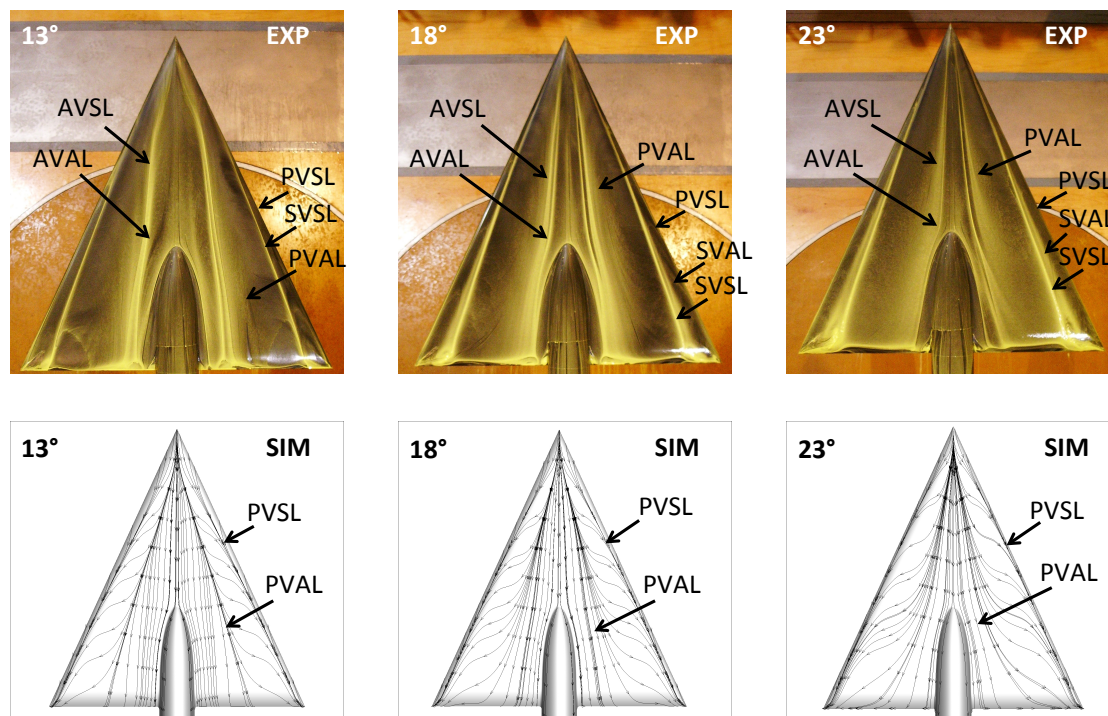
FIGURE 5.2: MRLE: Comparison of vortex footprint on upper surface: experimental oil flow visualization (top row) [38, 40, 41] and surface streamlines from simulations with Grid 1 and wall model (bottom row). AVSL - apex vortex separation line, AVAL - apex vortex attachment line, PVSL - primary vortex separation line, PVAL - primary vortex attachment line, SVSL - secondary vortex separation line, SVAL - secondary vortex attachment line.

line lies close to the center of the wing in both experiment and simulation. Again, secondary vortex separation and attachment line are only observed in the experiment. As mentioned at the beginning of this paragraph, the primary vortex separation line lies farther from the leading edge for all three angles of attack considered, notably in the front part. Using the refined Grid 4567, which still does not resolve the wall region, the position of the separation line moves closer to the leading edge, which is in better agreement with the experiment, suggesting that the TBLE wall model employed in this study is not able to accurately predict the separation line for the considered complex flow around a curved surface. Also, simulations with a simple no-slip condition yield a very similar streamline topology on Grid 4. One can thus conclude that the wall model has only a minor influence on the flow topology.

5.1.2 Velocity distribution and velocity fluctuation intensities

A comparison of the velocity distribution at different cross sections, shown in Figs. 5.3 & 5.4, 5.5 & 5.6, and 5.7 & 5.8 for $\alpha = 13°$, $\alpha = 18°$, and $\alpha = 23°$, respectively, shows overall good agreement and is in line with the previously observed discrepancy regarding the separation line position in the front part of the wing.

For $\alpha = 13°$, at cross section $x/c_r = 0.2$, the velocity distribution obtained with Grid 4 is in reasonable agreement with the experimental data with slight differences in the region close to the leading edge. At $x/c_r = 0.4$, the experimental velocity distribution shows a higher maximum streamwise velocity and the vortex core lies closer to the leading edge than in the simulation. At $x/c_r = 0.6$ and $x/c_r = 0.8$, the velocity distribution obtained in the simulation is in good agreement with the experimental data, with a minor discrepancy regarding the maximum streamwise velocity which is predicted higher by the simulation. This observation can still be made at the most downstream location, $x/c_r = 0.95$, where the vortex core lies further inboard in the experiment.

For $\alpha = 18°$, at cross section $x/c_r = 0.2$, the velocity distribution obtained by the simulation is in rather good agreement with the experimental data, showing again, as for $\alpha = 13°$, slight differences in the region close the leading edge. The experimental data show a region of negative or low streamwise velocity away from the leading edge, which is counterintuitive and might be a measurement inaccuracy. At $x/c_r = 0.4$, the predicted velocity distribution is overall in good agreement with the experimental data with a minor discrepancy regarding the vortex core which lies further inboard. The agreement between simulation and experiment is very good at $x/c_r = 0.6$. At $x/c_r = 0.8$, the overall shape is in good agreement but the vortex core is predicted closer to the leading edge by the simulation. At the most downstream location, $x/c_r = 0.95$, the vortex core is again predicted closer to the leading edge and a region of high streamwise velocity in the vortex core is observed, whereas the experiment shows a small region of negative streamwise velocity indicating vortex breakdown. Vortex breakdown is sensitive to minor disturbances, e.g. slight changes in the surrounding conditions. Therefore, for $\alpha = 18°$, vortex breakdown above the wing sometimes occurs and sometimes not. Note, for instance, that vortex breakdown was observed in the experiments for the MRLE but not for the SLE, even though vortex breakdown generally occurs earlier for the SLE. In view of the fixed boundary conditions with no disturbances in the simulations, it is thus not surprising that vortex breakdown is not observed for $\alpha = 18°$.

FIGURE 5.3: MRLE, $\alpha = 13°$: Velocity distribution at cross sections $x/c_r = 0.2, 0.4,$ and 0.6 (from left to right). Top row shows experimental measurements [38, 40, 41], bottom row shows results of simulation with Grid 4 and simple no-slip condition.

For $\alpha = 23°$, at cross section $x/c_r = 0.2$, the velocity distribution obtained with Grid 4567 is in good agreement with the experimental data. For Grid 4, the position of the vortex core is further inboard and further away from the wall. At $x/c_r = 0.4$ and $x/c_r = 0.6$, the velocity distributions are in good agreement with the experimental data for both Grid 4 and Grid 4567. At $x/c_r = 0.8$, the simulation with Grid 4 predicts a higher streamwise velocity in the vortex core and for $x/c_r = 0.95$ a larger region of negative streamwise velocity. Vortex breakdown occurred at approximately the same position as in the experiment, namely $x/c_r \approx 0.89$ (vs. $x/c_r \approx 0.85$ in the experiment). For Grid 4567, the simulations predict larger regions of higher negative velocities in streamwise direction at $x/c_r = 0.8$ and $x/c_r = 0.95$, which stems from the slightly earlier vortex breakdown, observed at $x/c_r \approx 0.77$ for this simulation.

Distributions of streamwise velocity fluctuation intensities at different cross sections for $\alpha = 13°$, $\alpha = 18°$, and $\alpha = 23°$ are shown in Figs. 5.9 - 5.14. Compared with the experimental measurements conducted at $Re = 1 \cdot 10^6$ and $Ma = 0.07$ [38, 40, 41], the simulations predict lower levels of velocity fluctuation intensities for all three angles of attack, see Figs. 5.9 - 5.11. However, the results for $\alpha = 23°$ are in good agreement with experimental results reported in [87]: Upstream of the vortex breakdown

FIGURE 5.4: MRLE, $\alpha = 13°$: Velocity distribution at cross sections $x/c_r = 0.8$ and 0.95 (from left to right). Top row shows experimental measurements [38, 40, 41], bottom row shows results of simulation with Grid 4 and simple no-slip condition.

FIGURE 5.5: MRLE, $\alpha = 18°$: Velocity distribution at cross sections $x/c_r = 0.2, 0.4$, and 0.6 (from left to right). Top row shows experimental measurements [38, 40, 41], bottom row shows results of simulation with Grid 4 and simple no-slip condition.

FIGURE 5.6: MRLE, $\alpha = 18°$: Velocity distribution at cross sections $x/c_r = 0.8$ and 0.95 (from left to right). Top row shows experimental measurements [38, 40, 41], bottom row shows results of simulation with Grid 4 and simple no-slip condition.

location, i.e. $x/c_r = 0.2$, $x/c_r = 0.4$, and $x/c_r = 0.6$, $u_{RMS} \approx 20\%$ in the region of the primary vortex and $u_{RMS} \approx 0\%$ outside of the vortex. At $x/c_r = 0.8$ and $x/c_r = 0.85$, i.e. at or close to the vortex breakdown location, the velocity fluctuation intensity significantly increases and reaches values up to $u_{RMS} \approx 50\%$ in the vortex core. This region of maximum turbulence intensity rapidly expands and annular regions of maximum turbulence intensity $u_{RMS} \approx 30\% - 40\%$ are formed downstream of the vortex breakdown location, see Fig. 5.12. Lateral velocity fluctuations, v_{RMS}, and vertical velocity fluctuations, w_{RMS}, also show qualitatively good agreement, see Figs. 5.13 and 5.14, but are predicted slightly higher than observed in the experiments [87].

5.1.3   Surface pressure distribution and surface pressure fluctuation intensities

A quantitative comparison of the pressure coefficient (C_p) distribution at different cross sections of the wing, shown in Figs. 5.15 - 5.17, shows reasonable to good agreement in the rear part of the wing and discrepancies in the front part, which is in accordance with the previous observations, notably the deviating separation line position in the front part.
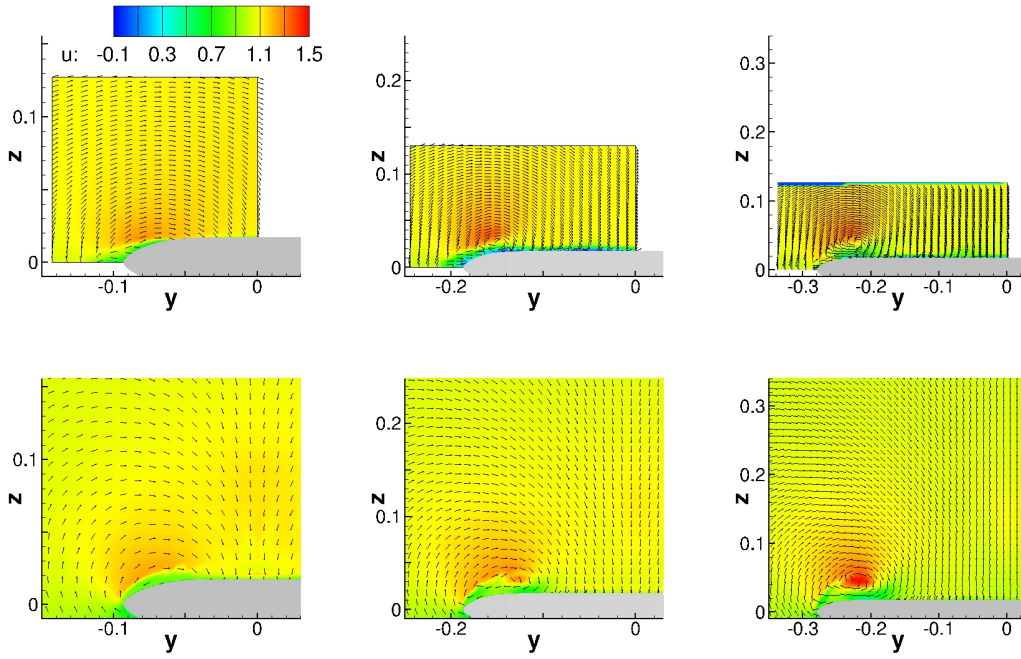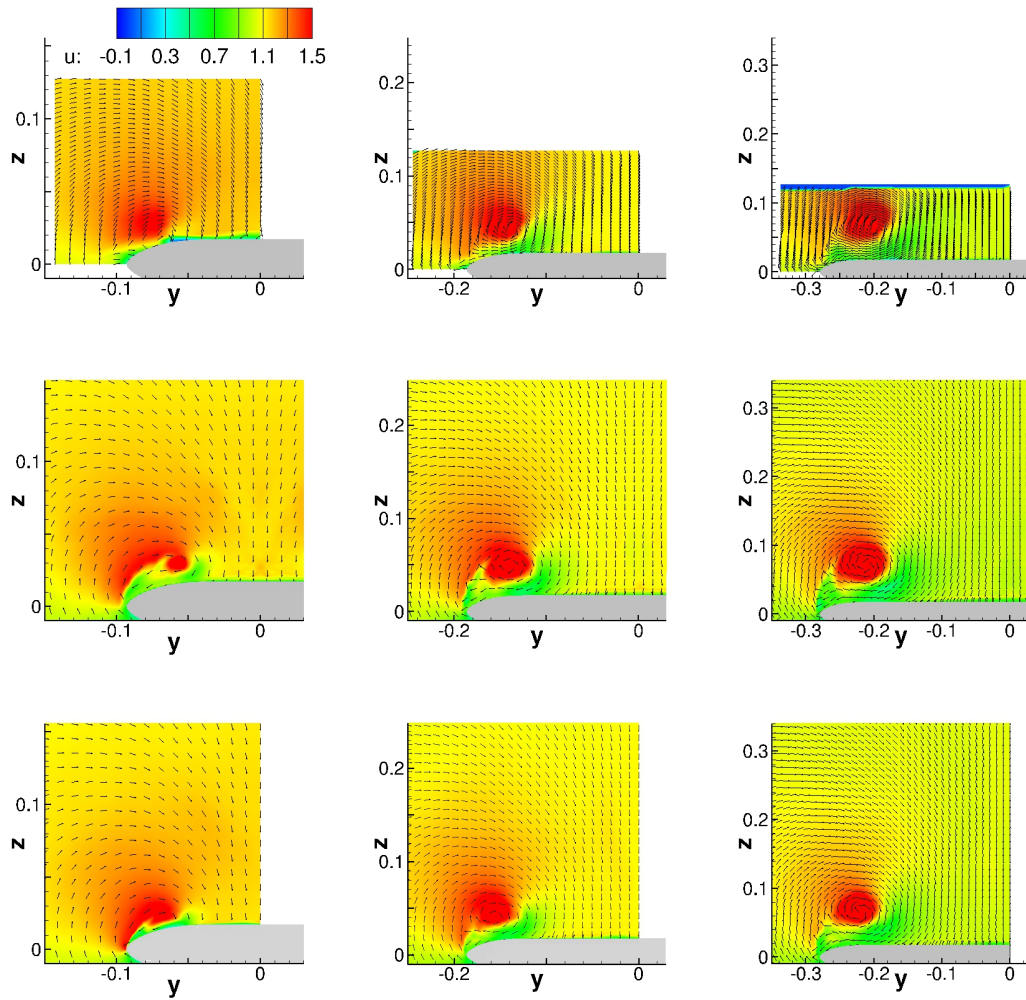
FIGURE 5.7: MRLE, $\alpha = 23°$: Velocity distribution at cross sections $x/c_r = 0.2, 0.4$, and 0.6 (from left to right). Top row shows experimental measurements [38, 40, 41], center row shows results of simulation with Grid 4 and TBLE wall model, bottom row shows results of simulation with Grid 4567 and simple no-slip condition.

For $\alpha = 13°$, the simulations fail to predict the suction peak close to the leading edge at $x/c_r = 0.2$ and $x/c_r = 0.4$. For the latter cross section, a suction peak of lower magnitude appears but is located further inboard. At $x/c_r = 0.6$, the magnitude of the suction peak is predicted equally high as in the experiment but it is still located further inboard. At $x/c_r = 0.8$, the location of the suction peak is in good agreement with the experimental data but its magnitude is predicted higher. For the most downstream cross section at $x/c_r = 0.95$, the suction peak is predicted higher and closer to the leading edge. For $\alpha = 13°$, the TBLE wall model had almost no effect on the C_p distribution at cross sections $x/c_r = 0.2$, $x/c_r = 0.4$ and $x/c_r = 0.6$. At the two most downstream cross sections, the results obtained with the TBLE wall model are slightly closer to the experimental data than the results obtained with a simple no-slip condition.
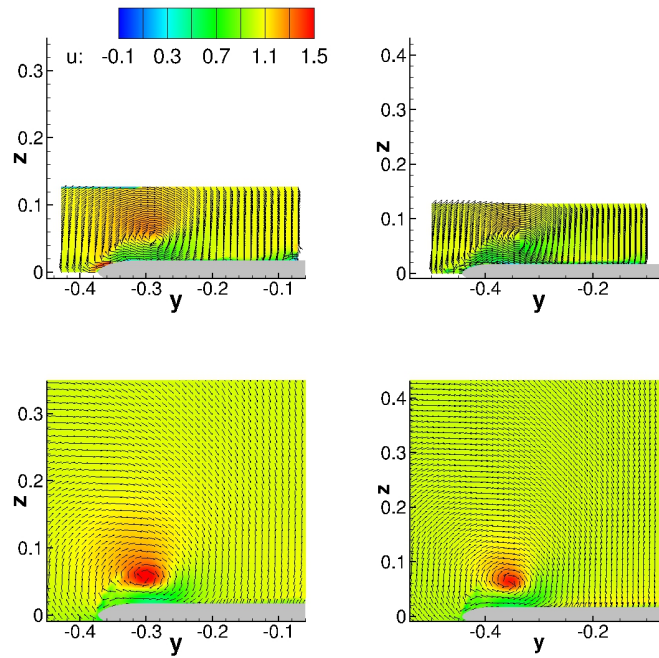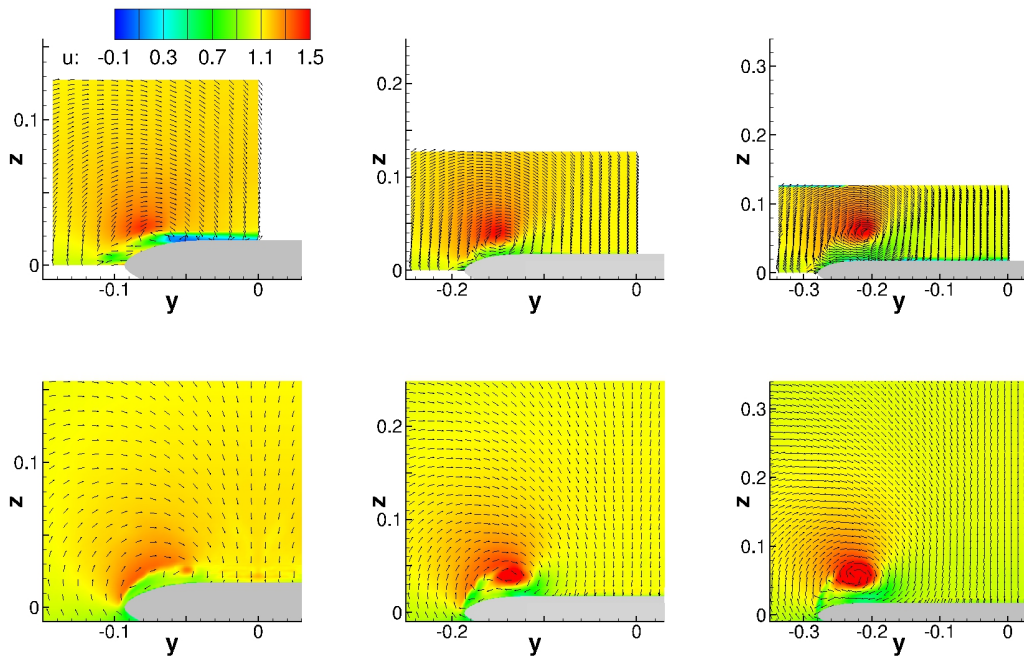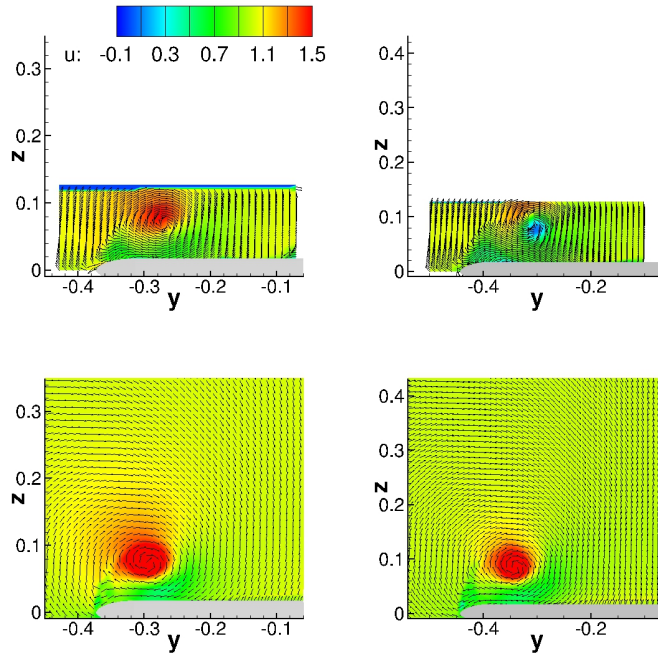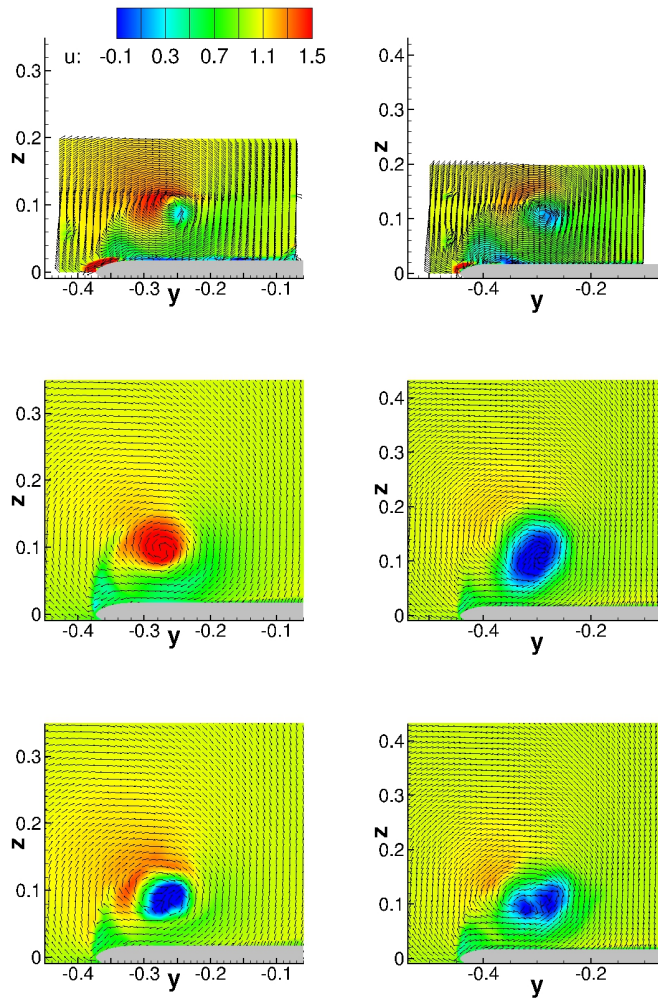
FIGURE 5.8: MRLE, $\alpha = 23°$: Velocity distribution at cross sections $x/c_r = 0.8$ and 0.95 (from left to right). Top row shows experimental measurements [38, 40, 41], center row shows results of simulation with Grid 4 and TBLE wall model, bottom row shows results of simulation with Grid 4567 and simple no-slip condition.

For $\alpha = 18°$, the simulations again fail to predict the suction peak close to the leading edge at $x/c_r = 0.2$. At $x/c_r = 0.4$, the magnitude of the suction peak is predicted as measured in the experiment but its location is further inboard. At $x/c_r = 0.6$ and $x/c_r = 0.8$, the location of the suction peak is in good agreement with the experiment but its magnitude is predicted higher. At the most downstream cross section, the suction peak is predicted higher and closer to the leading edge. For $\alpha = 18°$, the TBLE wall model again had only little effect on the C_p distribution at cross sections $x/c_r = 0.2$ and $x/c_r = 0.4$. At the following cross sections, it shows a slight improvement compared to the results obtained with the simple no-slip condition.

For $\alpha = 23°$, the simulations with Grid 4 show a suction peak which is located further inboard and significantly lower in magnitude at cross section $x/c_r = 0.2$. Using Grid
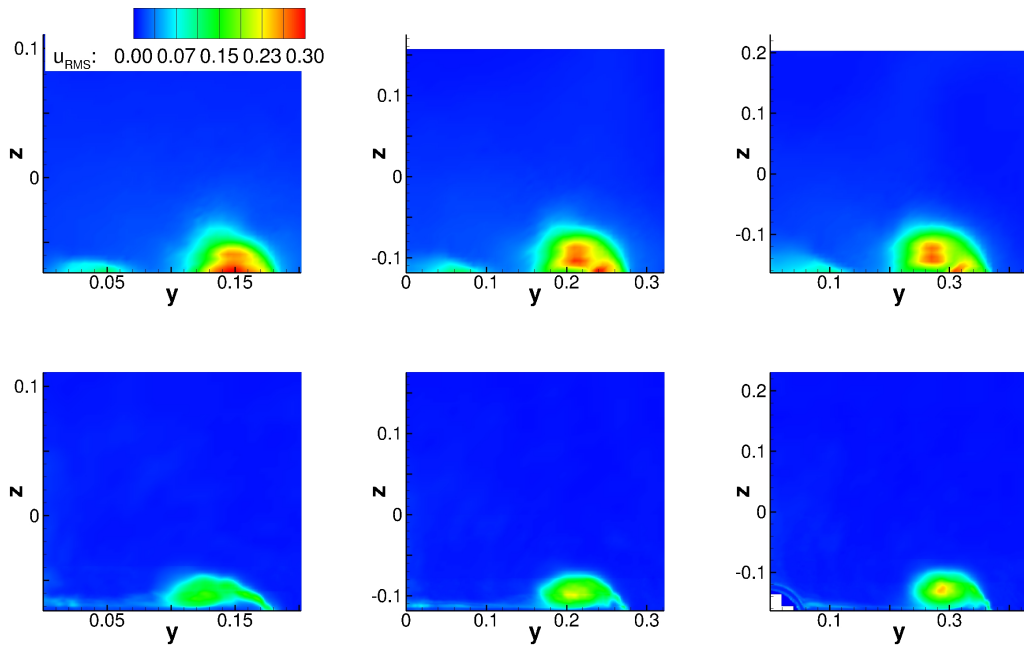
FIGURE 5.9: MRLE, $\alpha = 13°$: Velocity fluctuation intensities u_{RMS} at cross sections $x/c_r = 0.4, 0.6,$ and 0.8 (from left to right). Top row shows experimental data for $Re = 1 \cdot 10^6$ and $Ma = 0.07$ [38, 40, 41], bottom row shows results of simulation with Grid 4 and TBLE wall model.
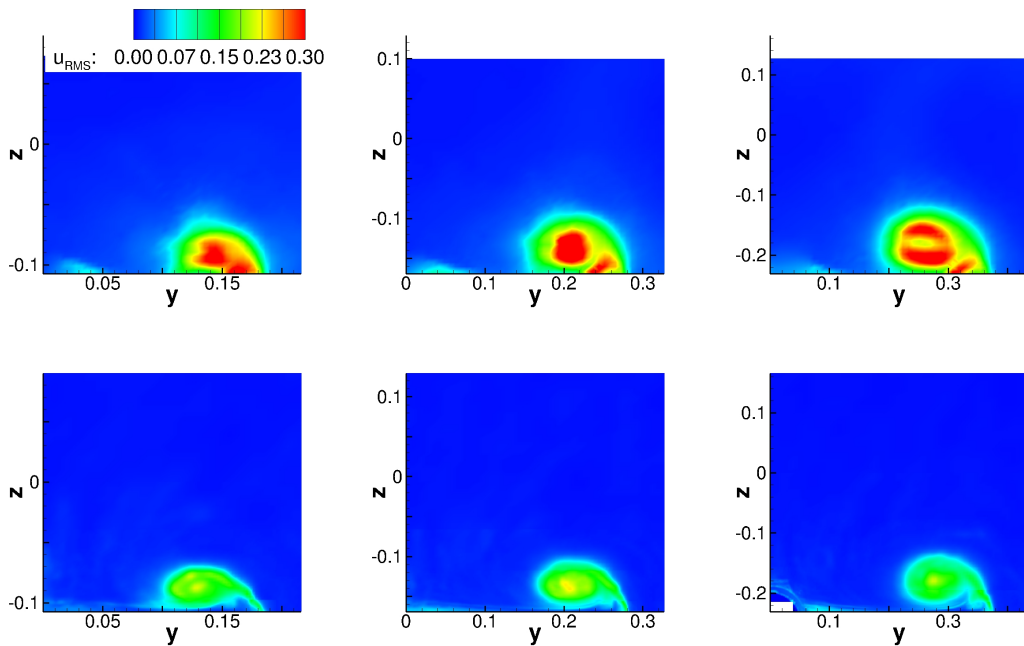
FIGURE 5.10: MRLE, $\alpha = 18°$: Velocity fluctuation intensities u_{RMS} at cross sections $x/c_r = 0.4, 0.6,$ and 0.8 (from left to right). Top row shows experimental data for $Re = 1 \cdot 10^6$ and $Ma = 0.07$ [38, 40, 41], bottom row shows results of simulation with Grid 4 and TBLE wall model.
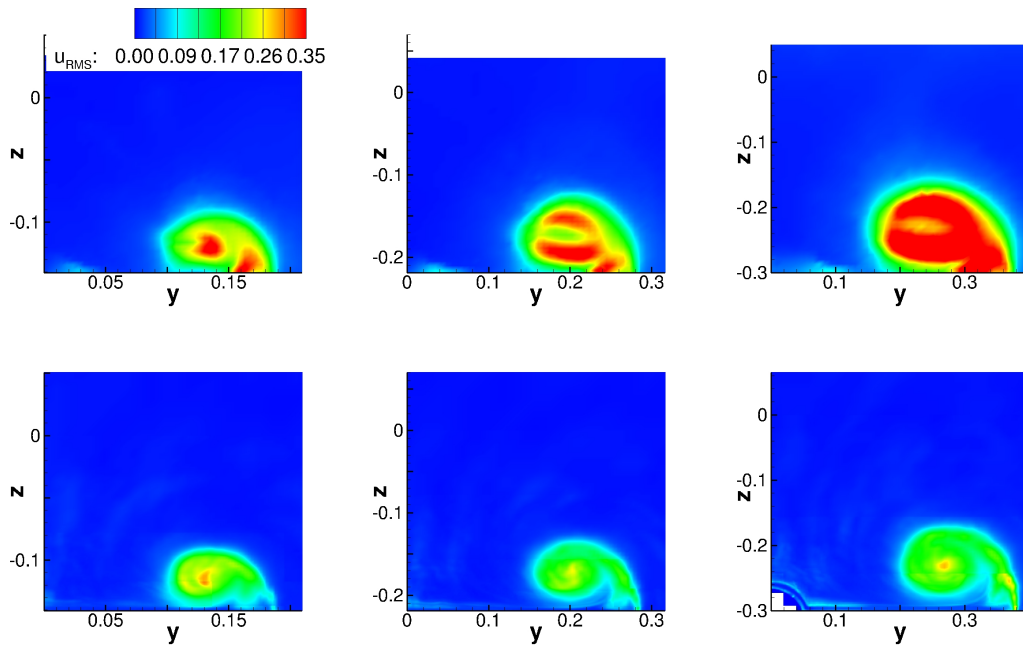
FIGURE 5.11: MRLE, $\alpha = 23°$: Velocity fluctuation intensities u_{RMS} at cross sections $x/c_r = 0.4, 0.6,$ and 0.8 (from left to right). Top row shows experimental data for $Re = 1 \cdot 10^6$ and $Ma = 0.07$ [38, 40, 41], bottom row shows results of simulation with Grid 4 and TBLE wall model.
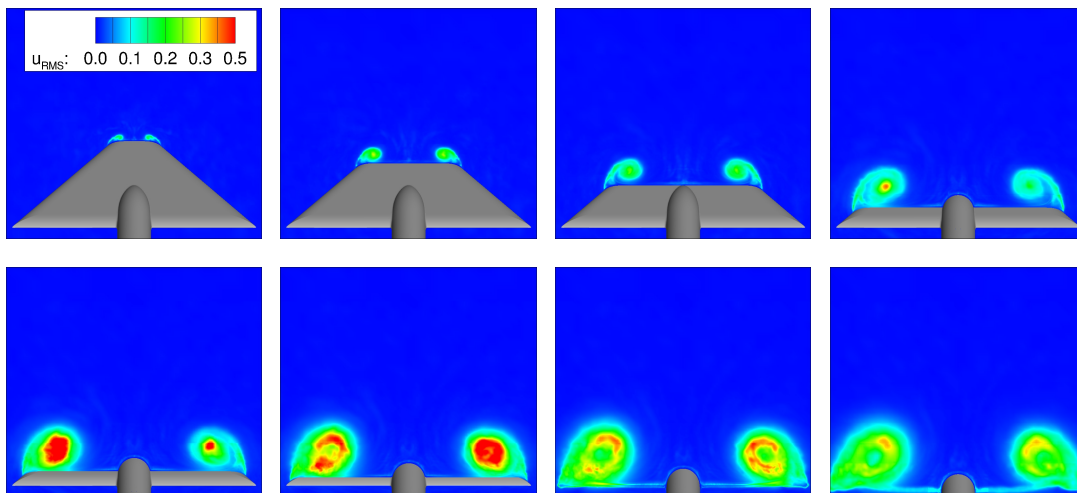
FIGURE 5.12: MRLE, $\alpha = 23°$: Velocity fluctuation intensities u_{RMS} at cross sections $x_g/c_r = 0.2, 0.4, 0.6,$ and 0.8 (top row from left to right) and $x_g/c_r = 0.85, 0.9, 0.95,$ and 1.0 (bottom row from left to right). Simulation with Grid 4 and TBLE wall model.
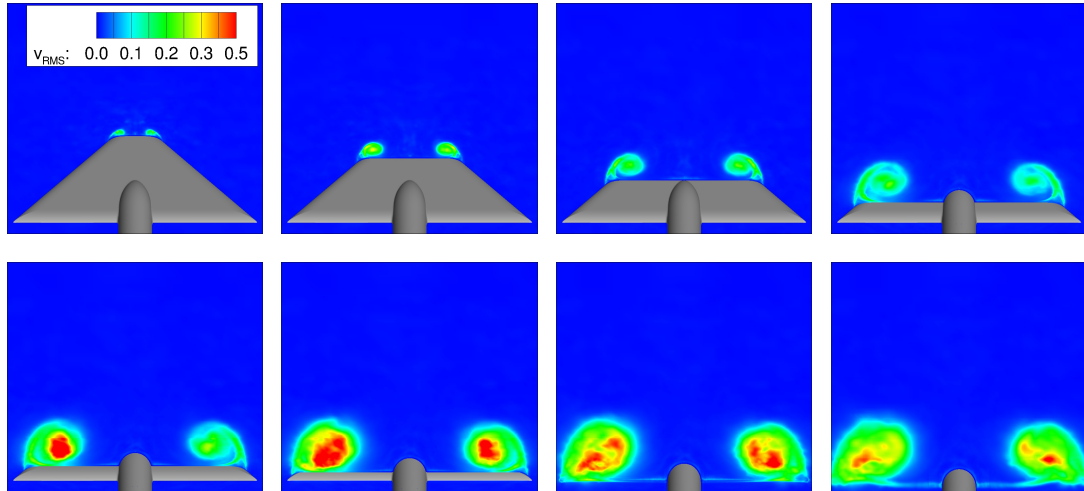
FIGURE 5.13: MRLE, $\alpha = 23°$: Velocity fluctuation intensities v_{RMS} at cross sections $x_g/c_r = 0.2, 0.4, 0.6$, and 0.8 (top row from left to right) and $x_g/c_r = 0.85, 0.9, 0.95$, and 1.0 (bottom row from left to right). Simulation with Grid 4 and TBLE wall model.
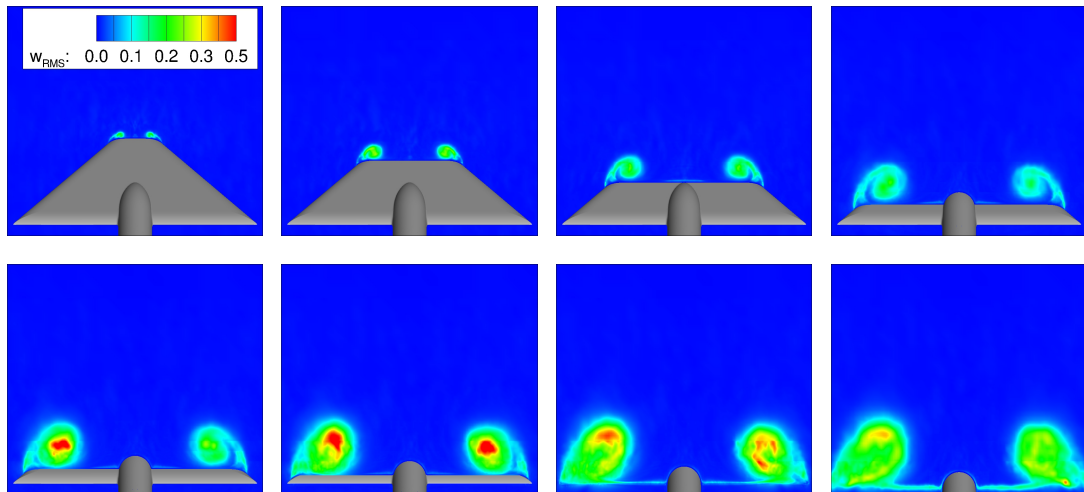
FIGURE 5.14: MRLE, $\alpha = 23°$: Velocity fluctuation intensities w_{RMS} at cross sections $x_g/c_r = 0.2, 0.4, 0.6$, and 0.8 (top row from left to right) and $x_g/c_r = 0.85, 0.9, 0.95$, and 1.0 (bottom row from left to right). Simulation with Grid 4 and TBLE wall model.

4567, which is refined in the region close to the apex, the suction peak is predicted significantly better but is still located further inboard and lower in magnitude. Studies with successively refined grids in the apex region showed that the prediction of both magnitude and location of the suction peak at $x/c_r = 0.2$ converges to the experimental data, indicating that a fully resolved apex region, which could not be realized in this work due to limited computational resources, might remedy the discrepancy at this cross section. At $x/c_r = 0.4$, the C_p distribution obtained with Grid 4 shows a suction peak of equal magnitude as in the experiment but located slightly inboard of the experiment.

FIGURE 5.15: MRLE, $\alpha = 13°$: Surface pressure distribution C_p at cross sections $x/c_r = 0.2, 0.4, 0.6, 0.8$ and 0.95 (from left to right and from top to bottom). Grid 4 with TBLE wall model - blue; Grid 4 with simple no-slip condition - red; Experiments [38, 40, 41] - black. η denotes normalized local half span width.

For Grid 4567, the suction peak's location is in good agreement with the experiment but its magnitude is predicted slightly higher. At $x/c_r = 0.6$ and $x/c_r = 0.8$, the simulations with Grid 4 correctly predict the suction peak location but a higher magnitude. For Grid 4567, the agreement with the experimental data is very good. At the most downstream cross section $x/c_r = 0.95$, the suction peak is predicted slightly outboard and slightly higher for Grid 4 and Grid 4567 with overall better agreement for Grid 4567. For $\alpha = 23°$, the TBLE wall model slightly improved the predicted C_p distribution at all cross sections, apart from $x/c_r = 0.2$. However, the improvement due to the TBLE wall model is significantly less than the improvement obtained by refining the grid, corroborating again that the effect of the wall model is marginal.

A quantitative comparison of the pressure coefficient fluctuations ($C_{p,RMS}$), see Figs. 5.18 - 5.20 for simulations with Grid 4 and TBLE wall model, shows reasonable agreement. For $\alpha = 13°$, the overall shape of the $C_{p,RMS}$ distribution at $x/c_r = 0.4$ and $x/c_r = 0.6$ is in good agreement with the experimental data, showing two peaks. However, their location is further inboard and the magnitude is predicted lower which is in agreement with the computed C_p distribution for this configuration. At $x/c_r = 0.8$, overall shape and location of the peaks are in good agreement with the experimental data, however
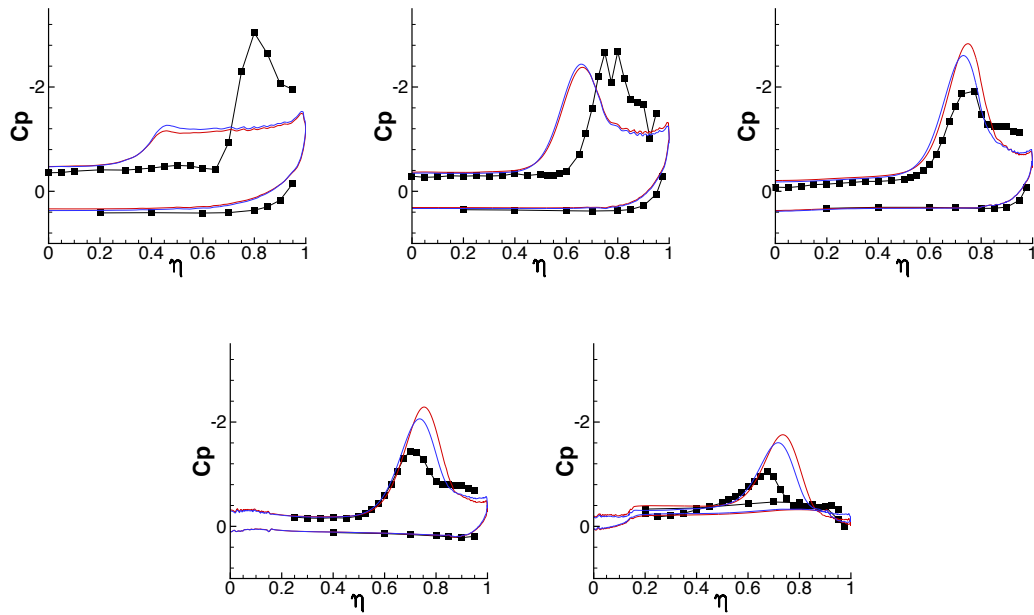
FIGURE 5.16: MRLE, $\alpha = 18°$: Surface pressure distribution C_p at cross sections $x/c_r = 0.2, 0.4, 0.6, 0.8$ and 0.95 (from left to right and from top to bottom). Grid 4 with TBLE wall model - blue; Grid 4 with simple no-slip condition - red; Experiments [38, 40, 41] - black. η denotes normalized local half span width.
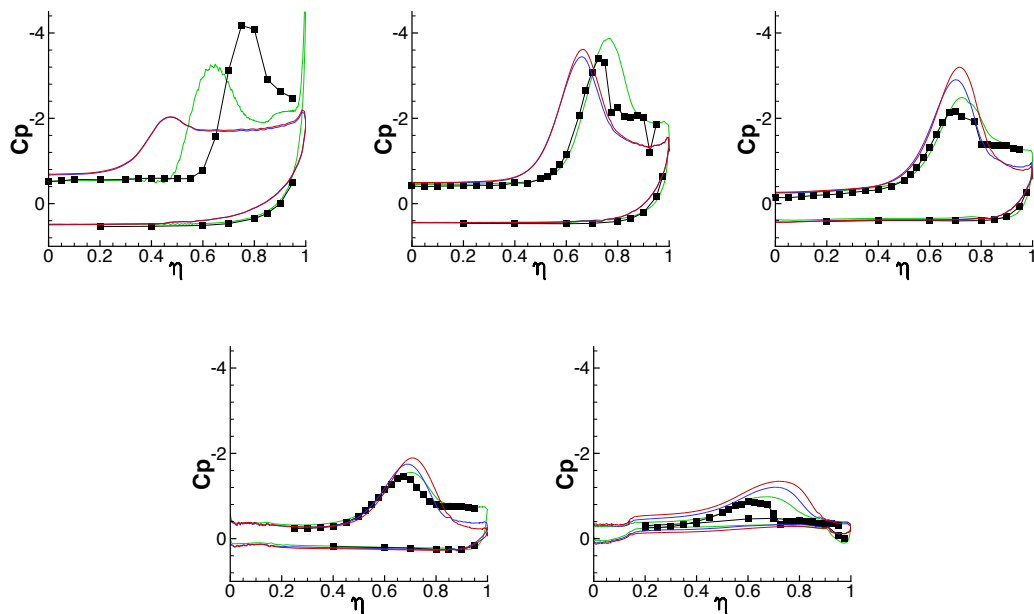
FIGURE 5.17: MRLE, $\alpha = 23°$: Surface pressure distribution C_p at cross sections $x/c_r = 0.2, 0.4, 0.6, 0.8$ and 0.95 (from left to right and from top to bottom). Grid 4 with TBLE wall model - blue; Grid 4 with simple no-slip condition - red; Grid 4567 - Grid 4567 with simple no-slip condition; Experiments [38, 40, 41] - black. η denotes normalized local half span width.

the fluctuations are predicted slightly higher. At $x/c_r = 0.95$, the magnitude of the fluctuations is predicted as measured in the experiments but the peak is slightly outboard. For $\alpha = 18°$, the $C_{p,RMS}$ distribution at $x/c_r = 0.4$ shows two peaks of approximately the same magnitude as in the experiment, but located slightly inboard, which is in line with the predicted C_p distribution. At the other three cross sections, the $C_{p,RMS}$ distributions show very poor agreement with the experimental measurements. In particular, inboard of the primary vortex, the predicted level of pressure fluctuations is significantly higher, which is surprising given that these regions are predicted fairly well for the other two angles of attack.

For $\alpha = 23°$, the computed $C_{p,RMS}$ distribution $x/c_r = 0.4$ shows two peaks, whereas only one peak was observed in the experiment. The magnitude is predicted slightly higher, the location is slightly inboard, which is in agreement with the computed C_p distribution. At $x/c_r = 0.6$, the simulation again shows two peaks whereas only one peak was observed in the experiment. The location of the main peak is predicted as measured in the experiment, but the magnitude is slightly higher. At $x/c_r = 0.8$, the overall shape is in good agreement with the experiment but the fluctuations are predicted higher. At $x/c_r = 0.95$, neither shape nor magnitude of the distribution are in agreement with the experimental data. However, the significantly increased fluctuation level predicted is in agreement with the increased turbulence level that one generally expects in the vortex breakdown region. The experimental data at $x/c_r = 0.95$, which show almost the same fluctuation level as for the other three cross sections, are thus surprising.

5.1.4   Vortex breakdown position and frequency

Vortex breakdown, indicated by zero or negative streamwise velocities in the vortex core, was observed at $x/c_r \approx 0.89$ for Grid 4 with TBLE wall model, and at $x/c_r \approx 0.77$ for Grid 4567. These results are in good agreement with the experimental result, $x/c_r \approx 0.85$ [38]. The vortex breakdown is of helical type, see Fig. 5.21, and the vortex axis's rotation is opposite to the primary vortex's rotation, as described in [13].

In order to determine the frequency of the vortex breakdown occurring in the simulation, a pressure signal has been extracted from a point in the vortex breakdown region ($x_g = 0.87$, $y_g = 0.23$, $z_g = -0.24$) and analyzed by a Fourier transform. As one can see
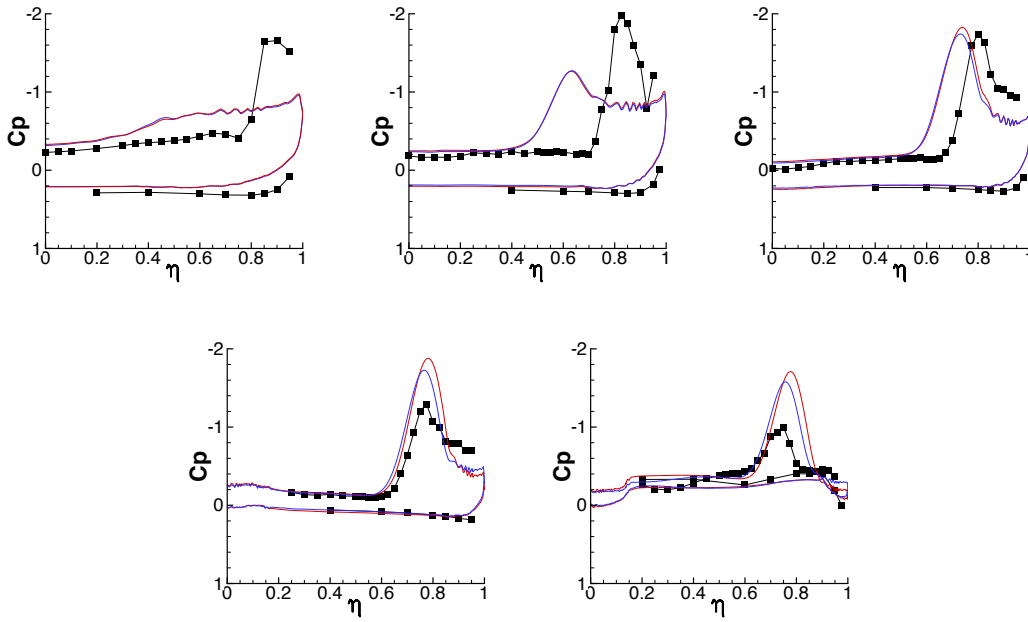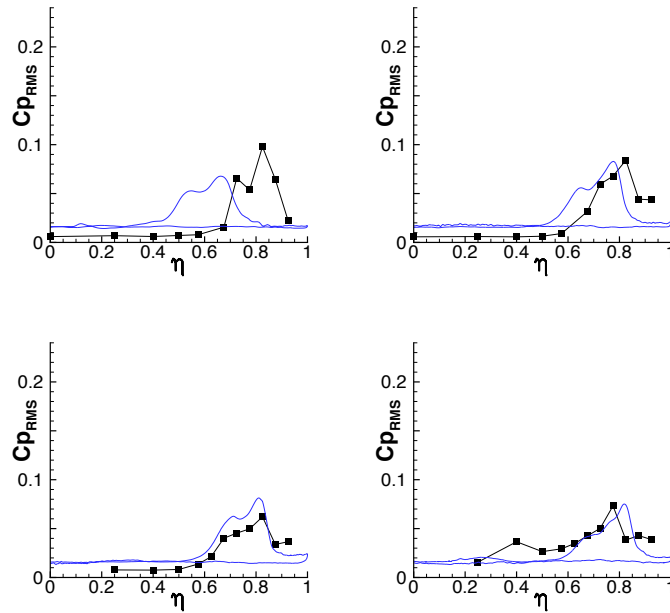
FIGURE 5.18: MRLE, $\alpha = 13°$: Surface pressure fluctuation intensities $C_{p,RMS}$ at cross sections $x/c_r = 0.4, 0.6, 0.8$ and 0.95 (from left to right and from top to bottom). Grid 4 with TBLE wall model - blue; Experiments [38, 40, 41] - black. η denotes normalized local half span width.
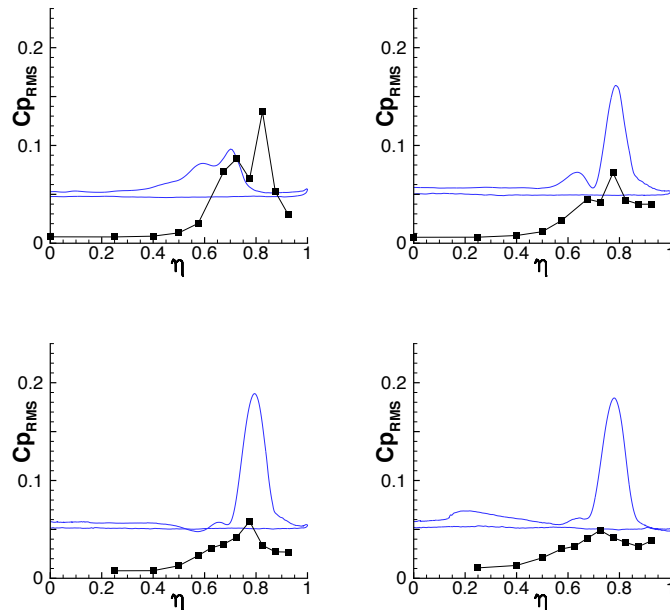
FIGURE 5.19: MRLE, $\alpha = 18°$: Surface pressure fluctuation intensities $C_{p,RMS}$ at cross sections $x/c_r = 0.4, 0.6, 0.8$ and 0.95 (from left to right and from top to bottom). Grid 4 with TBLE wall model - blue; Experiments [38, 40, 41] - black. η denotes normalized local half span width.
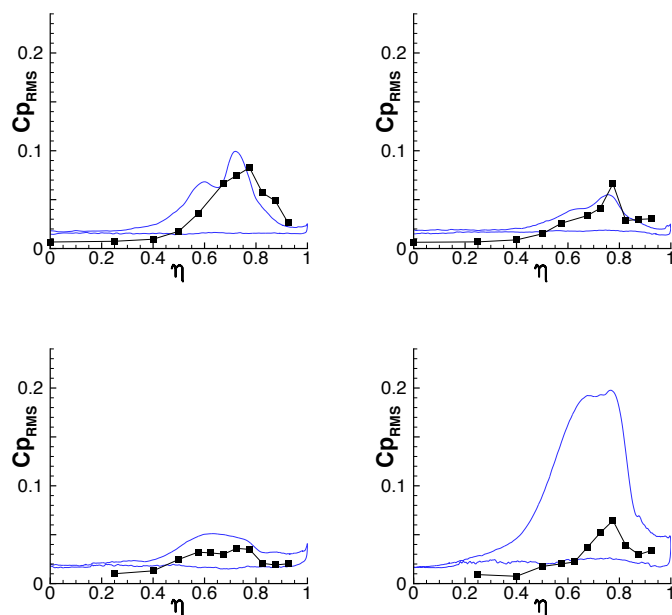
FIGURE 5.20: MRLE, $\alpha = 23°$: Surface pressure fluctuation intensities $C_{p,RMS}$ at cross sections $x/c_r = 0.4, 0.6, 0.8$ and 0.95 (from left to right and from top to bottom). Grid 4 with TBLE wall model - blue; Experiments [38, 40, 41] - black. η denotes normalized local half span width.
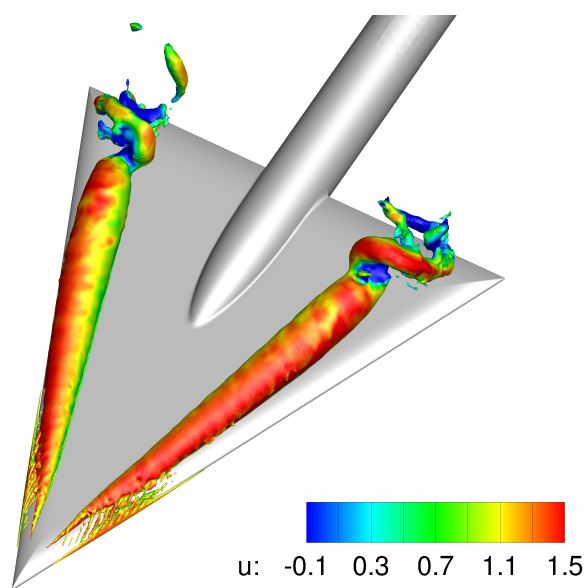
FIGURE 5.21: MRLE, $\alpha = 23°$: Helical form of vortex breakdown. Figure shows isosurface of pressure coefficient ($C_p = -2$) colored by streamwise velocity.
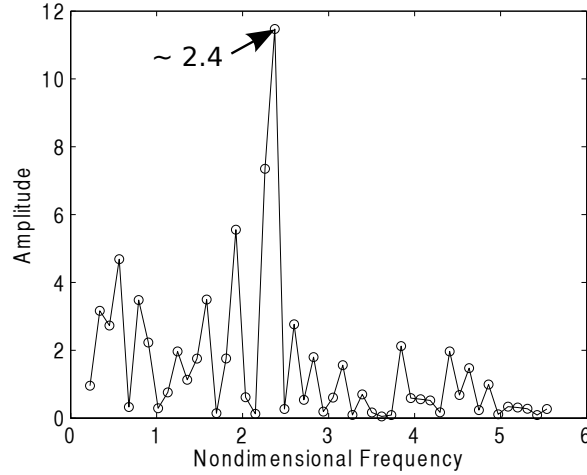
FIGURE 5.22: MRLE, $\alpha = 23°$: Frequency analysis of pressure signal extracted from vortex breakdown region. The amplitude values on the ordinate are determined by multiplying the respective Fourier coefficient with its complex conjugate and dividing by the signal length.

in Fig. 5.22, the dominant nondimensional frequency appearing is $f_{dom,SIM} \approx 2.4$. An empirically derived formula estimating the vortex breakdown frequency is given in [85]:

$$f_{dom,EST} = \frac{1}{x/c_r \cdot c_r \cot \varphi_W} \frac{U_\infty}{\sin \alpha} (0.28 \pm 0.025) \,, \tag{5.1}$$

where U_∞ and φ denote free stream velocity and sweep angle, respectively. For the configuration and free stream conditions considered, this leads to an expected nondimensional frequency $f_{dom,EST}$ at the point of extraction of $f_{dom,EST} \approx 1.6 - 1.9$. The observed frequency range in the experiment was slightly higher, $f_{dom,EXP} \approx 1.8 - 2.2$ [38], so the dominant frequency in the simulation confirms this observation and is overall in good agreement.

5.2 Sharp Leading Edge (SLE) - angles of attack of $13°$, $18°$, and $23°$

As previously stated, the SLE configuration is computationally easier than the MRLE configuration since the primary vortex separation is geometrically fixed at the leading edge. Considering the main flow characteristics, the numerical investigations show overall very good agreement with the experimental results with only minor discrepancies

regarding the separation line. Again, there is no secondary vortex for any of the three angles of attack. The velocity and pressure distributions deviate slightly from the experimental measurements at the upstream cross sections, significantly less than for the MRLE, though. The agreement at the downstream cross sections is good, and vortex breakdown position and frequency are predicted well. A detailed discussion of the results is given in the following subsections.

5.2.1   Main flow characteristics

As for the MRLE, the expected vortex topologies are predicted correctly for all angles of attack considered, apart from the secondary vortex, which is not observed for any of the three angles of attack. For $\alpha = 13°$ and $\alpha = 18°$, one observes a fully developed leading edge vortex and a counter rotating trailing edge vortex, see left and center column of Fig. 5.23, respectively. For $\alpha = 23°$, one observes a fully developed leading edge vortex with vortex breakdown above the wing, and a counter rotating trailing edge vortex, see right column of Fig. 5.23. Contrary to the simulations with the MRLE, vortex breakdown had to be triggered by a small disturbance, e.g. by inserting small spheres downstream of the wing's trailing edge, see Fig. 5.24. As previously mentioned, vortex breakdown is sensitive to small disturbances in the surrounding conditions, and the fixed boundary conditions with no disturbances used in the simulations thus do not perfectly represent the wind tunnel conditions. Note that other forms of disturbances, e.g. marginally moving or rescaling the geometry also provoked vortex breakdown, indicating that very small disturbances may suffice. As for the MRLE, the secondary vortex is expected to be small [88] for this configuration, which is again corroborated by the experimental measurements, where the secondary vortex is mainly observable on the oil flow pictures but not in the velocity and pressure measurements. As argued in the case of the MRLE, the grid resolution on the upper wing surface in conjunction with the TBLE wall model is insufficient to represent this small-scale flow feature, confirming observations made in [125] and [110]. The vortex system leads to the characteristic pressure coefficient distribution on the upper surface of the wing with a suction peak below the axis of the primary vortex, see bottom row of Fig. 5.23. The main flow features depicted in Fig. 5.1 are predicted correctly regardless of the use of the wall model, indicating that the wall model does not have a major impact for this type of flow, an observation already made in a previous study [74] and confirming the results of the simulations with the MRLE.
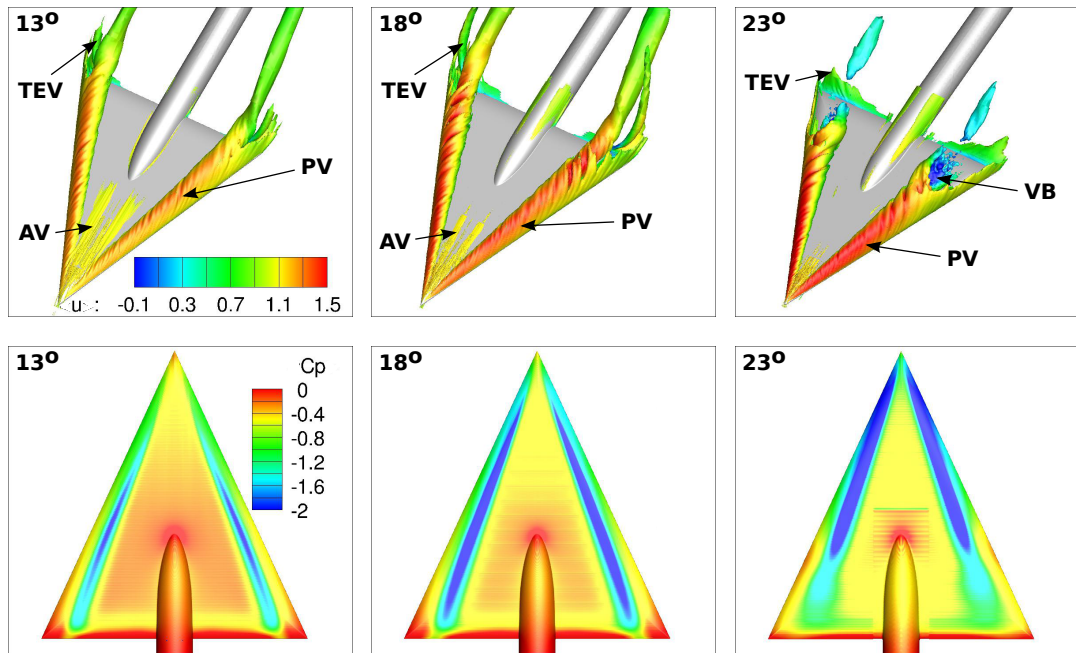
FIGURE 5.23: SLE: Main flow characteristics for angles of attack of 13° (left), 18° (center), and 23° (right), obtained with Grid 4. AV - apex vortex, PV - primary vortex, TEV - trailing edge vortex, VB - vortex breakdown. Top row shows isosurfaces of streamwise vorticity ($\omega_x = \pm 20$) colored by streamwise velocity. Bottom row shows pressure coefficient distribution on upper wing surface.
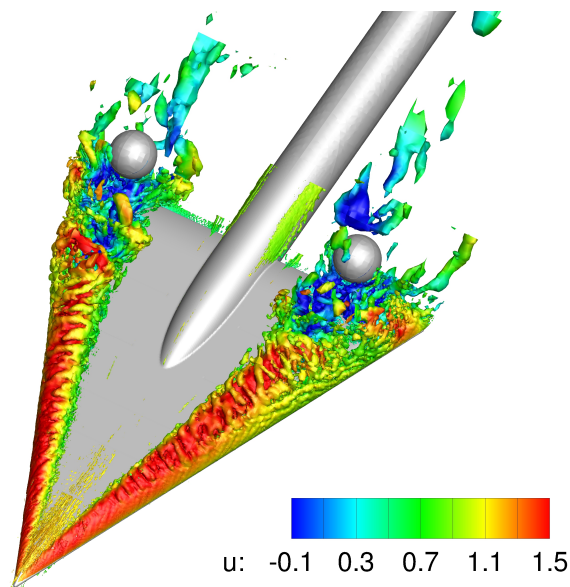
FIGURE 5.24: SLE, $\alpha = 23°$. Small spheres downstream of the wing's trailing edge to trigger vortex breakdown.

A comparison of streamlines close to the wing surface with experimental oil flow visualizations, see Fig. 5.25, shows a significantly better prediction of the separation line position than for the MRLE, marginally away from the leading edge, however, and not precisely at the leading edge, as expected for the SLE. The latter observation can be explained by the fact that the employed immersed boundary technique represents the SLE as slightly rounded, see Fig. 4.4.

Therefore, for $\alpha = 13°$, the primary vortex leads to a primary vortex separation line originating slightly away from the leading edge and a little displaced from the apex. In comparison with the MRLE, however, it lies significantly closer to the leading edge and not as much displaced from the apex, see Fig. 5.2. The primary vortex attachment line observed in the simulation lies further inboard in the front part and approximately at the same position close to the trailing edge. The secondary vortex separation and attachment lines are not observed in the simulation.

For $\alpha = 18°$, the fully developed leading edge vortex leads to a primary vortex separation line originating close to the apex. Again, as for $\alpha = 13°$, the primary vortex separation line does not lie exactly at the leading edge as in the experiment, but slightly inboard. In comparison with $\alpha = 13°$, the primary vortex attachment line is located further inboard in both experiment and simulation, and comparing simulation with experiment, one again observes that the attachment line lies further inboard in the front part and approximately at the same position at the trailing edge. For $\alpha = 18°$, the secondary vortex separation and attachment lines are again only visible in the experiment.

For $\alpha = 23°$, the fully developed leading edge vortex leads to a primary vortex separation line originating close to the apex, which, as for the other two angles of attack, again lies slightly away from the leading edge. The primary vortex attachment line lies close to the center of the wing in both experiment and simulation. Again, secondary vortex separation and attachment lines have only been observed in the experiment.

As mentioned at the beginning of this paragraph, the primary vortex separation line does not lie exactly at the leading edge for all three angles of attack considered, notably in the front part, which is caused by the fact that the immersed boundary method employed does not accurately represent the sharp leading edge. However, comparing SLE with MRLE, the overall trend is correct, that is, for the SLE the separation line is - almost - at the leading edge, whereas for the MRLE, it is significantly displaced from the leading edge. Moreover, grid refinement improves both separation line position and geometry representation.
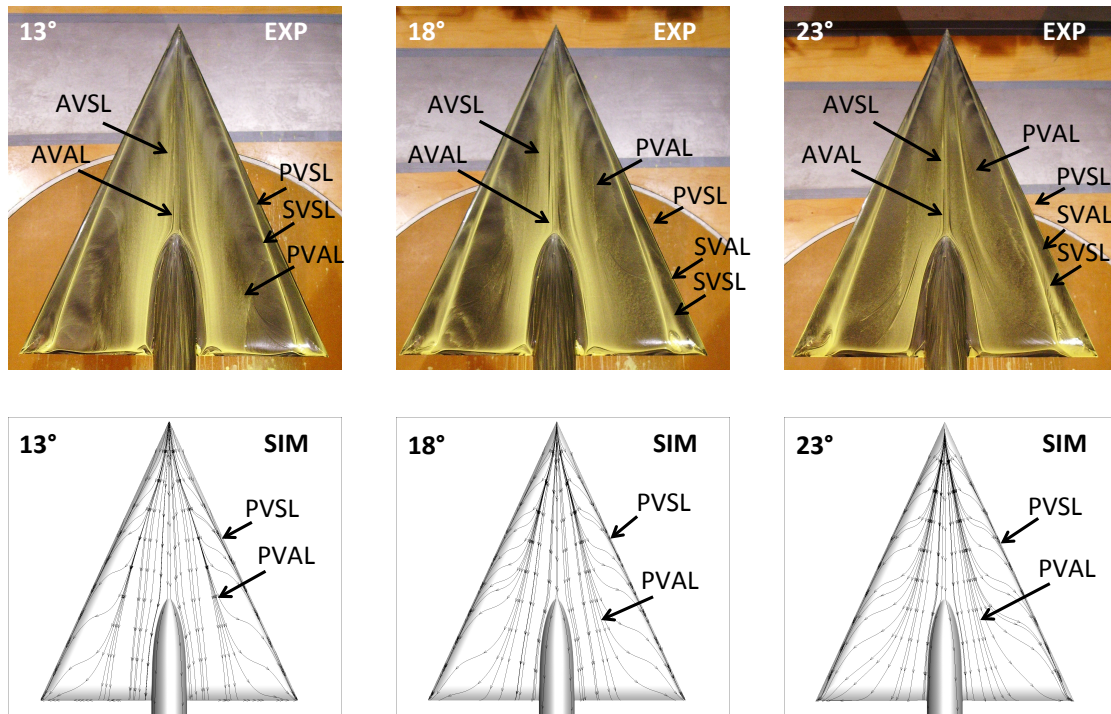
FIGURE 5.25: SLE: Comparison of vortex footprint on upper surface: experimental oil flow visualization (top row) [38, 40, 41] and surface streamlines from simulations with Grid 4 (bottom row). PVSL - primary vortex separation line, PVAL - primary vortex attachment line, SVSL - secondary vortex separation line, SVAL - secondary vortex attachment line.

5.2.2 Velocity distribution and velocity fluctuation intensities

A comparison of the velocity distribution at different cross sections, shown in Figs. 5.26 & 5.27, 5.28 & 5.29, and 5.30 & 5.31 for $\alpha = 13°$, $\alpha = 18°$, and $\alpha = 23°$, respectively, is overall in good accordance with the experimental data and in line with the previous observations.

For $\alpha = 13°$, at cross sections $x/c_r = 0.2$ and $x/c_r = 0.4$, the velocity distribution obtained with Grid 4 is overall in reasonable agreement with the experimental data with only minor differences. At $x/c_r = 0.6$, the velocity distribution shows a higher maximum streamwise velocity and the vortex core lies slightly closer to the wing surface than in the simulation but laterally at the same position, similar to what has been observed for the MRLE. At $x/c_r = 0.8$ and $x/c_r = 0.95$, the velocity distribution obtained in the simulation again shows a higher maximum streamwise velocity and the vortex core lies closer to the leading edge than in the simulation but vertically at approximately the

same position, which is again similar to the observation made for the MRLE.

For $\alpha = 18°$, at cross section $x/c_r = 0.2$, the velocity distribution obtained in the simulation shows a significantly smaller region of high streamwise velocity and the overall shape shows some discrepancies. At $x/c_r = 0.4$ and $x/c_r = 0.6$, the velocity distribution is in good agreement with the experimental measurements. At $x/c_r = 0.8$, the overall shape of the velocity distribution is in good agreement, but the vortex core is located closer to the leading edge than in the experiment. At $x/c_r = 0.95$, the simulation shows a large region of high streamwise velocity, whereas the region is significantly smaller in the experiment. Furthermore, the vortex core lies again closer to the leading edge in the simulation. Overall, the observations are very similar to the observations made for the MRLE.

For $\alpha = 23°$, at cross section $x/c_r = 0.2$, the velocity distributions obtained with Grid 4 and Grid 45 are in reasonable agreement with the experimental data but show a slightly different shape. For Grid 4, the discrepancies regarding the shape are more pronounced. At $x/c_r = 0.4$ and $x/c_r = 0.6$, the velocity distributions are in good agreement with the experimental data for both Grid 4 and Grid 45. However, the vortex core lies closer to the leading edge than in the experiment for the latter cross section and the shape still shows minor discrepancies. At $x/c_r = 0.8$ and $x/c_r = 0.95$, experiment and both simulations (Grid 4 and Grid 45) show a region of negative streamwise velocity indicating that vortex breakdown has already occurred. Both shape and magnitude of the velocity distribution show some discrepancies, however, notably regarding the size of the region of negative streamwise velocity, which is predicted significantly larger in the simulations. This is particularly surprising for the simulation with Grid 4, in which vortex breakdown occurred more downstream than in the experiment ($x/c_r \approx 0.77$ vs. $x/c_r \approx 0.68$), and thus one would rather expect a smaller region of negative streamwise velocity.

Distributions of streamwise velocity fluctuation intensities at different cross sections for $\alpha = 23°$, see Figs. 5.32 - 5.34, exhibit the characteristic shape expected from the experiments [87], but show minor differences regarding magnitude: Upstream of the vortex breakdown location, i.e. $x/c_r = 0.2$, $x/c_r = 0.4$, and $x/c_r = 0.6$, $u_{RMS} \approx 20-30\%$ in the region of the primary vortex and $u_{RMS} \approx 0\%$ outside of the vortex. Between $x/c_r = 0.65$ and $x/c_r = 0.75$, i.e. at or close to the vortex breakdown location, the velocity fluctuation intensity significantly increases and reaches $u_{RMS} \approx 50-60\%$ with peak values up to $u_{RMS} \approx 90\%$ in the vortex core. This region of maximum turbulence intensity rapidly
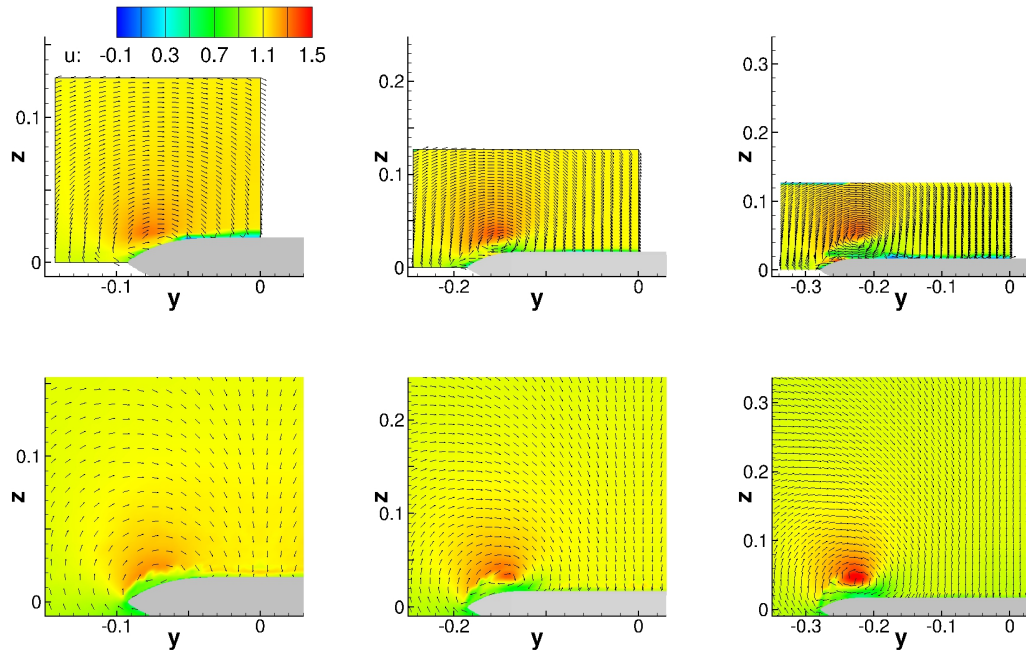
FIGURE 5.26: SLE, $\alpha = 13°$: Velocity distribution at cross sections $x/c_r = 0.2, 0.4$, and 0.6 (from left to right). Top row shows experimental measurements [38, 40, 41], bottom row shows results of simulation with Grid 4 and simple no-slip condition.
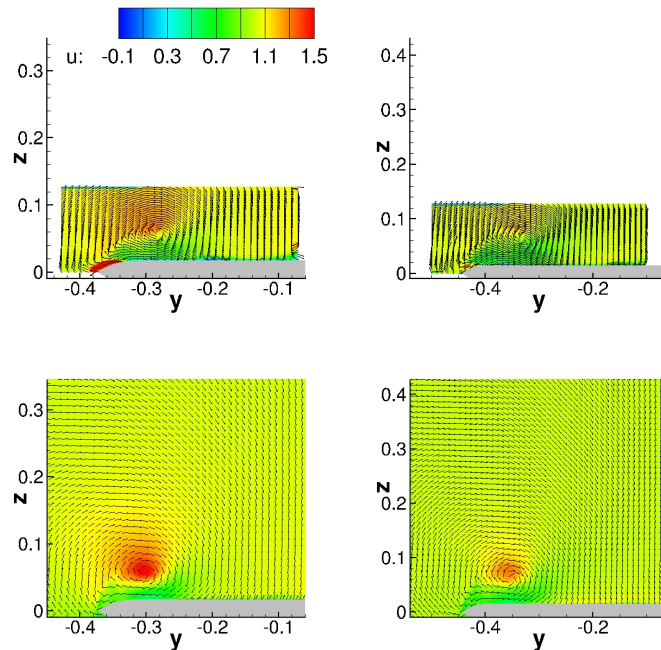
FIGURE 5.27: SLE, $\alpha = 13°$: Velocity distribution at cross sections $x/c_r = 0.8$ and 0.95 (from left to right). Top row shows experimental measurements [38, 40, 41], bottom row shows results of simulation with Grid 4 and simple no-slip condition.
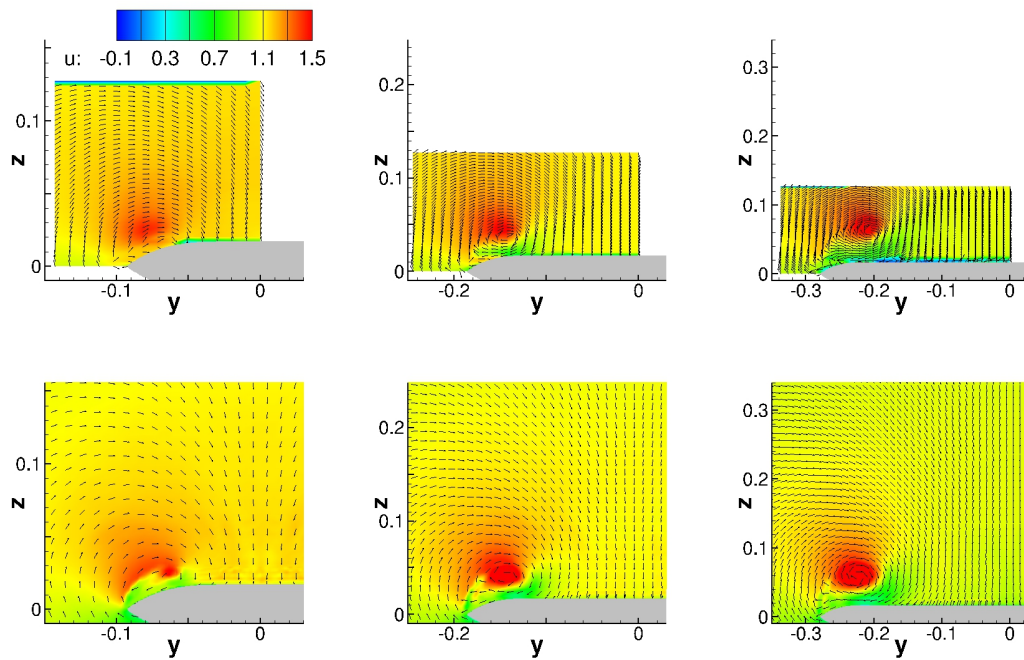
FIGURE 5.28: SLE, $\alpha = 18°$: Velocity distribution at cross sections $x/c_r = 0.2, 0.4$, and 0.6 (from left to right). Top row shows experimental measurements [38, 40, 41], bottom row shows results of simulation with Grid 4 and simple no-slip condition.
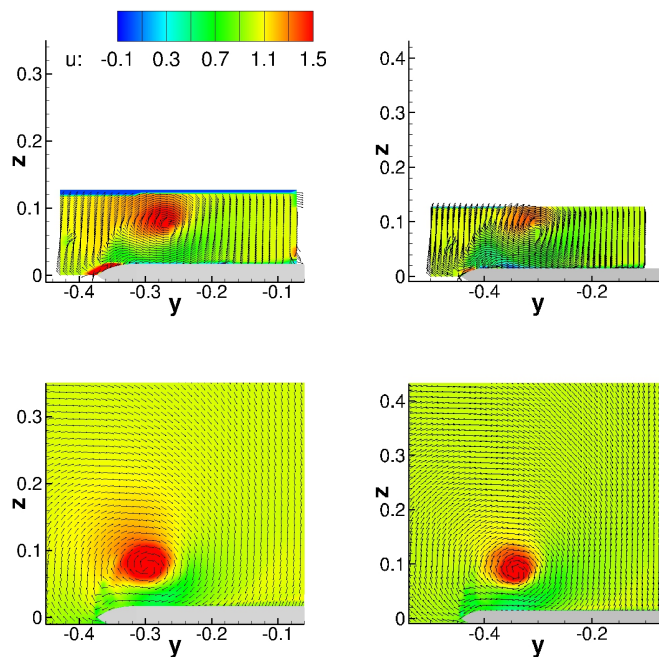
FIGURE 5.29: SLE, $\alpha = 18°$: Velocity distribution at cross sections $x/c_r = 0.8$ and 0.95 (from left to right). Top row shows experimental measurements [38, 40, 41], bottom row shows results of simulation with Grid 4 and simple no-slip condition.
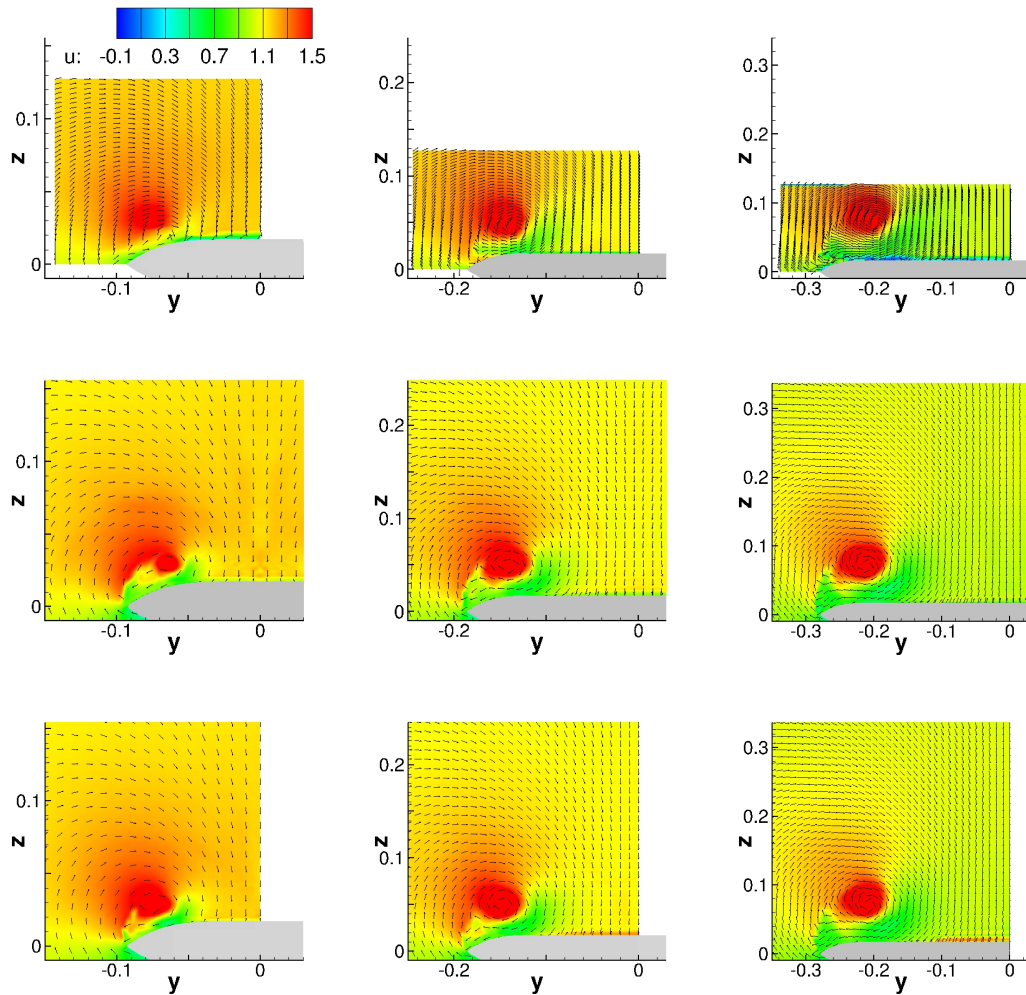
FIGURE 5.30: SLE, $\alpha = 23°$: Velocity distribution at cross sections $x/c_r = 0.2, 0.4$, and 0.6 (from left to right). Top row shows experimental measurements [38, 40, 41], center row shows results of simulation with Grid 4 and TBLE wall model, bottom row shows results of simulation with Grid 45 and simple no-slip condition.

expands and annular regions of maximum turbulence intensity $u_{RMS} \approx 30\% - 40\%$ are formed downstream of the vortex breakdown location, see Fig. 5.32. Lateral velocity fluctuations, v_{RMS}, and vertical velocity fluctuations, w_{RMS}, also show qualitatively good agreement, see Figs. 5.33 and 5.34, but are again, as for the MRLE, predicted slightly higher than observed in the experiments [87].

5.2.3 Surface pressure distribution and surface pressure fluctuation intensities

A quantitative comparison of the pressure coefficient (C_p) distribution at different cross sections of the wing, see Figs. 5.35 - 5.37, confirms the previous observations, showing
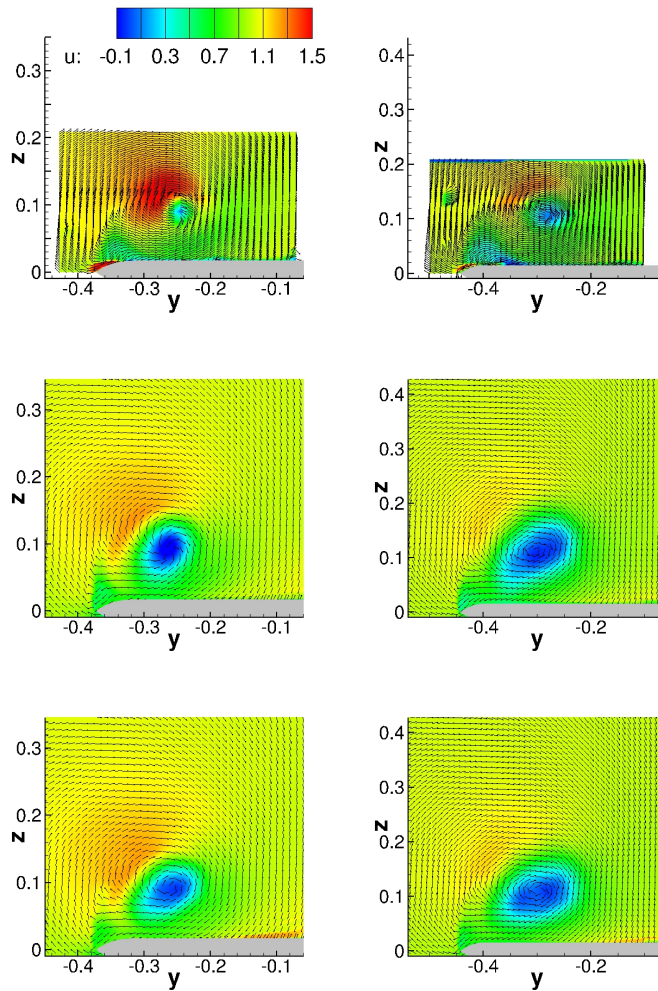
FIGURE 5.31: SLE, $\alpha = 23°$: Velocity distribution at cross sections $x/c_r = 0.8$ and 0.95 (from left to right). Top row shows experimental measurements [38, 40, 41], center row shows results of simulation with Grid 4 and TBLE wall model, bottom row shows results of simulation with Grid 45 and simple no-slip condition.

overall better agreement than for the MRLE, but still some discrepancies in the apex region.

For $\alpha = 13°$, the simulations fail to predict the suction peak close to the leading edge at $x/c_r = 0.2$, as for the MRLE. At $x/c_r = 0.4$, the suction peak is of slightly lower magnitude and located slightly inboard. At $x/c_r = 0.6$, the magnitude of the suction peak is predicted slightly higher but its location coincides with the experiment's. At $x/c_r = 0.8$ and $x/c_r = 0.95$, the suction peak's magnitude is again predicted higher and the location is slightly closer to the leading edge, confirming the observation made in the preceding sections.

For $\alpha = 18°$, the simulations again fail to predict the suction peak close to the leading edge at $x/c_r = 0.2$. At $x/c_r = 0.4$, the magnitude of the suction peak is predicted
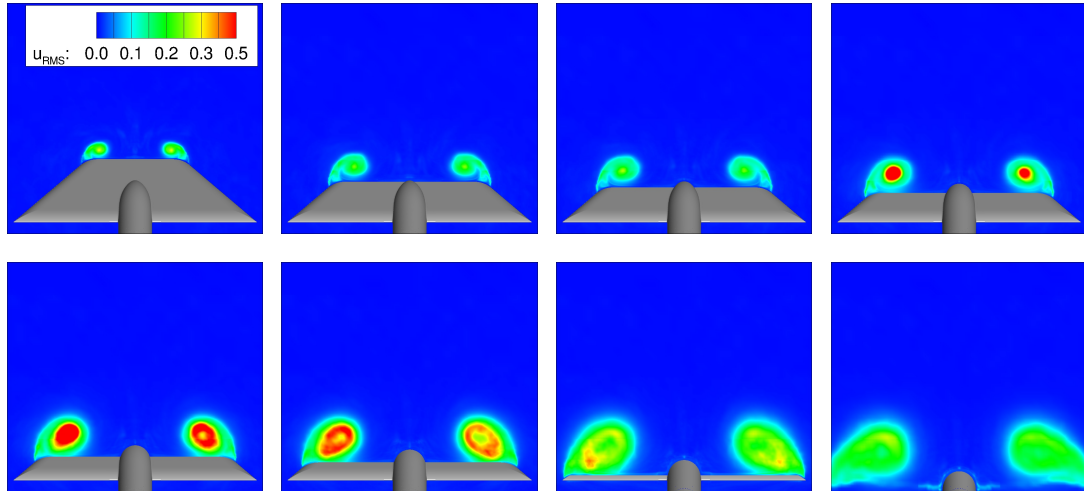
FIGURE 5.32: SLE, $\alpha = 23°$: Velocity fluctuation intensities u_{RMS} at cross sections $x_g/c_r = 0.4, 0.6, 0.65$, and 0.7 (top row from left to right) and $x_g/c_r = 0.75, 0.8, 0.9$, and 1.0 (bottom row from left to right). Simulation with Grid 4 and TBLE wall model.
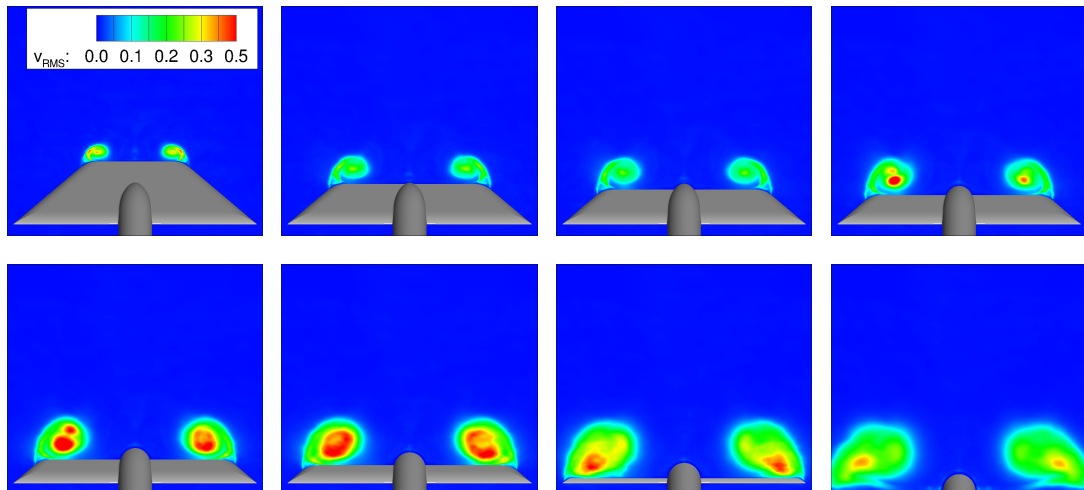
FIGURE 5.33: SLE, $\alpha = 23°$: Velocity fluctuation intensities v_{RMS} at cross sections $x_g/c_r = 0.4, 0.6, 0.65$, and 0.7 (top row from left to right) and $x_g/c_r = 0.75, 0.8, 0.9$, and 1.0 (bottom row from left to right). Simulation with Grid 4 and TBLE wall model.

equally high as measured in the experiments but its location is slightly inboard. At $x/c_r = 0.6$ and $x/c_r = 0.8$, the location of the suction peak is predicted slightly closer to the leading edge and the magnitude is predicted higher than in the experiment. At the most downstream cross section, the suction peak is predicted slightly higher and closer to the leading edge than observed in the experiments, which is in line with previous observations.

For $\alpha = 23°$, the simulations with Grid 4 show a suction peak which is located slightly inboard and lower in magnitude at cross section $x/c_r = 0.2$. Using Grid 45, which is
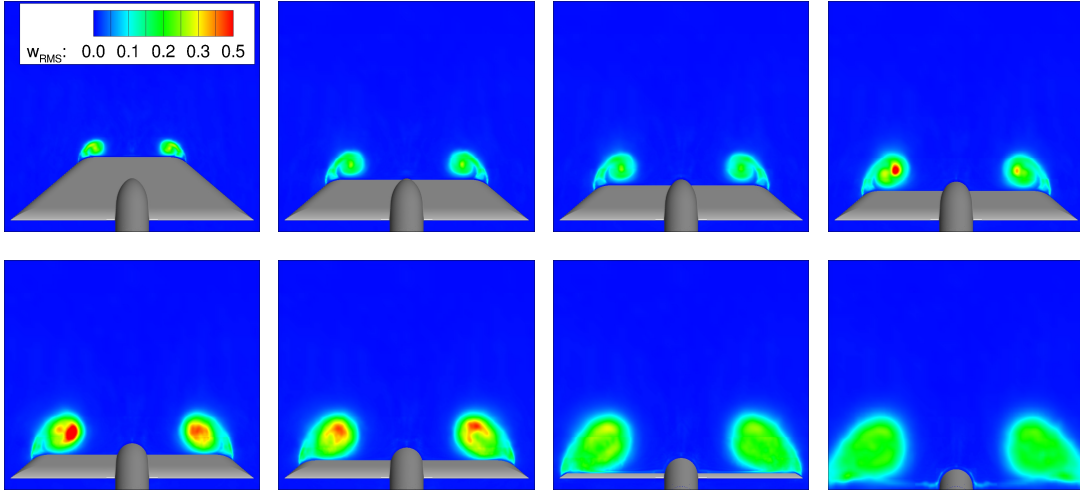
FIGURE 5.34: SLE, $\alpha = 23°$: Velocity fluctuation intensities w_{RMS} at cross sections $x_g/c_r = 0.4, 0.6, 0.65$, and 0.7 (top row from left to right) and $x_g/c_r = 0.75, 0.8, 0.9$, and 1.0 (bottom row from left to right). Simulation with Grid 4 and TBLE wall model.

refined in the region close to the apex, the suction peak is predicted significantly better and shows good agreement with the experimental measurements. At $x/c_r = 0.4$, the C_p distribution obtained with Grid 4 shows a suction peak of same magnitude located slightly inboard of the experiment. For Grid 45, both suction peak's location and magnitude are in very good agreement with the experiment. At $x/c_r = 0.6$ and $x/c_r = 0.8$, the simulations with both grids predict a suction peak with approximately same magnitude and location as measured in the experiments. For Grid 45, the agreement with the experimental data is overall better for these two cross sections. At the most downstream cross section $x/c_r = 0.95$, the suction peak is predicted slightly outboard and slightly higher for Grid 4 and Grid 45 with overall better agreement for Grid 45. For $\alpha = 23°$, the TBLE wall model slightly improved the predicted C_p distribution at all cross sections. However, the improvement due to the TBLE wall model is significantly less than the improvement obtained by refining the grid, confirming the observations made for the MRLE and corroborating again that the effect of the wall model is marginal.

A quantitative comparison of the pressure coefficient fluctuations ($C_{p,RMS}$), shown in Figs. 5.38 - 5.40 for simulations with Grid 4, shows good agreement regarding the peak values in the region of the primary vortex, with minor discrepancies in line with the computed C_p distributions, but partly significantly higher fluctuation levels inboard of the primary vortex.

For $\alpha = 13°$, the overall shape of the $C_{p,RMS}$ distribution is similar to the experimental
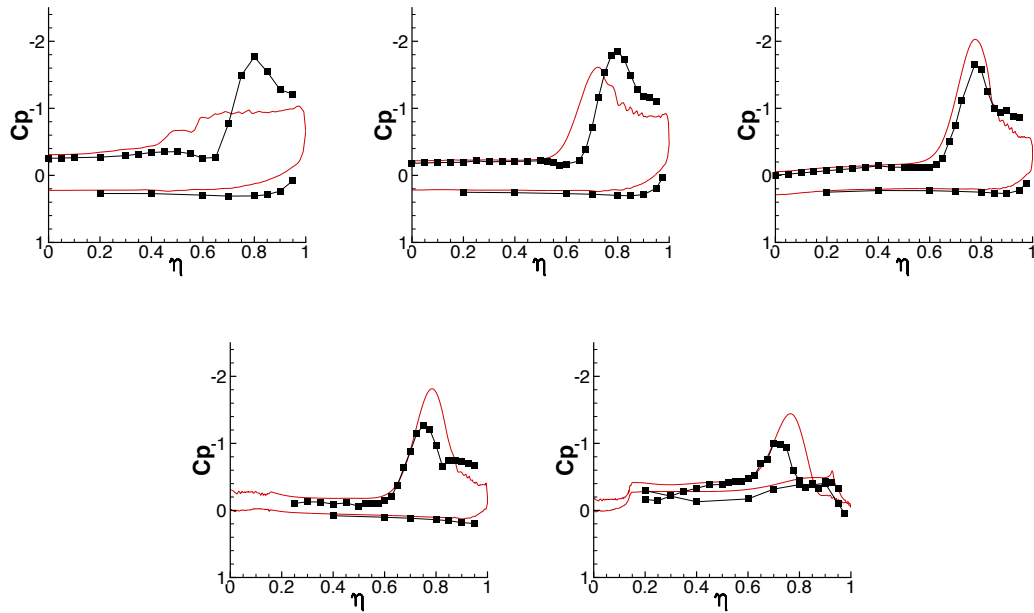
FIGURE 5.35: SLE, $\alpha = 13°$: Surface pressure distribution C_p at cross sections $x/c_r = 0.2, 0.4, 0.6, 0.8$ and 0.95 (from left to right and from top to bottom). Grid 4 with simple no-slip condition - red; Experiments [38, 40, 41] - black. η denotes normalized local half span width.
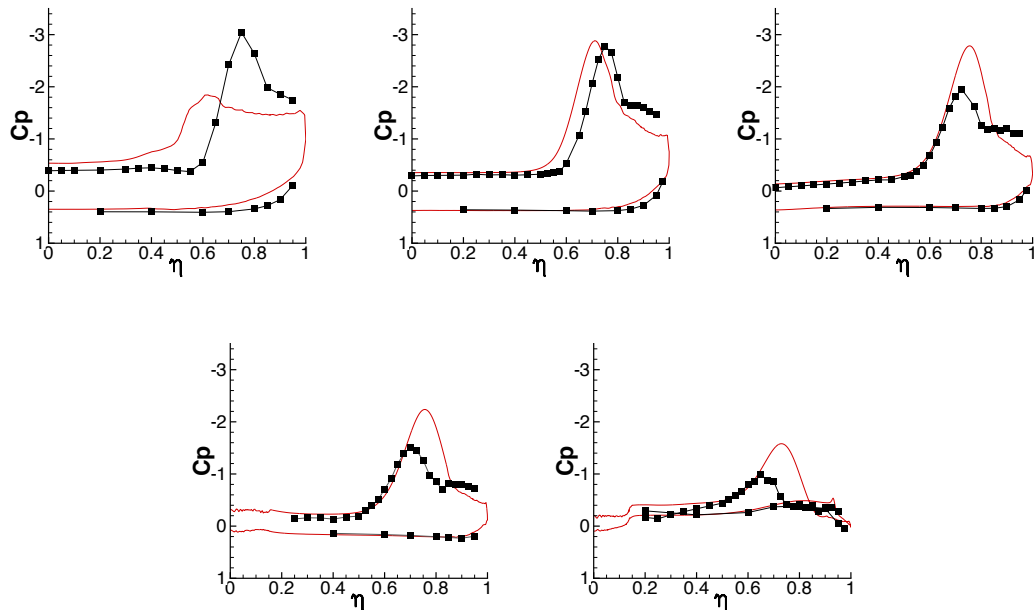
FIGURE 5.36: SLE, $\alpha = 18°$: Surface pressure distribution C_p at cross sections $x/c_r = 0.2, 0.4, 0.6, 0.8$ and 0.95 (from left to right and from top to bottom). Grid 4 with simple no-slip condition - red; Experiments [38, 40, 41] - black. η denotes normalized local half span width.
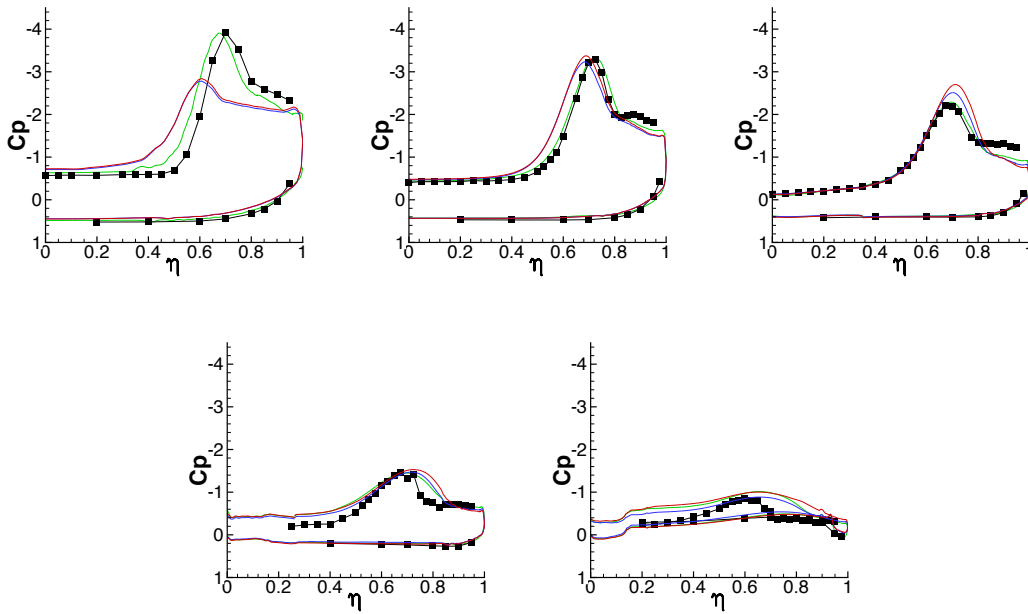
FIGURE 5.37: SLE, $\alpha = 23°$: Surface pressure distribution C_p at cross sections $x/c_r = 0.2, 0.4, 0.6, 0.8$ and 0.95 (from left to right and from top to bottom). Grid 4 with TBLE wall model - blue; Grid 4 with simple no-slip condition - red; Grid 45 with simple no-slip condition - green; Experiments [38, 40, 41] - black. η denotes normalized local half span width.

data at all four cross sections, $x/c_r = 0.4$, $x/c_r = 0.6$, $x/c_r = 0.8$, and $x/c_r = 0.95$, but the fluctuation level is predicted significantly higher in the inner part of the wing.

For $\alpha = 18°$, the overall shape of the $C_{p,RMS}$ distribution shows again similar behavior as the experimental data. The maximum levels of fluctuation intensity are predicted quite well for all four cross sections and the locations of the peak levels show only minor discrepancies, which is in agreement with the previous observations. However, as for $\alpha = 13°$, the level of fluctuation intensity inboard of the primary vortex is predicted significantly higher, particularly at the upstream cross sections.

For $\alpha = 23°$, the predictions show good agreement at cross section $x/c_r = 0.4$ and reasonable agreement at $x/c_r = 0.6$. At $x/c_r = 0.8$ and $x/c_r = 0.95$, the fluctuation level is predicted quite well in the region inboard of the primary vortex, contrary to the other two angles of attack, but the peak values in the region of the primary vortex are predicted significantly higher, an observation already made for the MRLE. As stated beforehand, this is in accordance with the general expectation of significantly increased fluctuation levels in the vortex breakdown region, and the experimental results at these cross sections are thus surprising.
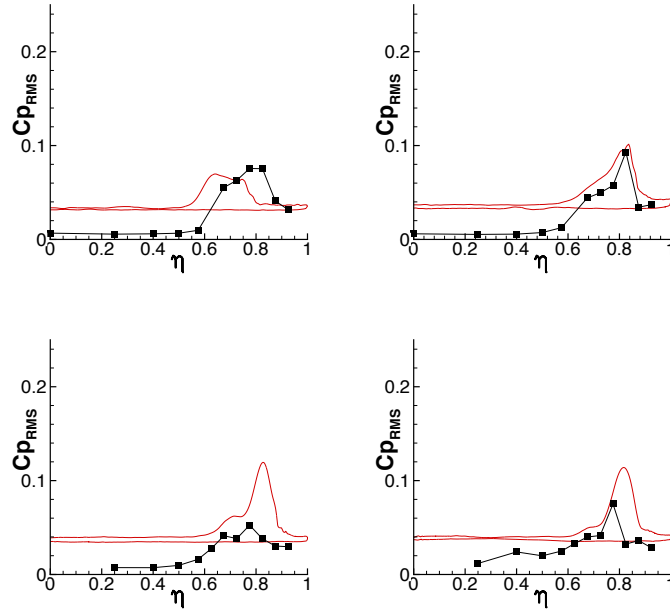
FIGURE 5.38: SLE, $\alpha = 13°$: Surface pressure fluctuation intensities $C_{p,RMS}$ at cross sections $x/c_r = 0.4, 0.6, 0.8$ and 0.95 (from left to right and from top to bottom). Grid 4 with simple no-slip condition - red; Experiments [38, 40, 41] - black. η denotes normalized local half span width.
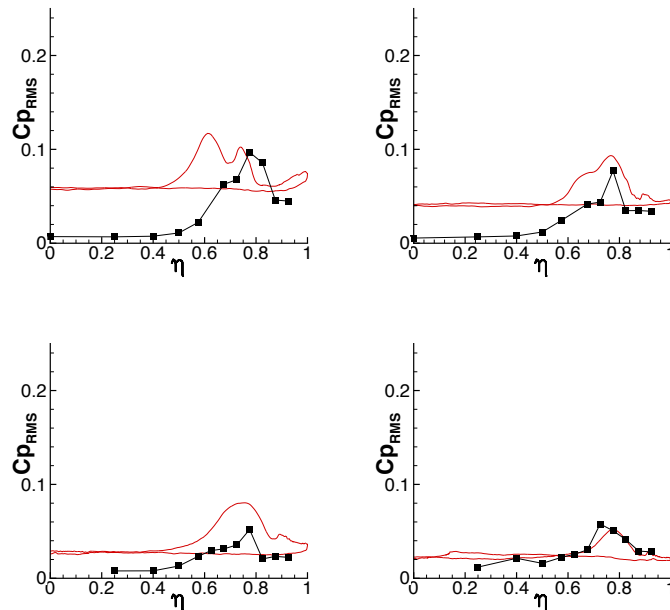
FIGURE 5.39: SLE, $\alpha = 18°$: Surface pressure fluctuation intensities $C_{p,RMS}$ at cross sections $x/c_r = 0.4, 0.6, 0.8$ and 0.95 (from left to right and from top to bottom). Grid 4 with simple no-slip condition - red; Experiments [38, 40, 41] - black. η denotes normalized local half span width.
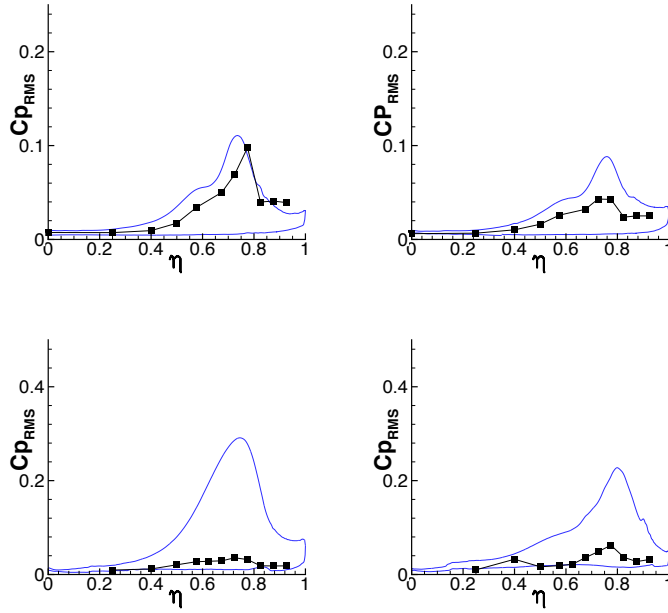
FIGURE 5.40: SLE, $\alpha = 23°$: Surface pressure fluctuation intensities $C_{p,RMS}$ at cross sections $x/c_r = 0.4, 0.6, 0.8$ and 0.95 (from left to right and from top to bottom). Grid 4 with TBLE wall model - blue; Experiments [38, 40, 41] - black. η denotes normalized local half span width.

5.2.4 Vortex breakdown position and frequency

Vortex breakdown, indicated by zero or negative streamwise velocities in the vortex core, was observed at $x/c_r \approx 0.77$ for Grid 4 and at $x/c_r \approx 0.69$ for Grid 45. These results are in good agreement with the experimental result, $x/c_r \approx 0.68$ [38]. The vortex breakdown is of helical type, see Fig. 5.41, and the vortex axis's rotation is opposite to the primary vortex's rotation, as described in [13] and as observed for the MRLE, see Fig. 5.21.

In order to determine the frequency of the vortex breakdown occurring in the simulation, a pressure signal has been extracted from a point in the vortex breakdown region ($x_g = 0.77$, $y_g = 0.24$, $z_g = -0.23$) and analyzed by a Fourier transform. As one can see in Fig. 5.42, the dominant nondimensional frequency appearing is $f_{dom,SIM} \approx 3.0$. As mentioned previously, the vortex breakdown frequency can be estimated via [85]

$$f_{dom,EST} = \frac{1}{x/c_r \cdot c_r \, cot \, \varphi_W} \frac{U_\infty}{sin \, \alpha} (0.28 \pm 0.025) \, , \tag{5.2}$$
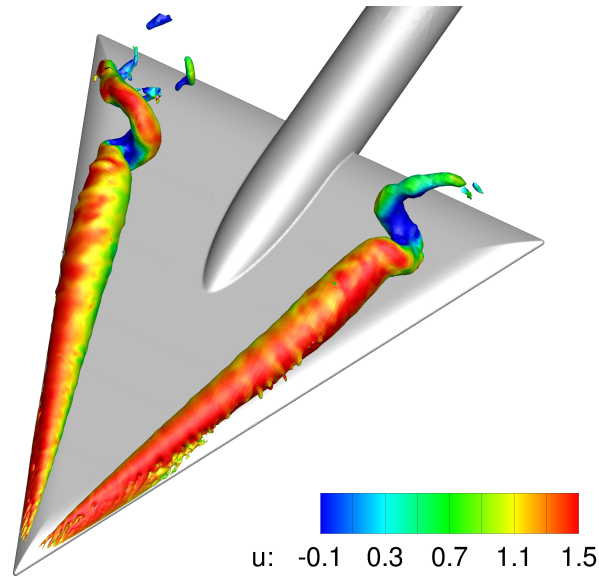
FIGURE 5.41: SLE, $\alpha = 23°$: Helical form of vortex breakdown. Figure shows isosurface of pressure coefficient ($C_p = -2$) colored by streamwise velocity.
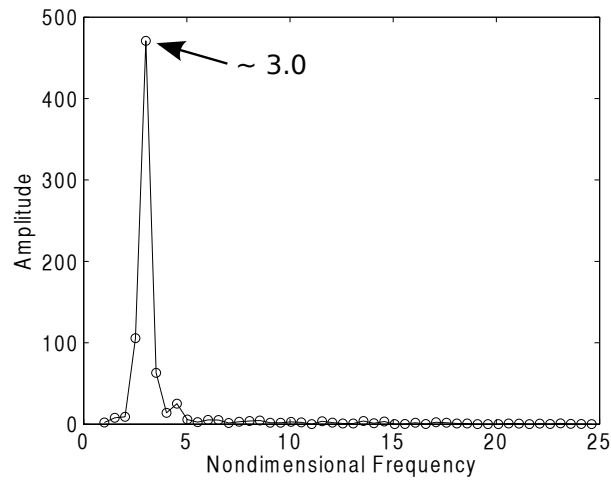
FIGURE 5.42: SLE, $\alpha = 23°$: Frequency analysis of pressure signal extracted from vortex breakdown region. The amplitude values on the ordinate are determined by multiplying the respective Fourier coefficient with its complex conjugate and dividing by the signal length.

which leads to an expected nondimensional frequency $f_{dom,EST}$ at the point of extraction of $f_{dom,EST} \approx 1.7 - 2.1$. The observed frequency range in the experiment by Furman and Breitsamter [38] was slightly higher than this expected frequency, but not as much higher as the dominant frequency observed in the simulation. However, the frequency observed in the simulation is in very good agreement with the results of the more recent experiment by Kölzsch and Breitsamter [126].

Chapter 6

Results of investigations with flow control

This chapter presents results of the simulations with flow control mechanisms, partly published in [123, 124]. It contains two sections. Section one discusses results of the investigations with active flow control through oscillating control surfaces, and, as an outlook, section two briefly presents a flow control approach where fluid from the pressure side is injected on the suction side via a geometric modification of the wing. All simulations in this chapter have been carried out with Grid 3 for the SLE at an angle of attack of $\alpha = 28°$. For this configuration, vortex breakdown occurs - without introducing any disturbances - at $x/c_r \approx 0.7$, and it thus constitutes an expedient case since the vortex breakdown location - the phenomenon of interest in this chapter - is clearly above the wing and the relatively coarse grid allows for saving computational resources.

6.1 Sharp Leading Edge (SLE) - angle of attack of $28°$, oscillating control surfaces

This section describes the investigations of flow control through oscillating control surfaces. The results indicate that oscillating control surfaces have only an insignificant effect on the vortex breakdown location for the configuration considered, which confirms experimental observations.

6.1.1   Description of approach

The control surfaces investigated are the same as the ones used in the experiments conducted at the Institute of Aerodynamics and Fluid Mechanics of Technische Universität München, apart from a larger gap between flap and wing, which was necessary due to the coarse grid. One can expect that the larger gap does not affect the overall effectiveness of the control surface, however [127], and a preliminary simulation showed that the chosen control surface, when not moving, does not affect the flow. The experimental investigations showed that control surfaces in the front part of the wing have a higher impact on the flow than control surfaces in the rear part [128]. Therefore, only control surfaces in the front part have been investigated, see Fig. 6.1. The control surface position in a wing fixed coordinate system is given by

$$
\begin{aligned}
x_{control\ surface} &= 0\,, \\
y_{control\ surface} &= 0\,, \\
z_{control\ surface} &= -C \cdot \frac{1}{2\pi f} sin(2\pi f t)\,,
\end{aligned}
\tag{6.1}
$$

i.e. the flap moves periodically up and down. f and t denote frequency and time, respectively, and the constant C can be modified to allow for different oscillation amplitudes. In the following, a maximum oscillation amplitude of approximately $0.01 \cdot c_r$ has been chosen. In the simulations, the non-dimensional frequencies $f = 2 =: f2$ and $f = 4 =: f4$ have been investigated. These frequencies lie in the range of frequencies investigated experimentally.

6.1.2   Main flow characteristics

Figure 6.2 indicates that the main flow characteristics are only slightly altered by the oscillating control surfaces. In the figure, the results of a simulation without flow control (top row left), a simulation with oscillating flaps and frequency $f2$ (top row center), and a simulation with oscillating flaps and frequency $f4$ (top row right) are shown. One observes that the overall flow looks almost identical, which is also confirmed by the almost coinciding pressure coefficient distributions for the three cases, see bottom row of Fig. 6.2. These results are in agreement with the experimental studies, where
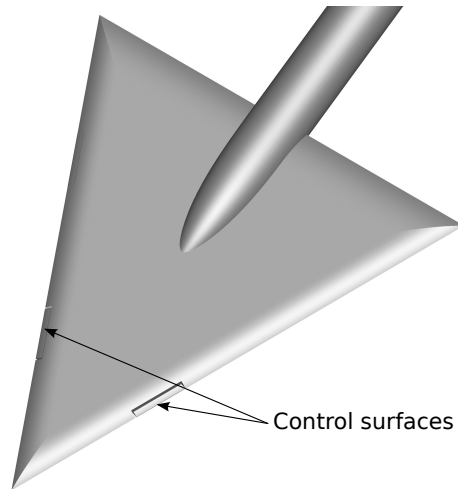
FIGURE 6.1: Control surfaces in the front part of the wing.
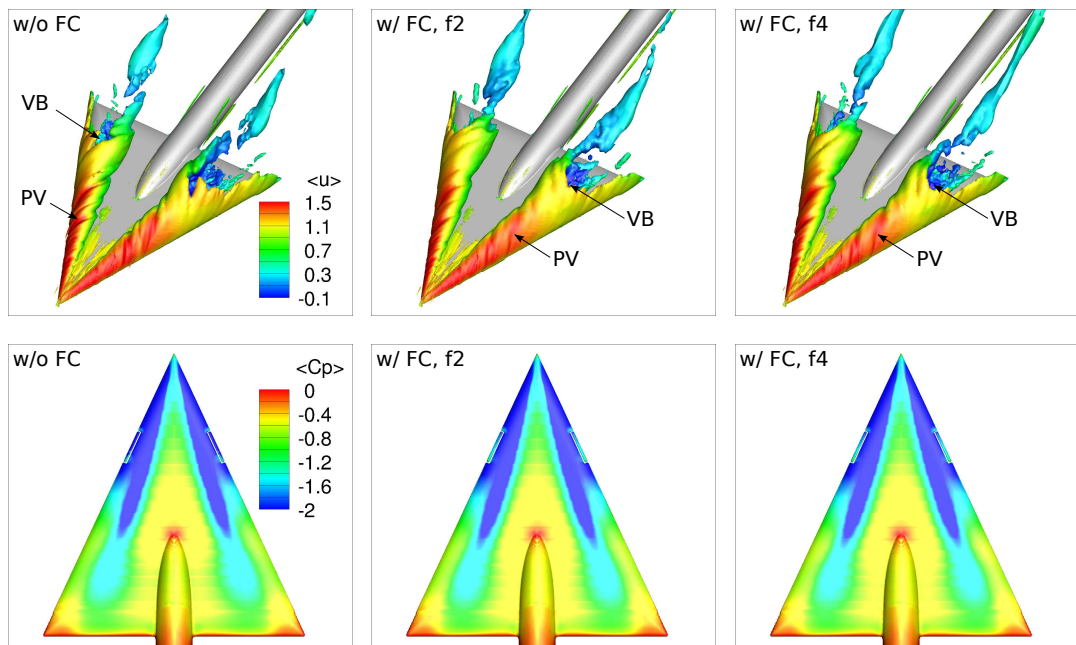
FIGURE 6.2: SLE, $\alpha = 28°$: Main flow characteristics without flow control (FC, left), with flow control and non-dimensional frequency $f = 2$ (f2, center), and with flow control and non-dimensional frequency $f = 4$ (f4, right). PV - primary vortex, VB - vortex breakdown. Top row shows isosurfaces of streamwise vorticity ($\omega_x = \pm 15$) colored by streamwise velocity. Bottom row shows pressure coefficient distribution on upper wing surface.

oscillating flaps also showed only an insignificant effect for angles of attack between $23°$ and $40°$ [128] .

6.1.3   Velocity distribution and velocity fluctuation intensities

A quantitative comparison of the velocity distributions at different cross sections, see Figs. 6.3 - 6.5, confirms the observation made in the previous subsection. There are only very minor differences at the two most downstream cross sections, $x/c_r = 0.8$ and $x/c_r = 0.95$, originating from a slightly different vortex breakdown location, see below.

A comparison of velocity intensity fluctuations, see Figs. 6.6 - 6.8, also shows only minor differences for the three cases, thus confirming the former observations.

6.1.4   Vortex breakdown position

A comparison of the vortex breakdown location, determined by negative streamwise velocity, see Fig. 6.9, shows that oscillating control surfaces delay vortex breakdown by approximately 4 percentage points. For the case without moving flap, vortex breakdown occurs at $x/c_r \approx 0.71$, for the case with moving flap and frequency $f2 = 2$, vortex breakdown occurs at $x/c_r \approx 0.75$, and for the case with moving flap and frequency $f4 = 4$, vortex breakdown also occurs at $x/c_r \approx 0.75$, i.e. the vortex breakdown location moves slightly downstream, but overall, it is only slightly altered by the oscillating flaps, and there is no significant change when modifying the oscillation frequency.

6.2   Sharp Leading Edge (SLE) - angle of attack of $28°$, injecting fluid from the pressure side

This last section is intended as an outlook to other possible flow control mechanisms and describes an approach based on geometric modifications leading to an injection of fluid from the pressure side. The numerical results indicate that this approach can have a significant effect on the vortex breakdown location.

6.2.1   Description of approach

As discussed in section 2.5, flow control via along-the-core blowing or trailing edge jets has been employed successfully to move the vortex breakdown position either downstream or upstream. Contrary to the aforementioned active flow control mechanisms,
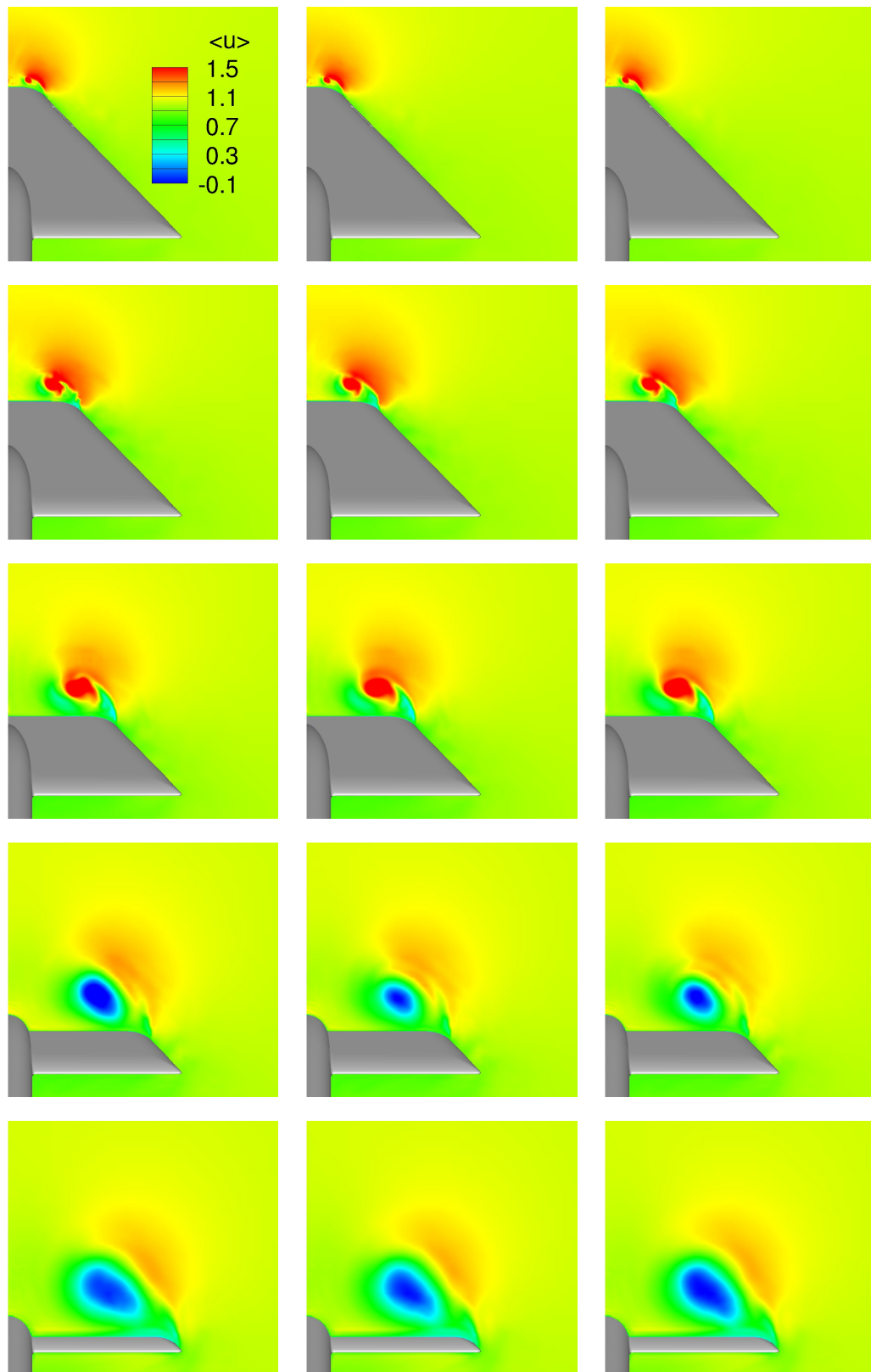
FIGURE 6.3: SLE, $\alpha = 28°$: Streamwise velocity distribution at cross sections $x/c_r = 0.2, 0.4, 0.6, 0.8$, and 0.95 (from top to bottom). Left column shows results without flow control, center column shows results for oscillating control surfaces with $f2 = 2$, right column shows results for oscillating control surfaces with $f4 = 4$.
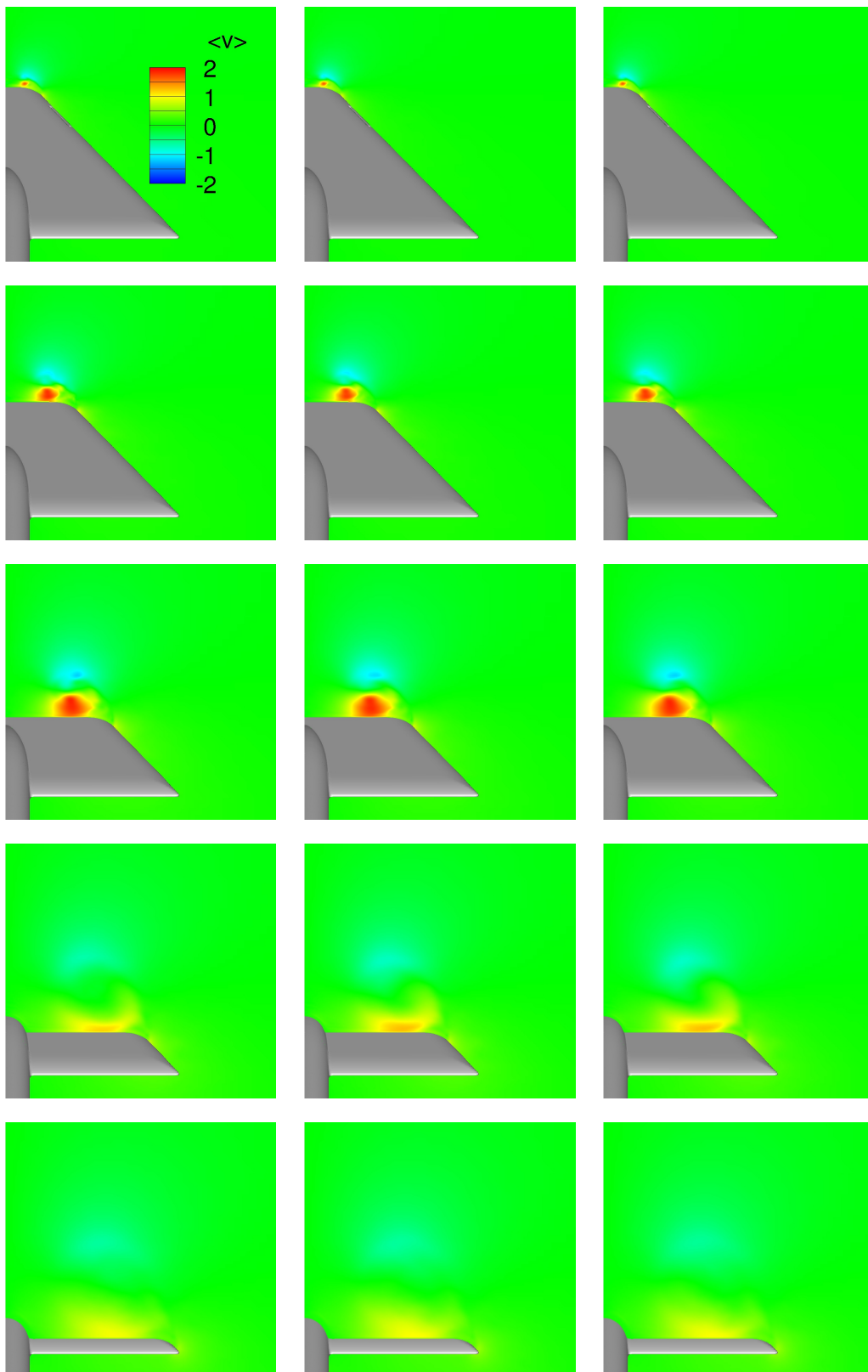
FIGURE 6.4: SLE, $\alpha = 28°$: Spanwise velocity distribution at cross sections $x/c_r = 0.2, 0.4, 0.6, 0.8$, and 0.95 (from top to bottom). Left column shows results without flow control, center column shows results for oscillating control surfaces with $f2 = 2$, right column shows results for oscillating control surfaces with $f4 = 4$.

FIGURE 6.5: SLE, $\alpha = 28°$: Vertical velocity distribution at cross sections $x/c_r = 0.2, 0.4, 0.6, 0.8$, and 0.95 (from top to bottom). Left column shows results without flow control, center column shows results for oscillating control surfaces with $f2 = 2$, right column shows results for oscillating control surfaces with $f4 = 4$.
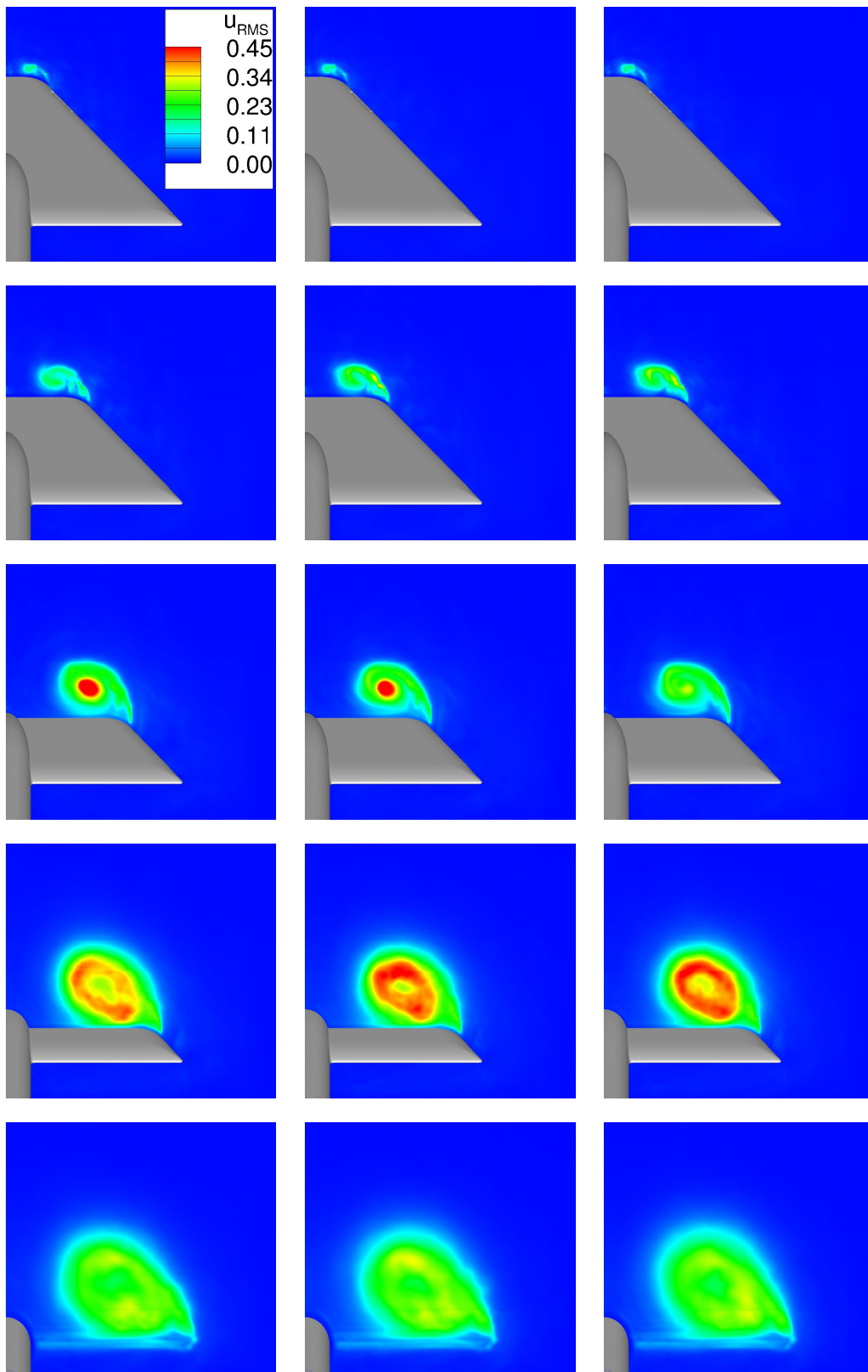
FIGURE 6.6: SLE, $\alpha = 28°$: Velocity intensity fluctuations u_{RMS} at cross sections $x_g/c_r = 0.2, 0.4, 0.6, 0.75,$ and 0.9 (from top to bottom). Left column shows results without flow control, center column shows results for oscillating control surfaces with $f2 = 2$, right column shows results for oscillating control surfaces with $f4 = 4$.
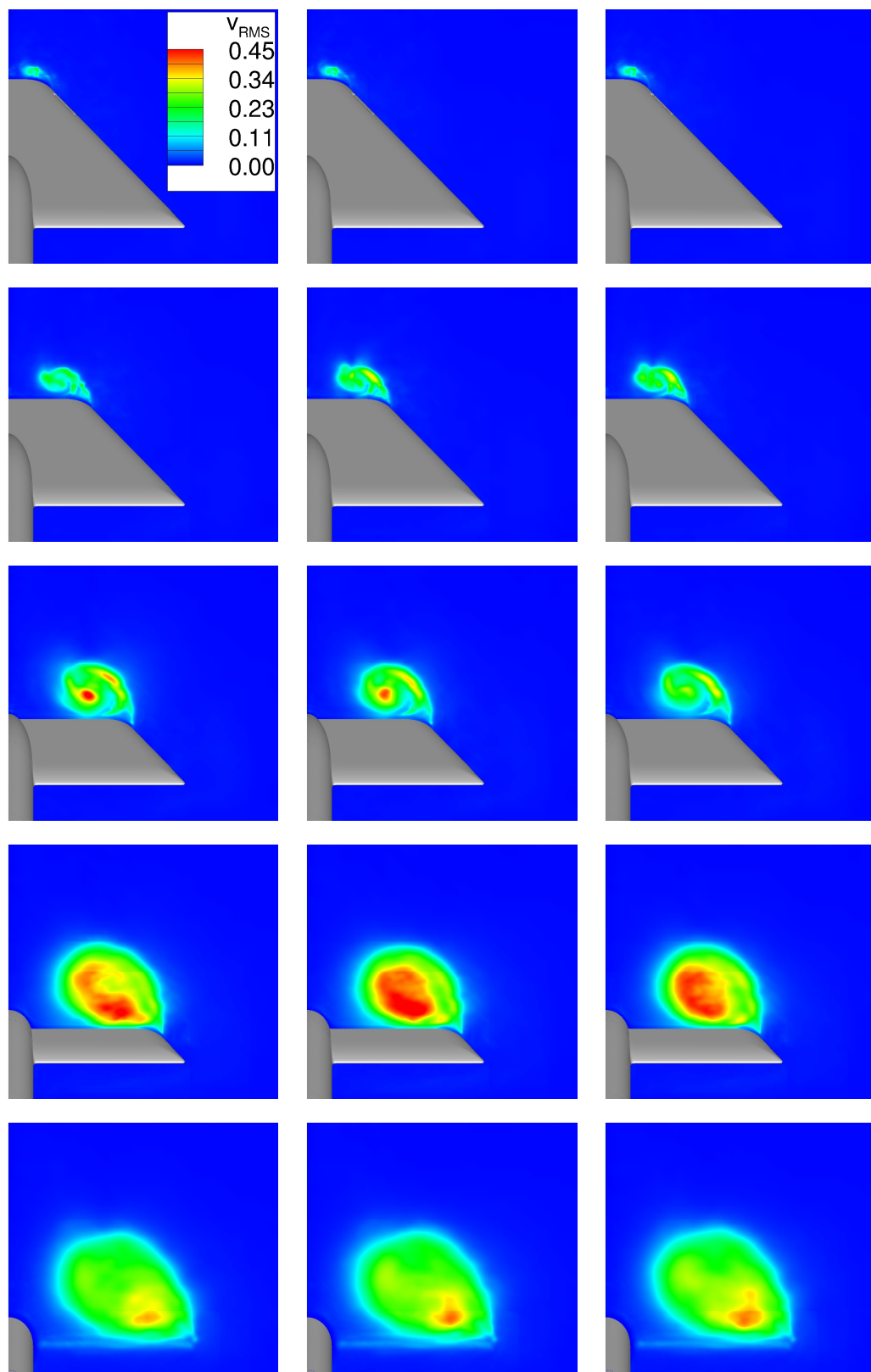
FIGURE 6.7: SLE, $\alpha = 28°$: Velocity intensity fluctuations v_{RMS} at cross sections $x_g/c_r = 0.2, 0.4, 0.6, 0.75$, and 0.9 (from top to bottom). Left column shows results without flow control, center column shows results for oscillating control surfaces with $f2 = 2$, right column shows results for oscillating control surfaces with $f4 = 4$.
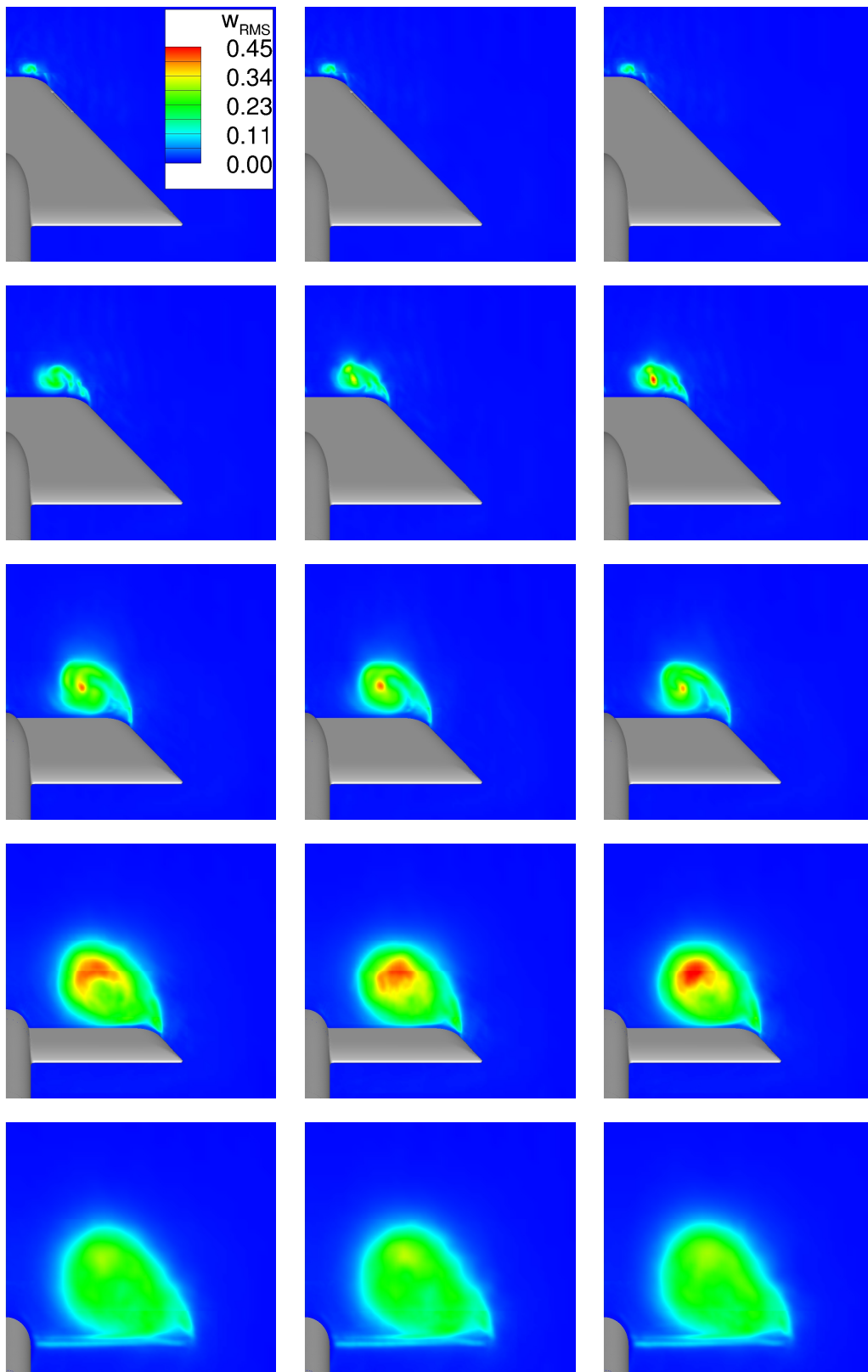
FIGURE 6.8: SLE, $\alpha = 28°$: Velocity intensity fluctuations w_{RMS} at cross sections $x_g/c_r = 0.2, 0.4, 0.6, 0.75$, and 0.9 (from top to bottom). Left column shows results without flow control, center column shows results for oscillating control surfaces with $f2 = 2$, right column shows results for oscillating control surfaces with $f4 = 4$.
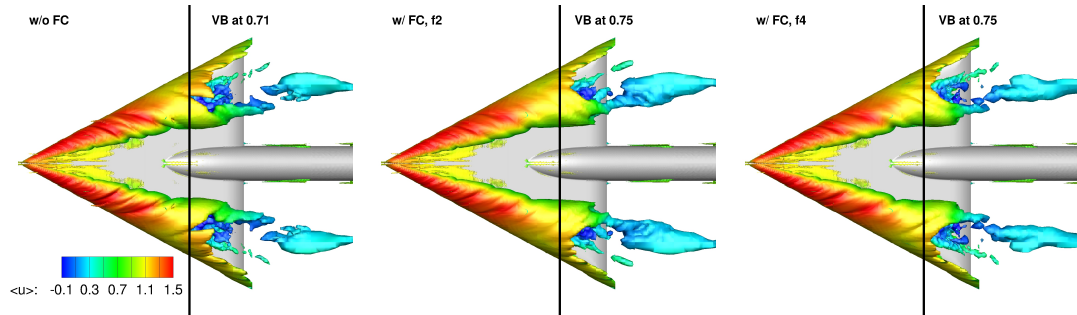
FIGURE 6.9: SLE, $\alpha = 28°$: Figures show isosurface of streamwise vorticity ($\omega_x = \pm 15$) colored by streamwise velocity. Vortex breakdown (VB) position indicated by black line. Left figure shows result with no flow control, center figure shows result with oscillating flap and $f2 = 2$, and right figure shows result with oscillating flap and $f4 = 4$.

the approach presented hereafter relies on geometric modifications leading to an injection of fluid from the pressure side and can thus be considered as a passive mechanism. Two geometric modifications are investigated: (1) Slots in the front part of the wing below the axes of the primary vortices, and (2), slots near the trailing edge, again located approximately below the primary vortices. A sketch of the geometries is shown in Fig. 6.10.

6.2.2 Main flow characteristics

The main flow characteristics are significantly altered in the case with slots in the front part, and slightly altered in the case with slots near the trailing edge, see Fig. 6.10. For the former configuration, one observes that the primary vortex is developed - almost - along the entire leading edge due to the significantly delayed vortex breakdown position, see below. Furthermore, the primary vortex structure near the slot position is affected for the considered slot geometry. This effect is probably less pronounced for an optimized slot shape, however. For the latter configuration, one observes minor changes regarding the flow characteristics, notably downstream of the trailing edge, where the injected fluid seems to stabilize the vortex core.

6.2.3 Vortex breakdown position

The numerical results show that the geometric modifications can significantly affect the vortex breakdown location, see Fig. 6.10. Slots in the front part of the wing, allowing for an injection of fluid from the pressure side into the vortex core, delay vortex breakdown,
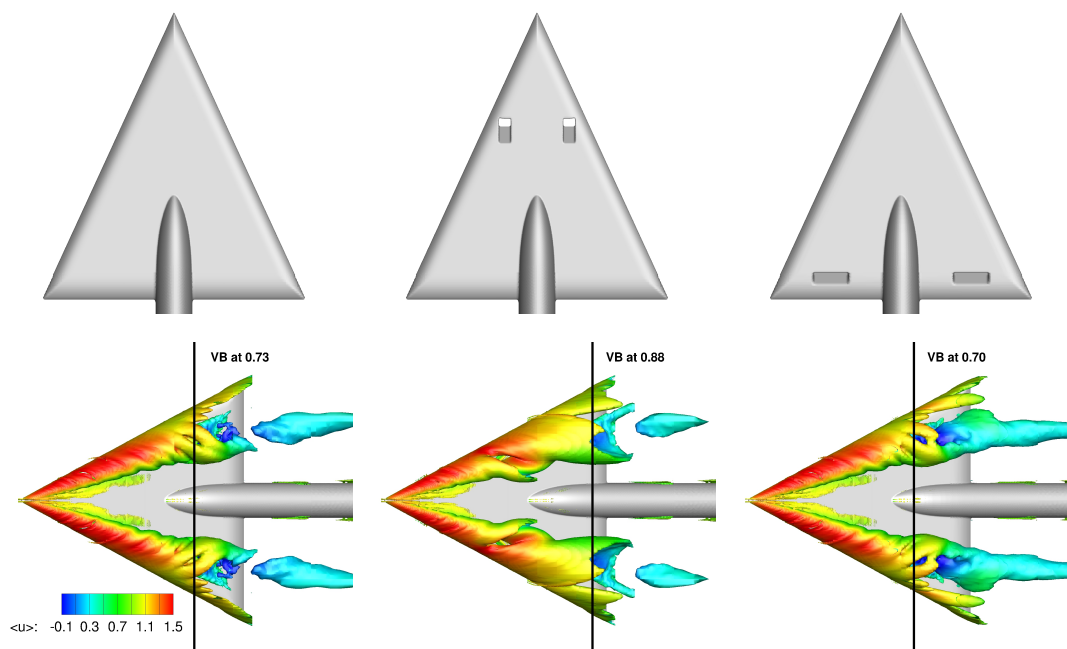
FIGURE 6.10: SLE, $\alpha = 28°$: Top row figures show wing geometries - no geometric modification (left), slots in the front part of the wing (center), and slots near the trailing edge (right). Bottom row figures show isosurface of streamwise vorticity ($\omega_x = \pm 15$) colored by streamwise velocity. Vortex breakdown (VB) position indicated by black line. Left figure shows result with no flow control, center figure shows result with slots in the front part of the wing, and right figure shows result with slots near the trailing edge.

similar to the concept of along-the-core blowing. Slots near the trailing edge, allowing for an injection of fluid from the pressure side in an upward direction with regard to the wing surface, move the vortex breakdown position upstream, similar to the concept of an upward deflected trailing edge jet. In the former case, vortex breakdown is delayed by 15 percentage points, in the latter, vortex breakdown is moved slightly upstream by 3 percentage points. Note that the two suggested geometric modifications have not been optimized regarding positioning, size, shape, or any other aspect. One can thus expect that a thorough investigation of the concept, including an optimization regarding the aforementioned aspects, will yield even better results.

Chapter 7

Conclusion

This final chapter consists of three parts. First, the main results and conclusions of the investigations without flow control are presented. Second, the main results and conclusions of the investigations regarding flow control mechanisms are summarized. Third, a short outlook on possible further investigations is given.

7.1 Conclusions regarding investigations without flow control

Regarding the investigations without flow control, the four main conclusions are:

(1) *Qualitatively, wall modeled LES correctly predicts main flow characteristics, apart from secondary vortex*: Using LES in conjunction with a TBLE based wall model, the main flow characteristics are predicted qualitatively correctly for both SLE and MRLE at all angles of attack considered, namely $\alpha = 13°, 18°$, and $23°$, with overall better results for the SLE. The only feature that is not predicted correctly is the secondary vortex, which is due to the insufficient grid resolution in the near wall region used in the present simulations. This observation confirms the findings of previous studies using similar wall models [110, 125], which also failed to predict such small scale secondary flow structures.

(2) *Quantitatively, results show overall good agreement with experiments*: Comparing the results of the simulations with experimental data, one observes, as expected,

overall better agreement for the SLE, given the geometrically fixed separation at the leading edge. For this case, the agreement can be considered as good. For the MRLE, which is computationally more challenging, the overall agreement with the experimental measurements is reasonable to good, showing discrepancies notably in the apex region, where the leading edge crossflow bluntness is highest and the primary vortex separation is predicted too far from the leading edge. Generally, the investigations show that a better resolved wall region leads to a significant improvement of the results, which indicates that the simplified TBLE based wall model used contains too many approximations - see below - for the complex flow considered. Moreover, the results confirm the conclusion of Cabot and Moin [73], who state that, regarding prediction accuracy and grid resolution, one gets what one pays for.

(3) *Simplified TBLE based wall model leads only to a minor improvement compared with a simple no-slip condition*: The simulations show that the simplified TBLE based wall model leads only to a minor improvement of the results compared with a simple no-slip condition, which may be explained by three aspects. First, for separating and reattaching flows, the boundary layer equations used to derive the TBLE based wall model are invalid. Second, in the wall model employed in this study, the pressure gradient and advective terms are neglected, and previous studies [73, 125, 129] have shown that both are important in TBLE based wall models for the aforementioned flows. Third, the wall model is not able to deal with transition, which can have a significant impact for the considered configuration [54, 64]. All three reasons may at least partly explain the wall model's rather poor performance.

(4) *Neural networks seem to be unsuitable to enhance wall modeling*: The use of neural networks to improve wall models is overall not promising due to the need of a priori data, see appendix A. Some specific applications may exist, though, e.g. using a neural network to speed up simulations.

In comparison to numerical investigations with RANS, see e.g. [69], the present wall modeled LESs predict vortex breakdown more accurately but fail to predict a secondary vortex. The latter is usually present in RANS investigations, oftentimes quantitatively incorrect, however [69]. In comparison to numerical investigations with DES, e.g. by

Jirasek [81] and by Tangermann et al.[80], the present wall modeled LESs achieve overall similar accuracy.

7.2   Conclusions regarding investigations with flow control

Regarding the investigations with flow control, the two main conclusions are:

(1) *Flow control via oscillating control surfaces seems to have an insignificant impact*: For the angle of attack considered, namely $\alpha = 28°$, flow control via oscillating control surfaces seems to have only a minor effect, which is in agreement with experimental observations, where perceptible improvements were only detected in the post-stall regime, i.e. angles of attack $\alpha > 35°$, notably for $\alpha = 45°$.

(2) *Injecting fluid from the pressure side can have a significant effect on vortex breakdown position*: Investigations with geometric modifications (slots) leading to an injection of fluid from the pressure side showed that, depending on the position of the slot, the vortex breakdown position can be moved either upstream or downstream quite effectively.

7.3   Outlook

Regarding future numerical investigations of the flow around delta wings - or other complex three-dimensional geometries - with the in-house flow solver INCA, the present results suggest three possible extensions:

(1) *Computational grids:* The adaptive mesh refinement techniques for the Cartesian grids used in the investigations do not allow for different refinement levels within a block. Refining the grid in the near wall region of complex geometries thus leads to either very many blocks, and consequently many buffer cells and lots of communication overhead, or prohibitively many grid cells. The investigations in this study showed that a better resolved wall region generally improves the results, and thus more elaborate grids allowing for refining the grid close to the wall in wall normal direction without generating prohibitively many blocks or cells will very likely yield more accurate predictions.

(2) *Immersed boundary method:* The immersed boundary method used in the present investigations does not accurately represent sharp edges on coarse grids. Therefore, an improved version, such as the one suggested by Örley et al. [130], will presumably yield better results on coarse grids.

(3) *Wall model:* The TBLE based wall model used in the investigations contains many approximations, e.g. the advective terms and the pressure gradient term are neglected, and it is not able to deal with transition. In addition, the boundary layer assumptions used to derive the TBLE are invalid in separation and reattachment regions, which the flow around delta wings exhibits. Therefore, a more sophisticated wall model based on the full three dimensional RANS equations and able to deal with transition, such as the one suggested by Park and Moin [131], is expected to yield better results. Moreover, improvements may be achieved by modifying the coupling position such that there are several LES cells below the coupling position, as suggested by Kawai and Larsson [132], who, for their particular numerical method, determined a minimum of four LES cells.

Regarding flow control, the suggested geometric modifications allowing for an injection of fluid from the pressure side provide many opportunities for further research, e.g. optimizing position, size, and shape of the slots, which has not been investigated yet. Both main parameters significantly influencing vortex breakdown - adverse pressure gradient and swirl level - can be targeted. For instance, by positioning the slots very close to the leading edge one might achieve an effect similar to active blowing through slots at the leading edges, which has been successfully employed in wind tunnel experiments at the Institute of Aerodynamics and Fluid Mechanics of Technische Universität München [126]. Therefore, geometric modifications allowing for an injection of fluid provide ample scope for further investigations.

Appendix A

Investigation of neural networks for wall modeling

The following appendix summarizes the investigation of neural networks (NN) for wall modeling, which has been part of the DFG project partly providing funding for this work. It contains five sections. Section one provides some examples of NN approaches used in computational fluid dynamics (CFD) and introduces the overall idea pursued in the following sections. Section two describes a general NN model, and section three details the specific implementation of the NN used in this investigation. Section four presents results of simulations of turbulent channel flow (TCF), and section five summarizes the findings of this investigation.

A.1   Introduction

In CFD, neural networks have been applied in several contexts, i.a. to describe eddy patterns in the near wall region [133], to represent chemistry data [134–136], to model the eddy viscosity [137], to model near wall turbulent flow [138], or to predict unsteady surface pressures [139]. In this work, a possible application of neural networks for wall modeling is investigated. In the following, it is described how such a model can be built, notably how to choose the architecture and how to train the network, and it is shown that the results obtained with the chosen model are comparable to the chosen

benchmark approach at significantly lower computational cost. However, the approach has several limitations.

As seen in section 3.4, wall models that estimate the wall shear stress and then impose it as a boundary condition on the exterior flow have proven to be effective and can be expressed as

$$\boldsymbol{\tau}_w = f(\mathbf{u}_0, p_0, \nu, \mathbf{x}_0) , \tag{A.1}$$

where f is an unknown function, mapping the velocity $\mathbf{u}_0$ and pressure p_0 of the exterior flow at the coupling position $\mathbf{x}_0 = (x_{1,0}, x_{2,0}, x_{3,0})$ to the wall shear stress $\boldsymbol{\tau}_w$. ν denotes the kinematic viscosity. It has been proven that NNs can approximate any continuous mapping on a compact interval [140], and thus a straightforward idea is to use a neural network (NN) to approximate the unknown mapping f, which is investigated hereafter.

A.2   Neural network model

Neural networks can be used in two ways: (1) classification, such as image recognition, and (2) regression [141]. Here, as in other cases in which NNs have been applied in simulations of turbulent flows, e.g. [133, 137, 139], the NN model is used in the latter way.

A NN consists of interconnected layers of neurons, see Fig. A.1. Each neuron consists of weighted inputs, an activation function, a bias term, and an output, see Fig. A.2. In a feedforward NN, there are only connections from the current layer to the following layer and no connections to the same or previous layers. Layers between the input and the output layer are called hidden layers. It has been shown that one hidden layer with bounded, increasing nonlinear activation functions suffices to approximate any continuous mapping [140], which is why a NN with only one hidden layer is considered in the following.

Having chosen the architecture of a NN, it must be trained using training samples. Assuming one wants to approximate the function
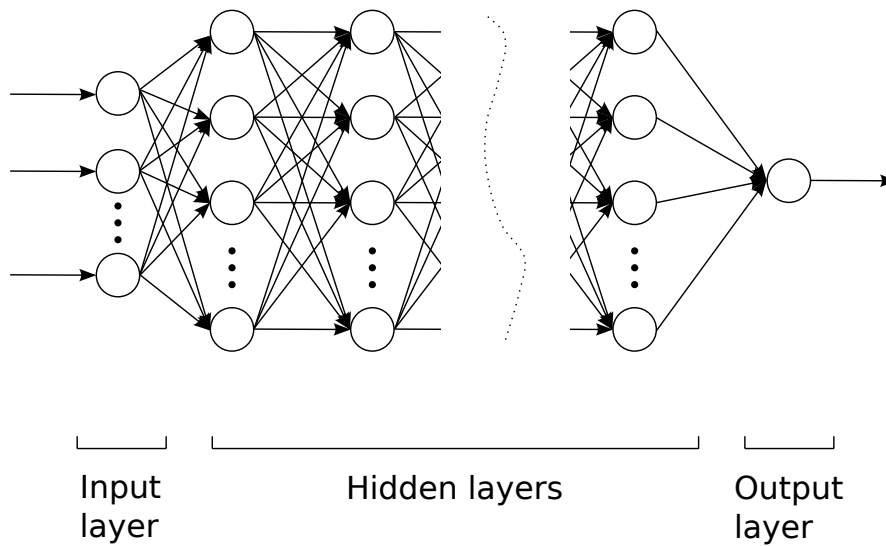
FIGURE A.1: General architecture of a feedforward neural network.
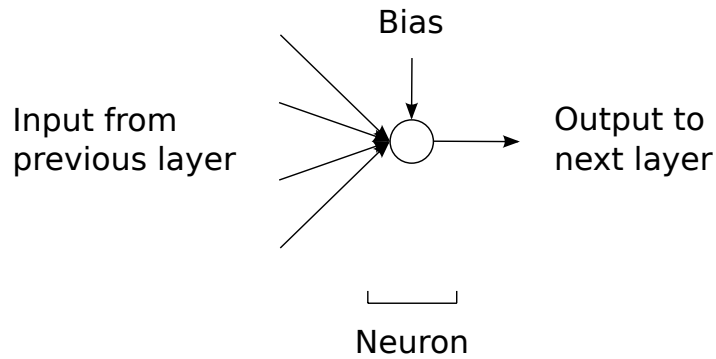
FIGURE A.2: Neuron in a neural network.

$$y = f(\mathbf{x}) \,, \tag{A.2}$$

one needs training sample pairs $(y^{(i)}, \mathbf{x}^{(i)})$, generated by equation A.2, and the training process consists in minimizing a suitable objective function, oftentimes the sum of squared errors between the desired outputs $y^{(i)} = f(\mathbf{x}^{(i)})$ and the outputs given by the NN, here denoted by $\tilde{y}^{(i)}(\mathbf{w}, \mathbf{x}^{(i)})$. The minimization is typically done using a back propagation algorithm. To avoid overfitting, a regularization term can be added. Without regularization term, the minimization problem becomes

$$\min_{\mathbf{w}} \ F(\mathbf{w}) = \frac{1}{2N} \sum_{i=1}^{N} (y^{(i)} - \tilde{y}^{(i)}(\mathbf{w}, \mathbf{x}^{(i)}))^2 \,, \tag{A.3}$$

where F is the sum of squared errors function, $\mathbf{w}$ is a vector containing all NN weights, N denotes the number of training samples, $y^{(i)}$ denotes the desired function value for the input $\mathbf{x}^{(i)}$, and $\tilde{y}^{(i)}$ denotes the NN prediction for $y^{(i)}$ given $\mathbf{x}$ and $\mathbf{w}$. Once the NN is trained, one has an analytical expression for the approximation, given by

$$\tilde{y}(\mathbf{x}) = \mathbf{w_1}\varphi(\mathbf{W_0}\mathbf{x} + \mathbf{b_0}) + \mathbf{b_1}\,, \tag{A.4}$$

where $\tilde{y}$ is the NN approximation of y, $\mathbf{w_1}$ is a row vector containing the NN weights between the hidden layer and the output layer, φ is a vector valued activation function, $\mathbf{W_0}$ is a matrix containing the NN weights between the input layer and the hidden layer, $\mathbf{b_0}$ is the bias of the hidden layer, $\mathbf{b_1}$ is the bias of the output layer, and $\mathbf{x}$ are the inputs. Note that equation A.4 assumes the previously mentioned NN with one hidden layer, nonlinear activation functions φ, and linear input and output layers, which can be viewed as a standard model for NN based function approximation [140].

A.3   Implementation

The presented concept is applied to approximate the generic model given in equation A.1 and tested on turbulent channel flow. Turbulent channel flow can be considered as a benchmark problem and thus has frequently been used to test novel wall modeling approaches, e.g. [110, 131, 142–146]. The simulations are conducted using the implicit LES approach ALDM for incompressible flows [101], which is briefly described in the following subsection.

A.3.1   Implicit LES framework

For incompressible flows with uniform density and $\nu = 1/Re$, the Navier-Stokes equations and the continuity equation can be written in non-dimensional form as

$$\frac{\partial \mathbf{u}}{\partial t} + \nabla \cdot \mathbf{F}(\mathbf{u}) + \nabla p - \nu\nabla^2\mathbf{u} = \mathbf{0}\,, \tag{A.5}$$

$$\nabla \cdot \mathbf{u} = 0\,, \tag{A.6}$$

with suitable boundary and initial conditions. Applying the filter $\mathbf{G}(\mathbf{x})$ to the previous two equations, one obtains the differential equations for the resolved scales.

$$\frac{\partial \overline{\mathbf{u}}}{\partial t} + \mathbf{G} * \nabla \cdot \mathbf{F}(\mathbf{u}) + \nabla \overline{p} - \nu \nabla^2 \overline{\mathbf{u}} = \mathbf{0} \,, \tag{A.7}$$

$$\nabla \cdot \overline{\mathbf{u}} = 0 \,. \tag{A.8}$$

Using ALDM, the aforementioned equations become

$$\frac{\partial \overline{\mathbf{u}}_{\mathbf{N}}}{\partial t} + \tilde{\mathbf{G}} * \tilde{\nabla} \cdot \tilde{\mathbf{F}}_{\mathbf{N}}(\tilde{\mathbf{u}}_{\mathbf{N}}) + \tilde{\nabla} \overline{p}_N - \nu \tilde{\nabla}^2 \overline{\mathbf{u}}_{\mathbf{N}} = \mathbf{0} \,, \tag{A.9}$$

$$\tilde{\nabla} \cdot \overline{\mathbf{u}}_{\mathbf{N}} = 0 \,, \tag{A.10}$$

in which the subscript $\mathbf{N}$ indicates the discrete approximation, $\tilde{\mathbf{u}}_{\mathbf{N}}$ denotes the approximate deconvolution of $\overline{\mathbf{u}}_{\mathbf{N}}$, $\tilde{\nabla}$ denotes the discrete approximation of the continuous operators, and $\tilde{\mathbf{F}}_{\mathbf{N}}$ is a consistent numerical flux function.

The equations are solved on a staggered Cartesian grid, and a pressure projection method is used. For time advancement, an explicit third-order Runge-Kutta scheme is used, in which the time step is dynamically adapted to satisfy the Courant-Friedrichs-Lewy (CFL) condition with $CFL = 1.0$. The pressure Poisson equation and diffusive terms are discretized by second-order central differences. The convective terms are discretized by the simplified version of ALDM (SALD) [102] for better computational efficiency.

A.3.2 NN wall model

A.3.2.1 Architecture

The neural network used to approximate the wall shear stress has 50 neurons in the hidden layer, 2 neurons in the input layer, and 1 neuron in the output layer. Its architecture is shown in Fig. A.3.
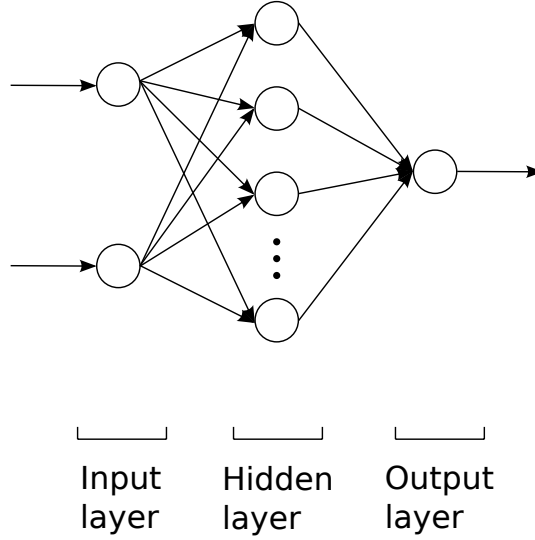
FIGURE A.3: Architecture of the feedforward NN with one hidden layer employed to predict the wall shear stress.

The number of neurons in the input layer is determined by the number of features selected (see following subsection), and the number of neurons in the output layer is one, since the neural network shall predict one component of the wall shear stress. In the code, a separate NN is used for each of the two components of the wall shear stress, $\tau_{w,x}$ and $\tau_{w,z}$. The two NNs have the same architecture and are built using the same methodology. Hereafter, the approach is described for $\tau_{w,x}$ only, given that the approach works analogously for $\tau_{w,z}$, and $\tau_{w,x}$ is abbreviated to τ_w. The number of neurons chosen for the hidden layer depends on the complexity of the function to be approximated and should ensure that the number of points to fit is at least four to five times larger than the number of degrees of freedom [138]. The latter is affected by the number of neurons in the hidden layer.

Analogous to equation A.4, the resulting approximation by the NN can be written as

$$\tilde{\tau}_w = \mathbf{w_1}\varphi(\mathbf{W_0}\mathbf{x} + \mathbf{b_0}) + \mathbf{b_1}\,, \tag{A.11}$$

where $\tilde{\tau}_w$ denotes the approximation for the wall shear stress, and $\mathbf{w_1}$, $\mathbf{W_0}$, $\mathbf{x}$, $\mathbf{b_0}$, and $\mathbf{b_1}$ are used in the same way as in equation A.4. For the activation function φ in the hidden layer, a hyperbolic tangent function

$$\varphi(x) = tanh(x) \tag{A.12}$$

is employed, since it fulfills the requirements (bounded, increasing, and nonlinear), and has been successfully employed in other studies, e.g. [133, 134, 138].

As argued by Nicoud et al. [144], reference data to derive new wall models should be obtained from wall-resolved LES or LES on coarse grids with an adequate model near the wall. Therefore, the data used to train the network in this work is taken from a turbulent channel flow LES with TBLE based wall model [110] at $Re_\tau = 2000$, which has proven successful in previous studies [107, 110]. The data is extracted from only one point of the channel's bottom wall and covers only a short span of time of the simulation. In total, 8000 training samples are used, which is a comparably low number. The aforementioned rule of thumb [138] holds, since there are $N_{dof} = 2 \cdot 50 + 50 + 2 + 50 + 1 = 203$ degrees of freedom, and $8000/203 \approx 40 > 5$.

A.3.2.2   Feature selection

An important aspect of every NN is the choice of inputs, also called feature selection. Ideally, as many inputs as possible are considered. However, given that there is often-times a small subset of possible inputs providing significantly more information about the desired output than the rest of the inputs, it is reasonable to take as few inputs as possible to reduce the overall complexity. Here, filter feature selection is used to accomplish this task, since it is computationally less expensive than other algorithms, such as forward or backward search [141].

In short, the idea of filter feature selection is to compute a score $S(i)$ for each possible input feature x_i that quantifies how much information about the desired output y is contained in feature x_i. Then, only features having scores above a certain threshold, or the ones with the largest scores, are selected. For the score $S(i)$, the absolute value of Pearson's correlation coefficient between the input feature and the desired output can be computed, yielding $S_{Pearson}(i)$ given by

$$S_{Pearson}(i) = \left| \frac{\sum_j (x_i^{(j)} - \bar{x}_i)(y^{(j)} - \bar{y})}{(\sum_j (x_i^{(j)} - \bar{x}_i)^2 (y^{(j)} - \bar{y})^2)^{1/2}} \right|. \tag{A.13}$$

Given that Pearson's correlation coefficient only provides a measure for the strength of the linear dependence between two variables, one can resort to a generalized correlation

TABLE A.1: Scores for feature selection for the approximation of the streamwise component of τ_w.

Feature	Description	$S_{Pearson}$	$S_{Spearman}$
$\tau_w^{(t-1)}$	wall shear stress from previous time step	0.994	0.993
$\partial p/\partial x\|_{1^{st}cell}$	pressure gradient in streamwise direction at first cell	0.382	0.355
$\partial p/\partial z\|_{1^{st}cell}$	pressure gradient in lateral direction at first cell	0.196	0.190
$u\|_{1^{st}cell}$	velocity in streamwise direction at first cell	0.150	0.135
$u\|_{2^{nd}cell}$	velocity in streamwise direction at second cell	0.084	0.069
$w\|_{1^{st}cell}$	velocity in lateral direction at first cell	0.050	0.034
$v\|_{1^{st}cell}$	velocity in vertical direction at first cell	0.038	0.043
$u\|_{3^{rd}cell}$	velocity in streamwise direction at third cell	0.033	0.035
$v\|_{3^{rd}cell}$	velocity in vertical direction at third cell	0.032	0.033
$v\|_{2^{nd}cell}$	velocity in vertical direction at second cell	0.023	0.025
$w\|_{2^{nd}cell}$	velocity in streamwise direction at second cell	0.023	0.022
$w\|_{3^{rd}cell}$	velocity in lateral direction at third cell	0.015	0.009

coefficient, such as Spearman's rank correlation coefficient, yielding $S_{Spearman}(i)$ given by equation A.14. Note that Spearman's correlation coefficient is simply Pearson's correlation between the ranked variables xr_i and yr:

$$S_{Spearman}(i) = \left| \frac{\sum_j (xr_i^{(j)} - \overline{xr_i})(yr^{(j)} - \overline{yr})}{(\sum_j (xr_i^{(j)} - \overline{xr_i})^2 (yr^{(j)} - \overline{yr})^2)^{1/2}} \right|. \tag{A.14}$$

The results for the possible set of inputs considered here is shown in table A.1.

Two aspects are apparent from table A.1. First, the scores computed using Pearson's coefficient do not differ considerably from the scores computed using Spearman's coefficient and, second, the ordering of the scores does not change, with one rather insignificant exception. Setting the threshold to 0.3, also used by Nicoud et al. [144] to signify high correlation, only the wall shear stress from the previous time step and the pressure gradient in streamwise direction are chosen as the two inputs for the NN. Note that numerically approximated derivatives have also been considered as possible inputs but did not yield scores higher than 0.3. Given that the coupling position $\mathbf{x_0}$ (see equation A.1) should be considered as well, the quantity $\partial p/\partial x\|_{1^{st}cell} \cdot \Delta y$ is chosen, where Δy denotes the distance of the first LES grid cell from the wall in wall normal direction. Note that this quantity has the same dimension as the desired output.
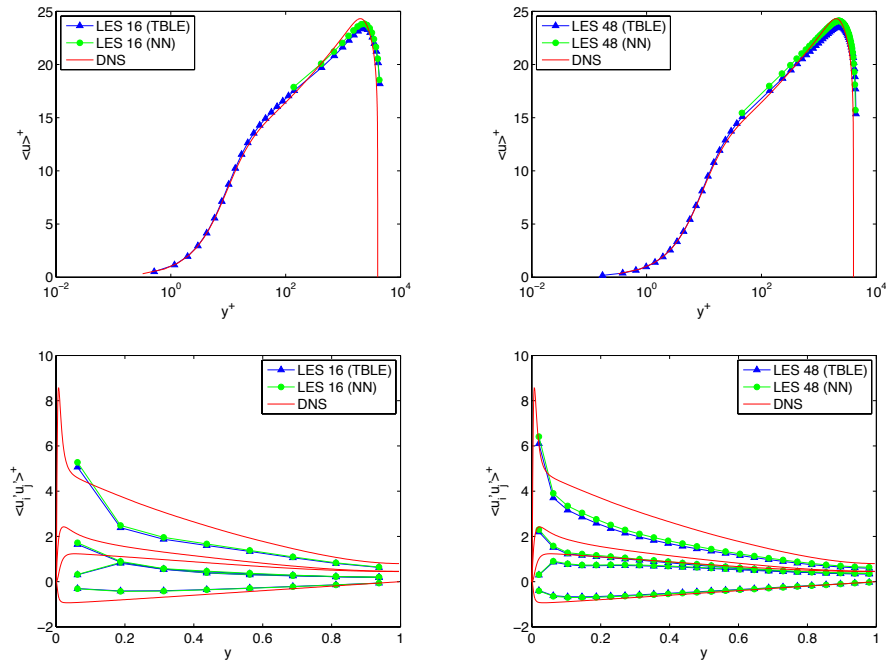
FIGURE A.4: Comparison of NN based wall model with TBLE based wall model for two different grid resolutions. DNS data from [147, 148].

A.3.2.3 Training

Having chosen an architecture and a set of features, the NN is trained using a Levenberg-Marquardt back propagation algorithm. The training of the network is stopped using a cross-validation criterion and is completed within several minutes on a standard desktop computer. Scaling of the inputs and different regularization approaches, e.g. Bayesian regularization, have been investigated but did not lead to significantly different results.

A.4 Results

The NN based wall function is tested in simulations of turbulent channel flow at $Re_\tau = 2000$ for different grid resolutions, namely 16, 32, and 48 cells in each of the three coordinate directions. The results are shown in Fig. A.4.

The results are compared with regard to two aspects: (1) accuracy and (2) computational efficiency.

Concerning aspect (1), accuracy, the results obtained using the NN based wall model are in good agreement with the results obtained with the TBLE model, which has to be

TABLE A.2: Comparison of computational efficiency of NN wall model and TBLE wall model. Time in seconds.

Setup	Wall model	Total time of simulation	Time spent in wall model routine
TCF_16	NN	$2.6 \cdot 10^3$	$4.7 \cdot 10^2$
TCF_16	TBLE	$5.4 \cdot 10^3$	$3.1 \cdot 10^3$
TCF_32	NN	$1.7 \cdot 10^4$	$1.5 \cdot 10^3$
TCF_32	TBLE	$2.8 \cdot 10^4$	$1.1 \cdot 10^4$
TCF_48	NN	$6.2 \cdot 10^4$	$2.7 \cdot 10^3$
TCF_48	TBLE	$8.6 \cdot 10^4$	$2.3 \cdot 10^4$

used as benchmark since the NN has been trained on data stemming from a simulation with the TBLE model. One observes that the wall shear stress predicted by the NN model is lower than the wall shear stress computed by the TBLE model. An a posteriori comparison of the wall shear stress values actually appearing in the LES simulation and the wall shear stress values of the training data, which were extracted from a simulation over a short period of time and at just one point of the domain, shows that the mean of the values in the training data is slightly lower than the mean of the wall shear stress values considering the entire simulation, which indicates that the approach is sensitive to the chosen training data. However, this problem could be remedied by using training data extracted from more locations and covering a longer span of time.

Regarding aspect (2), computational efficiency, in the simulations considered, the NN based wall model is approximately $6.6 - 8.4$ times faster than the TBLE based wall model. As a result, the total time for the simulation of turbulent channel flow at $Re_\tau = 2000$ is reduced by $28 - 52\%$, see table A.2 and Fig. A.5. Of course, the one-time overhead of training the NN has to be considered, too. However, as mentioned in section A.3.2.3, this overhead is insignificant, especially if the simulations run for a long time or if one conducts multiple simulations. Moreover, the NN could be trained online, and switched on once the training is completed.

A.5   Conclusion

It is shown that the NN based wall model described achieves results of roughly the same accuracy as a TBLE based wall model at significantly lower computational cost, which indicates that it may be suitable as an approach to speed up certain simulations.
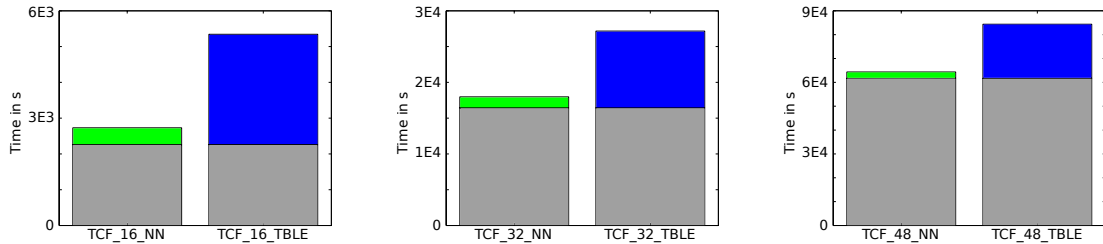
FIGURE A.5: Illustration of speed-up of NN based wall model in comparison with TBLE based wall model for turbulent channel flow. Total bar height represents total time of simulation. Colored part of bar represents time spent in wall model routine (green - NN, blue - TBLE).

The presented approach should not be considered as a new generally applicable wall model, however, but rather as a simple example demonstrating the general concept and procedure, and a possible use. Extensions to the model, e.g. modeling only the fluctuating part of the wall stresses and fixing the mean, as suggested by Nicoud et al. [144] for wall models based on linear stochastic estimation, or including more input variables, certainly provide scope for enlarging its range of applicability.

However, the suggested model has two main limitations: (1) The a priori needed training data, i.e. one needs samples to train the network and the samples have to cover the range on which the network will be applied later. (2) The wall shear stress is predicted relying only on data at the coupling position, i.e. partial information. Therefore, it will only work well if the information at the coupling position suffices to determine an approximate wall shear stress, which may not be the case in all types of flows.

In the context of wall modeling, neural networks could of course be applied differently. However, the former of the two limitations - the need of a priori training data - is a general and quite severe limitation of neural networks, which is why their overall suitability for wall modeling seems to be very limited. For instance, wall models based on optimal control theory [144, 149], which also necessitate a priori knowledge, have been investigated for more than a decade with rather moderate success, and, so far, their application did not go beyond the simulation of turbulent channel flow [145, 150]. Moreover, in comparison to other regression approaches, neural networks usually contain many free parameters and lack physical interpretability.

Bibliography

[1] R.M. Lang and G.L. Blaisdell. Passive snow removal with a vortex generator at the Pegasus runway, Antarctica. *Annals of Glaciology*, 26:231–236, 1998.

[2] B.N. Meroney and R.N. Meroney. Snow control with vortex and blower fences. In *A Multidisciplinary Approach to Snow Engineering*, Santa Barbara, 1988.

[3] C.E. Brown. Effect of Leading-Edge Separation on the Lift of a Delta Wing. *Journal of the Aeronautical Sciences (Institute of the Aeronautical Sciences)*, 21 (10):690–694, 1954.

[4] H. Werlé. Quelques résultats expérimentaux sur les ailes en flèche, aux faibles vitesses, obtenus en tunnel hydrodynamique. Technical report, La recherche aéronautique No. 41, 1954.

[5] E.C. Polhamus. A concept of the vortex lift of sharp-edge delta wings based on a leading-edge suction analogy. Technical report, TN D-3767, NASA Langley Research Center, 1966.

[6] M. Lee and C.M. Ho. Lift Force of Delta Wings. *Applied Mechanics Reviews*, 43 (9):209–221, 1990.

[7] J. Délery. Aspects of vortex breakdown. *Progress in Aerospace Sciences*, 30(1): 1–59, 1994.

[8] I. Gursul. Review of Unsteady Vortex Flows over Slender Delta Wings. *Journal of Aircraft*, 42(2):299–319, 2005.

[9] G. Drougge. The International Vortex Flow Experiment for Computer Code Validation. In *ICAS-Proceedings*, Jerusalem, Israel, 1988.

[10] A. Elsenaar, L. Hjelmberg, K.A. Bütefisch, and W.J. Bannink. The International Vortex Flow Experiment. In *AGARD-CP-437*. NATO STO, 1988.

[11] B. Wagner, S. Hitzel, M.A. Schmatz, W. Schwarz, A. Hilgenstock, and S. Scherr. Status of CFD Validation on the Vortex Flow Experiment. In *AGARD-CP-437*. NATO STO, 1988.

[12] H.W.M. Hoeijmakers. Modelling and Numerical Simulation of Vortex Flow in Aerodynamics. In *AGARD-CP-494*. NATO STO, 1991.

[13] D. Hummel. The international vortex flow experiment 2 (VFE-2): Objectives and overview. Technical report, Ch 17, RTO-TR-AVT-113, NATO STO, 2009.

[14] D. Hummel. Review of the Second International Vortex Flow Experiment (VFE-2). In *46th AIAA Aerospace Sciences Meeting and Exhibit*, Aerospace Sciences Meetings. American Institute of Aeronautics and Astronautics, 2008.

[15] D. Hummel. Final results of the international vortex flow experiment - resume and outlook. Technical report, Ch 35, RTO-TR-AVT-113, NATO STO, 2009.

[16] D. Hummel. The International Vortex Flow Experiment 2 (VFE-2): Background, objectives and organization. *Aerospace Science and Technology*, 24(1):1–9, 2013.

[17] C.R. Doering. The 3D Navier-Stokes Problem. *Annual Review of Fluid Mechanics*, 41:109–128, 2009.

[18] C. Fefferman. Existence and smoothness of the Navier-Stokes equation, 2014. URL `http://www.claymath.org/sites/default/files/navierstokes.pdf`.

[19] B. Desjardins and C.K. Lin. A survey of the compressible Navier-Stokes equations. *Taiwanese Journal of Mathematics*, 3(2):123–137, 1999.

[20] K.W. Mangler and J.H.B. Smith. A Theory of the Flow Past a Slender Delta Wing with Leading Edge Separation. *Proceedings of the Royal Society of London A: Mathematical, Physical and Engineering Sciences*, 251(1265):200–217, 1959.

[21] J.H.B. Smith. Improved calculations of leading-edge separation from slender, thin, delta wings. *Proceedings of the Royal Society of London. Series A, Mathematical and Physical Sciences*, 306(1484):67–90, 1968.

[22] R.T. Jones. Properties of low-aspect-ratio pointed wings at speeds below and above the speed of sound. Technical report, Technical Note No. 1032, National Advisory Committee for Aeronautics, 1946.

[23] K. Gersten. Nichtlineare Tragflächentheorie insbesondere für Tragflügel mit kleinem Seitenverhältnis. *Ingenieur-Archiv*, 30(6):431–452, 1961.

[24] R.K. Nangia and G.J. Hancock. A Theoretical Investigation for Delta Wings with Leading-Edge Separation at Low Speeds. Technical report, C.P. No. 1086, Queen Mary College, University of London, 1968.

[25] R.K. Nangia. Semi-Empirical Prediction of Vortex Onset and Progression on 65 deg. Delta Wings (RTO-AVT-113, VFE-2 Facet). In *46th AIAA Aerospace Sciences Meeting and Exhibit*, Aerospace Sciences Meetings. American Institute of Aeronautics and Astronautics, 2008.

[26] R.K. Nangia. Semi-empirical prediction of vortex onset on the VFE-2 configuration. Technical report, Ch 33, RTO-TR-AVT-113, NATO STO, 2009.

[27] M. Lessen, P.J. Singh, and F. Paillet. The stability of a trailing line vortex. Part 1. Inviscid theory. *Journal of Fluid Mechanics*, 63(04):753, 1974.

[28] F. Coton, S. Mat, R. Galbraith, and R. Gilmour. Low Speed Wind Tunnel Characterization of the VFE-2 Wing. In *46th AIAA Aerospace Sciences Meeting and Exhibit*, Aerospace Sciences Meetings. American Institute of Aeronautics and Astronautics, 2008.

[29] F. Coton, S. Mat, and R. Galbraith. Experimental investigations on the VFE-2 configuration at Glasgow University, United Kingdom. Technical report, Ch 22, RTO-TR-AVT-113, NATO STO, 2009.

[30] R. Konrath, C. Klein, and A. Schröder. PSP and PIV Investigations on the VFE-2 Configuration in Sub- and Transonic Flow. In *46th AIAA Aerospace Sciences Meeting and Exhibit*, Aerospace Sciences Meetings. American Institute of Aeronautics and Astronautics, 2008.

[31] R. Konrath, C. Klein, A. Schröder, and K. de Groot. Experimental investigations on the VFE-2 configuration at DLR, Germany. Technical report, Ch 19, RTO-TR-AVT-113, NATO STO, 2009.

[32] R. Konrath, C. Klein, and A. Schröder. PSP and PIV investigations on the VFE-2 configuration in sub- and transonic flow. *Aerospace Science and Technology*, 24 (1):22–31, 2013.

[33] S. Kurun. Experimental investigations on the VFE-2 configuration at TUBITAK-SAGE, Turkey. Technical report, Ch 23, RTO-TR-AVT-113, NATO STO, 2009.

[34] J.M. Luckring. Initial Experiments and Analysis of Vortex Flow on Blunt Edge Delta Wings. In *46th AIAA Aerospace Sciences Meeting and Exhibit*, Aerospace Sciences Meetings. American Institute of Aeronautics and Astronautics, 2008.

[35] J.M. Luckring. Initial Experiments and Analysis of Blunt-Edge Vortex Flows. Technical report, Ch 18, RTO-TR-AVT-113, NATO STO, 2009.

[36] J.M. Luckring. Initial experiments and analysis of blunt-edge vortex flows for VFE-2 configurations at NASA Langley, USA. *Aerospace Science and Technology*, 24(1):10–21, 2013.

[37] O. Rodriguez. Experimental investigations on the VFE-2 configuration at ONERA, France. Technical report, Ch 20, RTO-TR-AVT-113, NATO STO, 2009.

[38] A. Furman and C. Breitsamter. Investigation of Flow Phenomena on Generic Delta Wing. In *25th International Congress of the Aeronautical Sciences*, Hamburg, Germany, 2006.

[39] A. Furman and C. Breitsamter. Turbulent and Unsteady Flow Characteristics of Delta Wing Vortex Systems. In *46th AIAA Aerospace Sciences Meeting and Exhibit*, Aerospace Sciences Meetings. American Institute of Aeronautics and Astronautics, 2008.

[40] A. Furman and C. Breitsamter. Experimental investigations on the VFE-2 configuration at TU Munich, Germany. Technical report, Ch 21, RTO-TR-AVT-113, NATO STO, 2009.

[41] A. Furman and C. Breitsamter. Turbulent and unsteady flow characteristics of delta wing vortex systems. *Aerospace Science and Technology*, 24(1):32–44, 2013.

[42] S.B. Pope. *Turbulent flows*. Cambridge University Press, 2000.

[43] D. Chapman. Computational Aerodynamics Development and Outlook. *AIAA Journal*, 17(12):1293–1313, 1979.

[44] H. Choi and P. Moin. Grid-point requirements for large eddy simulation: Chapman's estimates revisited. *Physics of Fluids*, 24(1):011702, 2012.

[45] U. Piomelli and E. Balaras. Wall-layer models for large-eddy simulations. *Annual Review of Fluid Mechanics*, 34:349–374, 2002.

[46] J. Jiménez. Computing high-Reynolds-number turbulence: will simulations ever replace experiments? *Journal of Turbulence*, 4(022), 2003.

[47] J. Kim, P. Moin, and R.D. Moser. Turbulence statistics in fully developed channel flow at low Reynolds number. *Journal of Fluid Mechanics*, 177:133–166, 1987.

[48] H. Le, P. Moin, and J. Kim. Direct numerical simulation of turbulent flow over a backward-facing step. *Journal of Fluid Mechanics*, 330:349–374, 1997.

[49] P. Moin and K. Mahesh. DIRECT NUMERICAL SIMULATION: A Tool in Turbulence Research. *Annual Review of Fluid Mechanics*, 30:539–578, 1998.

[50] A.G. Hutton. The emerging role of large eddy simulation in industrial practice: challenges and opportunities. *Philosophical transactions. Series A, Mathematical, physical, and engineering sciences*, 367:2819–26, 2009.

[51] J. Ferziger and M. Peric. *Computational Methods for Fluid Dynamics*. Springer, 3rd edition, 2002.

[52] D.C. Wilcox. *Turbulence Modeling for CFD*. D C W Industries, 3rd edition, 2006.

[53] W. Fritz. Numerical Simualtion of the Peculiar Subsonic Flow-Field about the VFE-2 Delta-Wing with Rounded Leading-Edge. In *46th AIAA Aerospace Sciences Meeting and Exhibit*, Aerospace Sciences Meetings. American Institute of Aeronautics and Astronautics, 2008.

[54] W. Fritz. Numerical Solutions for the VFE-2 Configuration on Structured Grids at EADS-MAS, Germany. Technical report, Ch 25, RTO-TR-AVT-113, NATO STO, 2009.

[55] W. Fritz. Numerical simulation of the peculiar subsonic flow-field about the VFE-2 delta wing with rounded leading edge. *Aerospace Science and Technology*, 24(1): 45–55, 2013.

[56] J.F. Le Roy, O. Rodriguez, and S. Kurun. Experimental and CFD Contribution to Understanding Delta Wing Vortical Flow. In *46th AIAA Aerospace Sciences Meeting and Exhibit*, Aerospace Sciences Meetings. American Institute of Aeronautics and Astronautics, 2008.

[57] J.F. Le Roy and J. Riou. Numerical Solutions for the VFE-2 Configuration on Structured Grids at ONERA, France. Technical report, Ch 26, RTO-TR-AVT-113, NASA STO, 2009.

[58] O. Boelens. Numerical solutions for the VFE-2 configuration on structured grids at NLR, the Netherlands. Technical report, Ch 27, RTO-TR-AVT-113, NATO STO, 2009.

[59] E. Gurdamar, Y. Ortakaya, B. Korkem, and S. Kaya. Some Factors Influencing the Vortical Flow Structures on Delta Wings. In *46th AIAA Aerospace Sciences Meeting and Exhibit*, Aerospace Sciences Meetings. American Institute of Aeronautics and Astronautics, 2008.

[60] E. Gurdamar, Y. Ortakaya, S. Kaya, and B. Korkem. Numerical solutions for the VFE-2 configuration on structured grids. Technical report, Ch 28, RTO-TR-AVT-113, NATO STO, 2009.

[61] S. Crippa. Numerical solutions for the VFE-2 configuration on unstructured grids at KTH, Sweden. Technical report, Ch 30, RTO-TR-AVT-113, NATO STO, 2009.

[62] S. Crippa and A. Rizzi. Initial Steady/Unsteady CFD Analysis of Vortex Flow over the VFE-2 Delta Wing. In *25th International Congress of the Aeronautical Sciences*, Hamburg, Germany, 2006.

[63] S. Crippa and A. Rizzi. Steady, Subsonic CFD Analysis of the VFE-2 Configuration and Comparison to Wind Tunnel Data. In *46th AIAA Aerospace Sciences Meeting and Exhibit*, Aerospace Sciences Meetings. American Institute of Aeronautics and Astronautics, 2008.

[64] A. Crivellini, V. D'Alessandro, and F. Bassi. High-order discontinuous Galerkin RANS solutions of the incompressible flow over a delta wing. *Computers & Fluids*, 88:663–677, 2013.

[65] M. Shur, P.R. Spalart, K.D. Squires, M. Strelets, and A. Travin. Three Dimensionality in Reynolds-Averaged Navier – Stokes Solutions Around Two-Dimensional Geometries. *AIAA Journal*, 43(6):1230–1242, 2005.

[66] T. Nishino, G.T. Roberts, and X. Zhang. Unsteady RANS and detached-eddy simulations of flow around a circular cylinder in ground effect. *Journal of Fluids and Structures*, 24:18–33, 2008.

[67] W. Fritz and R.M. Cummings. What was Learned from the Numerical Simulations for the VFE-2. In *46th AIAA Aerospace Sciences Meeting and Exhibit*, Aerospace Sciences Meetings. American Institute of Aeronautics and Astronautics, 2008.

[68] P.R. Spalart. Detached-Eddy Simulation. *Annual Review of Fluid Mechanics*, 41: 181–202, 2009.

[69] W. Fritz and R.M. Cummings. Lessons learned from the numerical investigations on the VFE-2 configuration. Technical report, Ch 34, RTO-TR-AVT-113, NATO STO, 2009.

[70] P. Sagaut. *Large Eddy Simulation for Incompressible Flows*. Springer, 3rd edition, 2006.

[71] E. Garnier, N.A. Adams, and P. Sagaut. *Large Eddy Simulation for Compressible Flows*. Springer, 2009.

[72] J.S. Baggett, J. Jiménez, and A.G. Kravchenko. Resolution requirements in large-eddy simulations of shear flows. Technical report, Center for Turbulence Research, Annual Research Briefs, 1997.

[73] W. Cabot and P. Moin. Approximate Wall Boundary Conditions in the Large-Eddy Simulation of High Reynolds Number Flow. *Flow, Turbulence and Combustion*, 63:269–291, 1999.

[74] I. Mary. Large eddy simulation of vortex breakdown behind a delta wing. *International Journal of Heat and Fluid Flow*, 24(4):596–605, 2003.

[75] P.R. Spalart, W.H. Jou, M. Strelets, and S.R. Allmaras. Comments on the feasibility of LES for wings, and on a hybrid RANS/LES approach. In *Advances in DNS/LES, 1st AFOSR International Conference On DNS/LES*, Columbus, OH, 1997.

[76] J. Fröhlich and D. von Terzi. Hybrid LES/RANS methods for the simulation of turbulent flows. *Progress in Aerospace Sciences*, 44(5):349–377, 2008.

[77] R.M. Cummings and A. Schütte. Detached-Eddy Simulation of the Vortical Flowfield about the VFE-2 Delta Wing. In *46th AIAA Aerospace Sciences Meeting and Exhibit*, Aerospace Sciences Meetings. American Institute of Aeronautics and Astronautics, 2008.

[78] R.M. Cummings and A. Schütte. Numerical solutions for the VFE-2 configuration on unstructured grids at USAFA, United States. Technical report, Ch 32, RTO-TR-AVT-113, NATO STO, 2009.

[79] R.M. Cummings and A. Schütte. Detached-Eddy Simulation of the vortical flow field about the VFE-2 delta wing. *Aerospace Science and Technology*, 24(1):66–76, 2013.

[80] E. Tangermann, A. Furman, and C. Breitsamter. Detached Eddy Simulation compared with Wind Tunnel Results of a Delta Wing with Sharp Leading Edge and Vortex Breakdown. In *AIAA paper 2012-3329*, 2012.

[81] S. Peng, S. Deck, H. van der Ven, T. Knopp, P. Catalano, C. Lozano, C. Zwerger, J. Kok, A. Jirasek, and C. Breitsamter. Scrutinizing Hybrid RANS-LES Methods for Aerodynamic Applications. Technical report, FOI, Swedish Defence Research Agency, Stockholm, 2014.

[82] U. Piomelli. Wall-layer models for large-eddy simulations. *Progress in Aerospace Sciences*, 44(6):437–446, 2008.

[83] A.M. Mitchell and J. Délery. Research into vortex breakdown control. *Progress in Aerospace Sciences*, 37(4):385–418, 2001.

[84] A. Stanbrook and L.C. Squire. Possible Types of Flow at Swept Leading Edges. *Aeronautical Quarterly*, 15(2):72–82, 1964.

[85] C. Breitsamter. Unsteady flow phenomena associated with leading-edge vortices. *Progress in Aerospace Sciences*, 44(1):48–65, 2008.

[86] J.M. Luckring. Reynolds Number, Compressibility, and Leading-Edge Bluntness on Delta-Wing Aerodynamics. In *24th International Congress of the Aeronautical Sciences*, Yokohama, Japan, 2004.

[87] C. Breitsamter. *Turbulente Strömungsstrukturen an Flugzeugkonfigurationen*. PhD thesis, Technische Universität München, 1997.

[88] D. Hummel. Effects of Boundary Layer Formation on the Vortical Flow above Slender Delta Wings. Technical report, RTO-MP-AVT-111, NATO STO, 2004.

[89] D. Hummel and G. Redeker. Experimentelle Bestimmung der gebundenen Wirbellinien sowie des Strömungsverlaufs in der Umgebung der Hinterkante eines schlanken Deltaflügels. *Abhandlungen der Braunschweigischen Wissenschaftlichen Gesellschaft*, 22:273–290, 1970.

[90] S. Leibovich. The structure of vortex breakdown. *Annual Review of Fluid Mechanics*, 10:221–246, 1978.

[91] O. Lucca-Negro and T. O'Doherty. Vortex breakdown: a review. *Progress in Energy and Combustion Science*, 27(4):431–481, 2001.

[92] I. Gursul, Z. Wang, and E. Vardaki. Review of flow control mechanisms of leading-edge vortices. *Progress in Aerospace Sciences*, 43(7-8):246–270, 2007.

[93] H. Werlé. Sur l'éclatement des tourbillons d'apex d'une aile delta aux faibles vitesses. Technical report, La recherche aéronautique No. 74, 1960.

[94] Z. Wang, P. Jiang, and I. Gursul. Effect of Thrust-Vectoring Jets on Delta Wing Aerodynamics. *Journal of Aircraft*, 44(6):1877–1888, 2007.

[95] Q. Deng and I. Gursul. Effect of Leading-Edge Flaps on Vortices and Vortex Breakdown. *Journal of Aircraft*, 33(6):1079–1086, 1996.

[96] D. Greenblatt and I.J. Wygnanski. The control of flow separation by periodic excitation. *Progress in Aerospace Sciences*, 36(7):487–545, 2000.

[97] S. Ghosal. An Analysis of Numerical Errors in Large-Eddy Simulations of Turbulence. *Journal of Computational Physics*, 125(1):187–206, 1996.

[98] A.G. Kravchenko and P. Moin. On the Effect of Numerical Errors in Large Eddy Simulations of Turbulent Flows. *Journal of Computational Physics*, 131(2):310–322, 1997.

[99] S. Hickel, C.P. Egerer, and J. Larsson. Subgrid-scale modeling for implicit large eddy simulation of compressible flows and shock-turbulence interaction. *Physics of Fluids*, 26(10):106101, 2014.

[100] N.A. Adams, S. Hickel, and S. Franz. Implicit subgrid-scale modeling by adaptive deconvolution. *Journal of Computational Physics*, 200(2):412–431, 2004.

[101] S. Hickel, N.A. Adams, and J.A. Domaradzki. An adaptive local deconvolution method for implicit LES. *Journal of Computational Physics*, 213(1):413–436, 2006.

[102] S. Hickel and N.A. Adams. Efficient Implementation of Nonlinear Deconvolution Methods for Implicit Large-Eddy Simulation. In M. Nagel, W.E., Jäger, W., Resch, editor, *High Performance Computing in Science and Engineering*, pages 293–306. Springer Berlin Heidelberg, 2007.

[103] R. Mittal and G. Iaccarino. Immersed Boundary Methods. *Annual Review of Fluid Mechanics*, 37:239–261, 2005.

[104] G. Iaccarino and R. Verzicco. Immersed boundary technique for turbulent flow simulations. *Applied Mechanics Reviews*, 56(3):331, 2003.

[105] M. Grilli, S. Hickel, X.Y. Hu, and N.A. Adams. Conservative Immersed Interface Method for compressible viscous flows with heat transfer. Technical report, Technische Universität München, 2011.

[106] X.Y. Hu, B.C. Khoo, N.A. Adams, and F.L. Huang. A conservative interface method for compressible flows. *Journal of Computational Physics*, 219(2):553–578, 2006.

[107] Z.L. Chen. *Wall Modeling for Implicit Large-Eddy Simulation*. PhD thesis, Technische Universität München, 2011.

[108] S. Hickel, E. Touber, J. Bodart, and J. Larsson. A parametrized non-equilibrium wall-model for large-eddy simulations. Technical report, Center for Turbulence Research, Proceedings of the Summer Program 2012, 2012.

[109] S. Hickel. INCA Computational Fluid Dynamics, 2014. URL `https://inca-cfd.com/`.

[110] Z.L. Chen, S. Hickel, A. Devesa, J. Berland, and N.A. Adams. Wall modeling for implicit large-eddy simulation and immersed-interface methods. *Theoretical and Computational Fluid Dynamics*, 28(1):1–21, 2014.

[111] M. Meyer, S. Hickel, and N.A. Adams. Assessment of Implicit Large-Eddy Simulation with a Conservative Immersed Interface Method for turbulent cylinder flow. *International Journal of Heat and Fluid Flow*, 31(3):368–377, 2010.

[112] M. Grilli, P.J. Schmid, S. Hickel, and N.A. Adams. Analysis of unsteady behaviour in shockwave turbulent boundary layer interaction. *Journal of Fluid Mechanics*, 700:16–28, 2012.

[113] V. Pasquariello, M. Grilli, S. Hickel, and N.A. Adams. Large-eddy simulation of passive shock-wave/boundary-layer interaction control. *International Journal of Heat and Fluid Flow*, 49:116–127, 2014.

[114] J.F. Quaatz, M. Giglmaier, S. Hickel, and N.A. Adams. Large-eddy simulation of a pseudo-shock system in a Laval nozzle. *International Journal of Heat and Fluid Flow*, 49:108–115, 2014.

[115] C.P. Egerer, S. Hickel, S.J. Schmidt, and N.A. Adams. Large-eddy simulation of turbulent cavitating flow in a micro channel. *Physics of Fluids*, 26(8):085102, 2014.

[116] S. Remmler, M. D. Fruman, and S. Hickel. Direct numerical simulation of a breaking inertia–gravity wave. *Journal of Fluid Mechanics*, 722:424–436, 2013.

[117] J.U. Klar, C. Breitsamter, S. Hickel, and N.A. Adams. Integrated Experimental-Numerical Analysis of High-Agility Aircraft Wake Vortex Evolution. *Journal of Aircraft*, 48(6):2050–2058, 2011.

[118] M. Meyer. *Simulation of Complex Turbulent Flows on Cartesian Adaptive Grids*. PhD thesis, Technische Universität München, 2013.

[119] G. Castiglioni, J.A. Domaradzki, V. Pasquariello, S. Hickel, and M. Grilli. Numerical simulations of separated flows at moderate Reynolds numbers appropriate

for turbine blades and unmanned aero vehicles. *International Journal of Heat and Fluid Flow*, 49:91–99, 2014.

[120] J. Chu and J.M. Luckring. Experimental Surface Pressure Data Obtained on 65º Delta Wing Across Reynolds Number and Mach Number Ranges. Technical report, TM 4645, NASA Langley Research Center, 1996.

[121] LRZ. Leibniz Supercomputing Centre, 2014. URL `https://www.lrz.de/services/compute/supermuc/systemdescription/`.

[122] C. Zwerger, S. Hickel, C. Breitsamter, and N.A. Adams. Wall modeled large eddy simulation of a delta wing with round leading edge. In *New Results in Numerical and Experimental Fluid Mechanics X; Contribution to the 19th DGLR/STAB Symposium*, Munich, Germany, 2014.

[123] C. Zwerger, S. Hickel, C. Breitsamter, and N.A. Adams. Wall modeled large eddy simulation of the VFE-2 delta wing. In *Direct and Large-Eddy Simulation X; ERCOFTAC Workshop DLES10*, Limassol, Cyprus, 2015.

[124] C. Zwerger, S. Hickel, C. Breitsamter, and N.A. Adams. Wall-modeled large-eddy simulation of the VFE-2 delta wing. In *AIAA paper 2015-2572*, 2015.

[125] W. Cabot. Near-wall models in large eddy simulations of flow behind a backward-facing step. Technical report, Center for Turbulence Research, Annual Research Briefs, 1996.

[126] A. Kölzsch and C. Breitsamter. Vortex-Flow Manipulation on a Generic Delta-Wing Configuration. *Journal of Aircraft*, 51(5):1380–1390, 2014.

[127] C. Breitsamter. Personal communication, 2014.

[128] A. Kölzsch. Personal communication, 2014.

[129] W. Cabot. Wall models in large eddy simulation of separated flow. Technical report, Center for Turbulence Research, Annual Research Briefs, 1997.

[130] F. Örley, V. Pasquariello, S. Hickel, and N.A. Adams. Cut-element based immersed boundary method for moving geometries in compressible liquid flows with cavitation. *Journal of Computational Physics*, 283:1–22, 2015.

[131] G.I. Park and P. Moin. An improved dynamic non-equilibrium wall-model for large eddy simulation. *Physics of Fluids*, 26(1):015108, 2014.

[132] S. Kawai and J. Larsson. Wall-modeling in large eddy simulation: Length scales, grid resolution, and accuracy. *Physics of Fluids*, 24(1):015105, 2012.

[133] R.F. Blackwelder. A preliminary attempt to use neural networks for turbulent eddy classification. Technical report, Center for Turbulence Research, Annual Research Briefs, 1995.

[134] F.C. Christo, A.R. Masri, E.M. Nebot, and S.B. Pope. An integrated PDF/neural network approach for simulating turbulent reacting systems. *Symposium (International) on Combustion*, 26(1):43–48, 1996.

[135] M. Ihme, A.L. Marsden, and H. Pitsch. Generation of Optimal Artificial Neural Networks Using a Pattern Search Algorithm: Application to Approximation of Chemical Systems. *Neural computation*, 20(2):573–601, 2008.

[136] M. Ihme, C. Schmitt, and H. Pitsch. Optimal artificial neural networks and tabulation methods for chemistry representation in LES of a bluff-body swirl-stabilized flame. *Proceedings of the Combustion Institute*, 32(1):1527–1535, 2009.

[137] F. Sarghini, G. de Felice, and S. Santini. Neural networks based subgrid scale modeling in large eddy simulations. *Computers & Fluids*, 32(1):97–108, 2003.

[138] M. Milano and P. Koumoutsakos. Neural Network Modeling for Near Wall Turbulent Flow. *Journal of Computational Physics*, 182(1):1–26, 2002.

[139] S.J. Schreck, W.E. Faller, and M.W. Luttges. Neural Network Prediction of Three-Dimensional Unsteady Separated Flowfields. *Journal of Aircraft*, 32(1):178–185, 1995.

[140] S. Haykin. *Neural Networks and Learning Machines*. Pearson, 3rd edition, 2009.

[141] A. Ng. CS 229 - Machine Learning, Lecture Notes, Stanford University, 2011.

[142] W. Cabot. Large-eddy simulations with wall models. Technical report, Center for Turbulence Research, Annual Research Briefs, 1995.

[143] E. Balaras, C. Benocci, and U. Piomelli. Two-Layer Approximate Boundary Conditions for Large-Eddy Simulations. *AIAA Journal*, 34(6):1111–1119, 1996.

[144] F. Nicoud, J.S. Baggett, P. Moin, and W. Cabot. Large eddy simulation wall-modeling based on suboptimal control theory and linear stochastic estimation. *Physics of Fluids*, 13(10):2968, 2001.

[145] J.A. Templeton, M. Wang, and P. Moin. A predictive wall model for large-eddy simulation based on optimal control techniques. *Physics of Fluids*, 20(6):065104, 2008.

[146] S.T. Bose and P. Moin. A dynamic slip boundary condition for wall-modeled large-eddy simulation. *Physics of Fluids*, 26(1):015104, 2014.

[147] S. Hoyas and J. Jiménez. Scaling of the velocity fluctuations in turbulent channels up to Re[sub τ]=2003. *Physics of Fluids*, 18(1):011702, 2006.

[148] J. Jiménez and S. Hoyas. Turbulent fluctuations above the buffer layer of wall-bounded flows. *Journal of Fluid Mechanics*, 611:215–236, 2008.

[149] F. Nicoud and J.S. Baggett. On the use of the optimal control theory for deriving wall models for LES. Technical report, Center for Turbulence Research, Annual Research Briefs, 1999.

[150] J.A. Templeton, M. Wang, and P. Moin. An efficient wall model for large-eddy simulation based on optimal control theory. *Physics of Fluids*, 18(2):025101, 2006.